HHS Public Access

Author manuscript

Cell Rep. Author manuscript; available in PMC 2024 December 16.

Published in final edited form as:

Cell Rep. 2024 November 26; 43(11): 114911. doi:10.1016/j.celrep.2024.114911.

Nanoparticle-based itaconate treatment recapitulates low-cholesterol/low-fat diet-induced atherosclerotic plaque resolution

Natalie E. Hong[1,2], **Alice Chaplin**[1], **Lin Di**[1,2], **Anastasia Ravodina**[1], **Graham H. Bevan**[1], **Huiyun Gao**[1], **Courteney Asase**[1], **Roopesh Singh Gangwar**[1,3], **Mark J. Cameron**[4], **Matthew Mignery**[1], **Olga Cherepanova**[5], **Aloke V. Finn**[6,7], **Lalitha Nayak**[1,8], **Andrew A. Pieper**[9,10,11,12,13,14], **Andrei Maiseyeu**[1,15,*]

[1]Cardiovascular Research Institute, School of Medicine, Case Western Reserve University, Cleveland, OH, USA

[2]Department of Biomedical Engineering, School of Medicine, Case Western Reserve University, Cleveland, OH, USA

[3]Division of Allergy and Immunology, Department of Medicine, University of Virginia, Charlottesville, VA, USA

[4]Department of Population and Quantitative Health Sciences, Case Western Reserve University, Cleveland, OH, USA

[5]Department of Cardiovascular and Metabolic Sciences, Lerner Research Institute, Cleveland Clinic, Cleveland, OH, USA

[6]Department of Internal Medicine, Cardiovascular Division, University of Maryland School of Medicine, Baltimore, MD, USA

[7]CVPath Institute, Inc., Gaithersburg, MD, USA

[8]Department of Hematology & Oncology, University Hospitals Cleveland Medical Center, Cleveland, OH, USA

[*]Correspondence: axm1079@case.edu.

AUTHOR CONTRIBUTIONS

N.E.H. performed epigenetic and metabolic experiments, assisted with data interpretation, and wrote and edited the manuscript. A.C. performed animal studies in atherosclerosis and dietary cessation and prepared samples for NanoString, RNA-seq, and SIRM. L.D. performed ITA-LNP targeting experiments, biodistribution studies of ITA-LNP, flow-cytometric evaluation of cell-specific targeting, and aortic tissue isolation and testing. A.R. performed molecular biology experiments, *in vitro* testing of ITA-LNP, western blotting, RNA-seq analysis and metabolomics data, and assisted with writing the manuscript. G.H.B. performed TS surgeries and provided the vulnerable plaque mouse model. H.G. and C.A. contributed to live animal experiments, maintained animal colonies, and performed and analyzed immunohistochemistry. R.S.G. performed cell phenotyping by flow cytometry. M.J.C. analyzed scRNA-seq data. M.M. performed *in vitro* studies on various itaconate nanoparticle formulations and analyzed atherosclerosis in cessation experiments. O.G. analyzed scRNA-seq data and assisted with writing and editing of the manuscript. A.V.F. analyzed human atherosclerosis samples. L.N. performed experiments and edited the manuscript. A.M. conceptualized the research, planned all experiments, and wrote the manuscript. A.A.P. assisted with data interpretation and wrote the manuscript with A.M. and N.E.H. All authors reviewed, edited, and approved the final manuscript.

DECLARATION OF INTERESTS

The authors declare no competing interests.

SUPPLEMENTAL INFORMATION

Supplemental information can be found online at https://doi.org/10.1016/j.celrep.2024.114911.

[9]Department of Psychiatry, Case Western Reserve University, Cleveland, OH, USA

[10]Brain Health Medicines Center, Harrington Discovery Institute, University Hospitals Cleveland Medical Center, Cleveland, OH, USA

[11]Geriatric Psychiatry, GRECC, Louis Stokes VA Medical Center, Cleveland, OH, USA

[12]Institute for Transformative Molecular Medicine, School of Medicine, Case Western Reserve University, Cleveland, OH, USA

[13]Department of Pathology, Case Western Reserve University, Cleveland, OH, USA

[14]Department of Neurosciences, Case Western Reserve University, Cleveland, OH, USA

[15]Lead contact

SUMMARY

Current pharmacologic treatments for atherosclerosis do not completely protect patients; additional protection can be achieved by dietary modifications, such as a low-cholesterol/low-fat diet (LCLFD), that mediate plaque stabilization and inflammation reduction. However, this lifestyle modification can be challenging for patients. Unfortunately, incomplete understanding of the underlying mechanisms has thwarted efforts to mimic the protective effects of a LCLFD. Here, we report that the tricarboxylic acid cycle intermediate itaconate (ITA), produced by plaque macrophages, is key to diet-induced plaque resolution. ITA is produced by immunoresponsive gene 1 (IRG1), which we observe is highly elevated in myeloid cells of vulnerable plaques and absent from early or stable plaques in mice and humans. We additionally report development of an ITA-conjugated lipid nanoparticle that accumulates in plaque and bone marrow myeloid cells, epigenetically reduces inflammation via H3K27ac deacetylation, and reproduces the therapeutic effects of LCLFD-induced plaque resolution in multiple atherosclerosis models.

Graphical Abstract

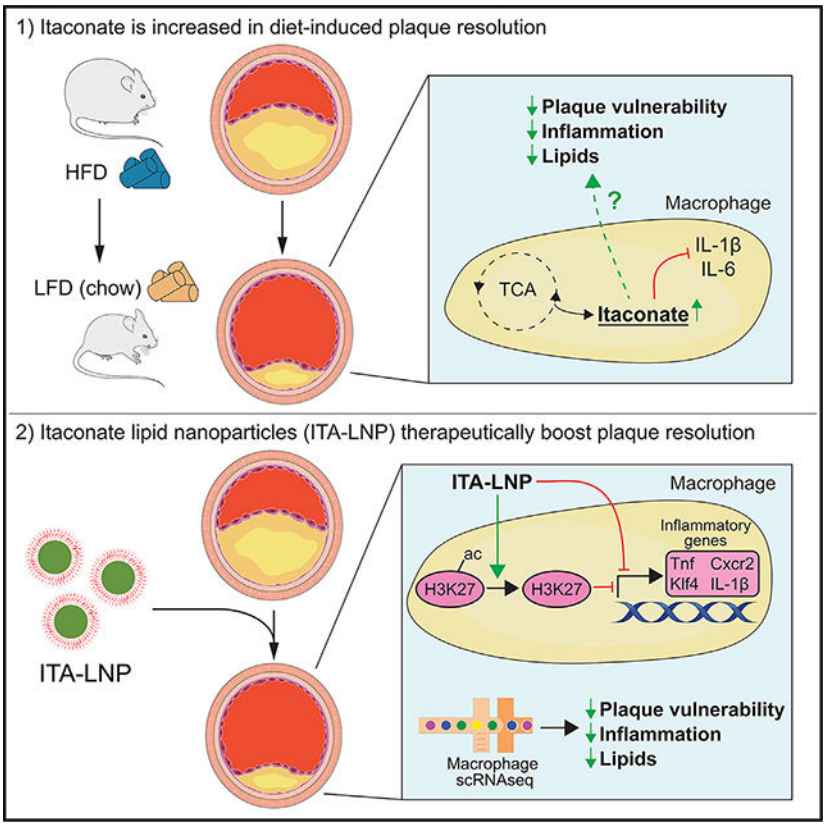

In brief

Hong et al. report that the tricarboxylic acid cycle metabolite itaconate (ITA) mediates low-cholesterol/low-fat-diet-induced atherosclerotic plaque resolution. Additionally, administration of nanoparticle-based ITA therapy induces plaque resolution in several models of atherosclerosis via multiple mechanisms, including epigenetic immunomodulation via H3K27ac deacetylation.

INTRODUCTION

Atherosclerotic cardiovascular disease (ASCVD) accounts for 16% of global mortality, and its prevalence is projected to increase further with the growing aging population.[1,2] In advanced states, ASCVD can progress to plaque rupture with subsequent myocardial infarction or cerebrovascular stroke.[2–4] Current therapies used to treat patients with ASCVD, such as cholesterol-lowering agents, are beneficial but do not achieve full protection, as patients still experience significant residual cardiovascular risk and mortality. Furthermore, advanced-stage treatments such as atherectomy are associated with risk of post-surgical complications.[5–12] While additional protection can be achieved by low-cholesterol, low-fat diet (LCLFD)-mediated plaque stabilization and inflammation reduction, a primary clinical strategy to combat ASCVD, patients often find it challenging to sustainably achieve this lifestyle modification.[13–25] Thus, there is a significant unmet need to develop therapeutics that recapitulate the protective efficacy of LCLFD. Unfortunately,

incomplete understanding of the underlying mechanisms of this phenomenon has thus far prevented attainment of this goal.

A major component of residual cardiovascular risk is inflammation, which is largely associated with macrophages.[5,7,12,26–28] While lipid lowering, whether by diet or by medicine, reduces inflammation, there is substantial clinical evidence demonstrating synergistic benefit in directly targeting inflammatory pathways in tandem with administration of lipid-lowering medications.[5,6,8,21,29–33] However, there still remains a significant risk of cardiovascular death and ASCVD complications in these patients.[6,8,29–32] Furthermore, chronically inhibiting general inflammation is not a viable treatment option because it increases susceptibility to infections and sepsis.[26–28] Epigenetic modification of inflammatory pathways has also been proposed as an alternative route to normalize physiologic inflammation. However, current therapeutics such as histone deacetylase (HDAC) inhibitors are plagued by lack of specificity, modest efficacy, and significant toxicity.[34–37]

To develop therapeutics to take on this residual risk, we investigated the inflammatory and metabolomic changes induced by lipid reduction via lifestyle modifications. Here, we report mechanistic insight into low-fat-diet-induced plaque resolution, which we translated into development of a therapeutic agent. By “plaque resolution” we refer to the phenomenon of increasing plaque stability, halting plaque growth, and directly resolving inflammation in plaque-related cells to prevent ASCVD complications. Laboratory animals that develop atherosclerotic plaque when fed a prolonged high-cholesterol, high-fat diet (HCHFD) demonstrate plaque resolution when they are subsequently switched to a normal low-fat diet (“dietary cessation”).[13–20] Here, we studied dietary cessation in two well-known atherogenic mouse models: *Apo*$E^{-/-}$ and *Ldlr*$^{-/-}$.[38–40] Using these models, we discovered that dietary cessation-driven plaque resolution is characterized by altered levels of the tricarboxylic acid (TCA) cycle metabolite itaconate (ITA), an immunomodulatory molecule, and of the ITA-synthesizing enzyme immunoresponsive gene 1 (IRG1, alternatively known as ACOD1; gene: *Irg1* or *Acod1*).[41,42] We also report elevated levels of IRG1 in vulnerable human carotid plaques and the absence of IRG1 in early or stable plaques.

We next tested whether exposing plaques to exogenously delivered ITA could directly achieve plaque resolution. While the ITA derivative 4-octyl itaconate (OI) has been previously shown to induce plaque resolution,[43,44] current ITA derivatives are not ideal for studying or replicating the biological effects of endogenous, unconjugated ITA, which differs from its derivatives.[42,45] Thus, to achieve targeted and efficient delivery of unconjugated ITA, we synthesized an ITA-based lipid nanoparticle, termed ITA-LNP. We demonstrate that ITA-LNPs deliver unconjugated ITA intracellularly, accumulate in myeloid cells in plaque and bone marrow, and recapitulate immunomodulatory effects that are unique to unmodified ITA.[42,46,47] We also show that ITA-LNPs are non-toxic and elicit epigenetic changes that lead to anti-inflammatory activity in plaques and myeloid progenitor cells in bone marrow. Additionally, we report that ITA-LNPs safely stimulate plaque resolution in several murine models with and without dietary cessation, including a model of unstable, vulnerable plaque that represents highly advanced ASCVD. Taken together, our results provide mechanistic understanding of the natural process of diet-driven plaque stabilization

and demonstrate selective delivery of a natural metabolite directly to myeloid cells to induce plaque resolution. This identifies a mode of treatment for ASCVD that targets inflammation with a two-pronged approach: site-specific plaque resolution and bone marrow progenitor priming.

RESULTS

Lowered cholesterol and lipoproteins via dietary cessation

We initiated our study of the physiologic, biochemical, and morphologic metrics of low-fat-diet-induced plaque resolution by assigning ApoE$^{-/-}$ mice to the following cohorts in a 25-week experimental paradigm: (1) “control” (Ctrl) mice fed a standard laboratory (chow) diet, (2) “progression” (Prog) mice fed an HCHFD, and (3) dietary “cessation” (Cess) mice fed HCHFD for 17 weeks and then subsequently switched to chow diet (Figure 1A). This experimental design is referred to as Ctrl-Prog-Cess (CPC). Metrics of plaque resolution (e.g., size, stability, and inflammation) were studied by comparing the groups at the end of this 25-week period.

As an atherogenic mouse model, ApoE$^{-/-}$ mice fed HCHFD have increased weight and lipid accumulation compared to mice fed a normal chow diet due to physiologic dysregulation of lipids.[39] Consequently, the progression group demonstrated significant body, white adipose tissue, and lymph node weight gain compared to the control group. The cessation group showed non-significant reductions in the aforementioned categories compared to the progression group. No differences were noted in brown adipose tissue content or organ weight between the cessation and progression groups (Figures S1A–S1E). Additionally, the progression group developed increased plasma cholesterol, liver cholesterol, plasma lipoproteins, and plasma phospholipids relative to the control group, and all four parameters were decreased in the cessation group back to control-group levels (Figures 1B–1D and S1F). Plasma triglycerides were also decreased in both the progression and cessation groups relative to the control group (Figure 1B), and liver triglycerides and non-esterified fatty acids were not altered across all groups (Figures 1C and S1G). Atherogenic very-low-density lipoprotein (vLDL) cholesterol was also increased in the progression group relative to the control group and decreased in the cessation group down to control-group levels (Figure 1D). There were no differences across all groups in intermediate-density lipoprotein (IDL), low-density lipoprotein (LDL), or high-density lipoprotein (HDL) (Figure 1D). NanoString analysis showed prominent regulation of major cholesterol- and lipid metabolism-relevant genes (e.g., *Cyp7A1* and *CD36*) in the liver in the cessation group relative to the progression group (Figure 1E).[48,49]

Reduced inflammation and induction of plaque resolution via dietary cessation

The progression group showed elevated inflammation in the form of increased gene expression in the liver for Toll-like receptor 4 (*Tlr4*) and tumor necrosis factor (*Tnf*), as well as increased plasma levels of interleukin-1β (IL-1β), IL-6, and macrophage inflammatory protein 1α (MIP1α). By contrast, the cessation group displayed lower inflammation, similar to the control group (Figures 1E, 1F, and S1H).

To further study inflammation in the CPC groups, we analyzed key immune cell populations that are key players in atherosclerotic development and inflammation. The markers of interest were immune activation marker Ly6C and migratory markers CCR2 and CX3CR1.[50–54] We examined these atherosclerosis-linked immune cell populations in blood, spleen, and bone marrow via flow cytometry (Figures 1G and S1I–S1K). In the cessation group relative to the progression group, blood $Ly6C^+$ (hi) monocytes were decreased and blood $Ly6C^-$ (lo) monocytes were increased (Figure 1G). There were no differences in either monocyte population across all groups in spleen and bone marrow (Figure 1G). These results indicate that dietary cessation reduces systemic inflammation.[50,51] Further phenotyping of monocytes in blood revealed additional substantial changes in the cessation group, especially for $CCR2^+$ cells (Figure 1H). Importantly, the number of $Ly6C^+CX3CR1^-$ monocytes, which directly traffic to atherosclerotic lesions and generate inflammatory macrophages,[52–54] was reduced in the cessation group (Figure 1H). Conversely, the number of $Ly6C^-CCR2^-CX3CR1^+$ monocytes, which are thought to differentiate into macrophages with attenuated inflammatory potential and possible inflammation-resolving properties,[52,54] was increased in the cessation group (Figure 1H).

Importantly, we observed significant resolution of atherosclerotic plaque in the cessation group, as seen by oil red O and hematoxylin-eosin (H&E, luminal occlusion) staining (Figure 2A). Key plaque stability metrics (i.e., predictive markers of plaque rupture and subsequent ASCVD events), including decreased necrotic core (Figure 2B) and increased smooth muscle actin (αSMA) to $Mac3^+$ macrophage ratio (Figure 2C), also indicated increased stability and lowered inflammation in the plaques of the cessation group.[55,56] Additional markers of plaque stability were also studied at the mRNA level using NanoString analysis. Immune cell markers (e.g., *Cd11b*) and vascular inflammation markers (e.g., *S100A9*, *Pon1*) were aberrantly dysregulated in the progression group and significantly returned toward normal in the cessation group (Figures 2D and S2A), confirming reduced inflammation in the cessation group.[57–60] Thus, our analysis indicated that inflammation associated with plaque progression is reduced in the cessation group and that dietary cessation leads to increased plaque stability.

NanoString counting of mRNA transcripts in single-cell leukocytes isolated from plaques showed a near complete reversal in expression of many inflammation-related genes in the cessation group, including interleukins, chemokines, chemokine receptors, complement activation, and oxidation stress-related markers (Figures 2E and S2A–S2C). Furthermore, transcriptomic analysis with bulk RNA sequencing (RNA-seq) in whole aortas from these groups demonstrated significant differences in levels of differentially expressed genes (DEGs) that indicated powerful epigenetic modulation of atherosclerosis by dietary cessation (Figures 2F and S2D–S2F; Sequence Read Archive accession SRA: PRJNA530042). Gene ontology (GO) analysis further showed that several interleukin and cytokine pathways were downregulated in the cessation group (Figures S2D–S2F). We also observed highly significant downregulation of many mitochondria-related genes in the cessation group (Figure 2G). Additionally, the cessation group showed statistically significant downregulation of both classic and alternative markers of macrophage activation (Figure 2H). Notably, typical pro-inflammatory genes, including targets in anti-atherosclerotic therapy such as *Il1b* and *Il6*,[61,62] were significantly downregulated in the

cessation group (Figure 2H). Intriguingly, transcription factor enrichment analysis of these RNA-seq datasets revealed 87 downregulated targets for peroxisome proliferator activated receptor α (PPARA), a regulator of lipid metabolism and inflammation, and 49 upregulated targets of nuclear factor erythroid 2-related factor 2 (NRF2; NFE2L2), a regulator of stress and inflammation, in the cessation group (Table S1).[63,64] Altogether, these findings suggest that transcriptional activation of antioxidant and anti-inflammatory programs is associated with plaque resolution.

Identification of macrophage-derived ITA as a key metabolite in dietary cessation-mediated plaque resolution

Metabolic studies have been conducted to seek out potential therapeutic targets to treat atherosclerosis, although they have largely been conducted in the setting of plaque progression.[65,66] To elucidate potential therapeutic strategies to induce plaque resolution, we examined how metabolism in aortic plaque responds to dietary cessation. Aortas, which are the site of major plaque formation in the ApoE$^{-/-}$ model, were isolated from a separate CPC experiment and incubated with uniformly labeled [^{13}C]glucose in an organoid culture according to established methods (Figure 2I).[67,68] The excised aortas were then subjected to stable isotope-resolved metabolomics (SIRM). Two modes of detection were employed: nuclear magnetic resonance (NMR) with heteronuclear single-quantum correlation analysis (HSQC), and ion chromatography-mass spectrometry (IC-MS, ProteomeXchange: PXD041137). More than 130 metabolites and their 1,300 isotopologs were identified to inform how ^{13}C was incorporated in metabolites of the TCA cycle, pentose phosphate pathway, and urea cycle, which are three fundamental and interconnected metabolic pathways. Selected metabolites are presented in Figures 2I and S2G. NMR-HSQC analysis of tissue-culture supernatants showed a trend of increased [^{13}C] lactate in the cessation group compared to the progression group, consistent with analysis of cell lysates showing higher production of intracellular [^{13}C]lactate (Figures 2I and S2G).[67–69] High glycolytic conversion of [^{13}C]glucose to pyruvate, followed by almost 90% fermentation into lactate, was indicative of high glycolytic rates in all CPC tissues (Figures 2I and S2G). This is expected, as even chow-diet-only ApoE$^{-/-}$ mice develop atherosclerosis and thus would likely have high glycolytic rates reflective of an atherosclerotic inflammatory state.[39] A notable difference between the cessation and progression groups was noted in ^{13}C enrichment of certain TCA metabolites at different stages of the cycle (Figure S2G). These differences indicate that the TCA cycle was largely utilizing a fuel source outside of glycolysis for earlier stages such as citrate (Figures 2J and S2G). Given this prominent difference, we further examined the TCA metabolites.

Intriguingly, analysis of total isotopologs of TCA cycle metabolites (^{12}C + ^{13}C) prominently revealed that ITA was particularly abundant in the progression group and sparse in the cessation group (Figure 3A). SIRM ^{13}C tracing studies subsequently confirmed that ITA synthesis from [^{13}C]glucose was highly upregulated in the progression group and reduced in the cessation group (Figure 3B). ITA is a metabolite produced from *cis*-aconitate by the IRG1 enzyme (gene: *Irg1* or *Acod1*) as an offshoot of the TCA cycle (Figure 3B).[41,70,71] Notably, ITA is produced by activated macrophages to reduce inflammation,[41,70,71] a strategy noted as a potential way to cause plaque resolution.[26,27] ITA inhibits succinate

dehydrogenase (SDH), leading to succinate accumulation as noted in the progression group (Figure S2G), and it additionally inhibits inflammation through other pathways, including NRF2 activation and suppression of mitochondrial oxidative phosphorylation (oxPhos).[42] These functions of ITA are consistent with the results of our transcriptome analysis. Thus, we focused on ITA as our primary molecule of interest in studying the mechanism of plaque resolution.

Enriched expression of IRG1 in cholesterol loading and in vulnerable plaque in mice and humans

We next investigated *Irg1*/IRG1 expression in mouse and human atherosclerotic lesions to further study the role of ITA in plaque resolution. In bulk plaque tissue, *Irg1* mRNA transcripts were highly expressed in the progression group compared to the cessation group and were undetected in the control group (Figure 3C). Furthermore, plaque myeloid cells co-expressed *Irg1* mRNA with $CD68^+$ and $Mac3^+$ in brachiocephalic artery (BCA) tissue sections, as shown by *in situ* hybridization with RNAscope (Figures S3A–S3E) and at the protein level via IRG1 immunofluorescence (Figure 3D). Notably, *Irg1* expression is limited to myeloid cell populations, as seen in the consortium ImmGen database[72] and in publicly available single-cell RNA-seq (scRNA-seq) datasets from human atherosclerosis specimens (Figure S3F, GEO: GSE131780).[73] In human plaque, immunofluorescence showed more prominent IRG1 co-staining with $CD68^+$ cells in stable plaque than in vulnerable plaque (Figures 3E, 3F, and S3K). This may be due to phenotypic changes seen in cells such as smooth muscle and macrophages in advanced human plaque,[74] as IRG1 was high and ubiquitous in vulnerable carotid plaques[75] (Figure 3E), whereas IRG1 was limited to a low number of $CD68^+$ cells in stable carotid plaques (Figure 3F). The anti-IRG1 antibodies that were used for these experiments were validated through *Irg1* overexpression, cell treatment, and human tissue staining (Figures S3I and S3J).

We hypothesized that the increase in *Irg1* expression in unstable plaque was an immunoprotective response to lipid accumulation. ITA is protective in an inflammatory milieu through multiple mechanisms and is released by macrophages in the context of bacterial or viral infection.[76] Stimulation of macrophages with inflammatory molecules, namely lipopolysaccharide (LPS), is a widely accepted model for studying *Irg1*/IRG1 expression and ITA release.[42,45] Surprisingly, however, when we tested some of the most common atherosclerosis-relevant *in vitro* models of cholesterol loading,[77–79] we noted that they failed to induce *Irg1* and *Il1b* expression in bone-marrow-derived macrophages (BMDMs) (Figure S3G). Notably, previous literature has reported similar findings with *Il1b*, and it has been previously shown that cells such as macrophages use acetyl-coenzyme A acetyltransferase (ACAT) to protectively process free cholesterol into esterified cholesterol, hence the observed lack of inflammatory response with these cholesterol-loading models.[80–82] Thus, we then turned to a different model for atherosclerotic-relevant cholesterol loading: incubation of BMDMs with cholesterol in the presence of an ACAT inhibitor (CP113818, ACAT-i).[83–86] This model yields increased intracellular free cholesterol levels, inducing the unfolded protein response and ultimately forming cholesterol crystals, a signature of advanced mouse and human atherosclerosis.[82,85–89] With this model, we observed that *Irg1* mRNA and IRG1 protein levels were significantly upregulated with free cholesterol loading

(Figures 3G and S3H). Concomitantly, the levels of pro-inflammatory genes, such as IL-6 (*Il6*), were also increased compared to PBS control (Figure 3G). IRG1 knockdown (IRG1 KD) in immortalized BMDMs (iBMDMs) using short hairpin RNA (shRNA) (Figure 3H) followed by cholesterol loading resulted in upregulation of inducible nitric oxide synthase (iNOS) and IkBα, which are, respectively, a major downstream mediator and upstream activator of NF-κB-p65 and inflammation (Figure 3I).

Altogether, these results demonstrate that expression of *Irg1*/IRG1, which produces ITA, is induced in late-stage unstable plaques and is driven by lipid accumulation. Given the immunomodulatory nature of ITA and the low production of IRG1 in early and stable plaques in mice and humans, we hypothesized that ITA is produced in unstable plaque to reduce inflammation and could thus act as a macrophage "switch" to allow for plaque resolution.[26,27] This inspired us to next test whether direct administration of ITA could achieve plaque resolution.

Formulation of ITA into a lipid nanoparticle pro-drug, ITA-LNP

To determine whether ITA could directly contribute to plaque resolution, we sought to test the effects of direct application of ITA to plaques. Although ITA is a hydrophilic dicarboxylic acid, previous studies have shown that ITA permeates cellular membranes through various active transport mechanisms.[42,45,90] However, unmodified ITA is likely to be a poor choice as a therapeutic because the micromolar levels that are required for efficacy would demand unreasonably high doses due to wide-spread systemic distribution and rapid systemic clearance.[42,91] ITA derivatives, such as dimethyl ITA (DMI) and OI, are widely used in place of ITA, as they are more cell permeable and more potent NRF2 activators.[42,45] In fact, it has been previously shown that direct administration of OI can achieve plaque resolution via NRF2.[43,44] However, ITA derivatives such as OI have effects somewhat divergent from those of unmodified ITA, notably in part due to their more potent electrophilicity, and thus are not ideal candidates to fully represent ITA's intracellular actions.[42,45,92] As our goal was to try to study the effects of unconjugated ITA on plaque resolution, we thus sought to design an ITA formulation that would achieve targeted delivery of unmodified ITA. To achieve this goal, we developed and tested ITA-based nanotherapeutic formulations. Here, we selected lipid-based nanoparticles as the delivery vehicle given their high biocompatibility, ease of drug loading, and natural affinity to target phagocytic cells such as macrophages.[93,94]

Our first formulation was itaconic acid salt loaded into the aqueous core of the lipid nanoparticle. Upon treating LPS-stimulated BMDMs with these ~100-nm-sized nanoparticles (Lip-ITA-Aq, Figures S4A and S4B), the BMDMs demonstrated no change in expression of inflammatory gene *Il1b*. This was in contrast to previous studies using free ITA and various carboxylic ester modifications of ITA, which exhibited robust downregulation of *Il1b* with treatment.[42,90] Our second formulation was several iterations of nanoparticles loaded with OI (OI-LNPs) in the lipid bilayer (Figure S4A and Table S2). BMDMs treated with this second formulation demonstrated downregulation of *Il1b* in a dose-dependent manner, while expression of NRF2 target gene heme oxygenase (*Hmox1*) was increased, consistent with an established mode of regulation of inflammation by ITA

(Figures S4C and S4D).[42,90] Again, however, while OI was shown to be effective in plaque resolution,[43] its divergent effects from unmodified ITA led us to develop a third and final formulation to achieve effective intracellular delivery of the original ITA molecule. Thus, to achieve delivery of the base ITA molecule, the final formulation was a lipid (1,2-dioleoyl-*sn*-glycero-3-phospho (ethylene glycol), Ptd-EG) conjugated to ITA (Figure 4A and Table S2; STAR Methods). Encouragingly, this lipid-ITA conjugate exhibited the following three key properties. First, it rapidly self-assembled into stable 66.5 ± 4.1-nm nanoparticles with a zeta potential of −30 ± 0.2 mV, referred to as ITA-LNP (Figures S4E and S4F; Table S2). Second, the design of ITA-LNP allows for rapid release of ITA through intracellular esterase activity (Figure 4A),[95,96] a significant improvement over previously described derivatives such as DMI.[42,46] Third, ITA-LNP, as a lipid nanoparticle, is amenable to surface modifications and/or incorporation of an imaging agent (e.g., fluorochrome) for biodistribution studies.[93] We also synthesized a control nanoparticle without ITA conjugation (Ctrl-LNP) of the same size for control-group treatments (Figure S4F and Table S2).

Intracellular release of ITA in myeloid cells by ITA-LNPs targets inflammation *in vitro* and *in vivo*

To evaluate the effects of ITA-LNPs in comparison to endogenous ITA and of ITA derivatives, we performed *in vitro* assays with several immune cell models. We first used two IL-1β assays (nigericin-activated BMDMs and monosodium urate [MSU]-activated THP-1s) to evaluate the effect of ITA-LNPs on IL-1β production and release. In LPS-primed, nigericin-activated inflammasomes in BMDMs, which models cholesterol crystal-triggered inflammation,[97,98] ITA-LNPs dose-dependently downregulated protein levels of the “mature” form of IL-1β and cleaved caspase-1 (p10) in cell-culture supernatants, a process that has been shown to be anti-inflammatory (Figure 4B).[99–101] ITA-LNPs also dose-dependently downregulated IL-1β in differentiated, MSU-activated THP-1 cells as seen in IL-1β cell reporter assays (Figure S4H and Table S3). Typically, endogenous ITA upregulates interferon-β (IFN-β), which differs from ITA derivatives (e.g., OI) that suppress IFN-β.[42] While ITA-LNPs did not exhibit IFN-β upregulation in LPS-stimulated BMDMs, ITA-LNPs’ effect on IFN-β was either non-suppressive or significantly less suppressive than OI in a dose-dependent manner (Figure S4I). In line with previous data on ITA ester derivatives,[90] ITA-LNPs decreased LPS-induced extracellular acidification rate (ECAR) in BMDMs (Figure 4C), demonstrating a robust anti-inflammatory effect against LPS stimulation. Furthermore, immunoblotting of unstimulated BMDMs treated with ITA-LNPs or Ctrl-LNPs confirmed that ITA-LNPs upregulate NRF2 and NRF2 targets HO-1 and p62 while somewhat lowering Keap1, although not statistically significantly (Figure 4D), similar to ITA derivatives.[45,90,102–104] Additional analysis revealed that ITA-LNPs significantly increased reduced glutathione to oxidized glutathione (GSH-to-GSSG) ratios and somewhat decreased NADPH-to-NADP ratios (Figure S4G), which are reflective of ITA’s ability to increase GSH production via NRF2 activation and induce NADPH oxidase activity.[105,106] Notably, intracellular succinate accumulated with ITA-LNP treatment (Figure 4E), which is seen in unmodified ITA but not with ITA derivatives.[42] While ITA has been shown to inhibit SDH and thus increase succinate accumulation, we also note that ITA-LNPs lowered expression of SDHA (Figure 4D). Glycolysis upregulation was confirmed by upregulation

of PKM2, PDH, and PKM1,[107,108] although the latter was statistically insignificant (Figure 4D), as well as intracellular accumulation of ^{13}C-labeled 1,3-bisphos-phoglycerate and extracellular [^{13}C]lactate release (Figure 4E). HIF-1α was lowered, albeit statistically insignificantly, similar to the effects of ITA derivatives (Figure 4D).[102] Ultimately, [U-^{13}C] glucose tracer SIRM experiments showed that intracellular levels of ITA were raised significantly upon ITA-LNP incubation with BMDMs (Figure 4E), which is not seen with several other modifications of ITA.[42,46] Notably, the intracellular [^{13}C]glucose conversion occurred without significant differences in glucose tracer uptake in Ctrl- vs. ITA-LNPs.

To study the biodistribution of ITA-LNPs in the setting of atherosclerosis, *Ldlr*$^{-/-}$ mice fed an HCHFD were bolus injected with Atto647-labeled ITA-LNPs. These experiments showed that ITA-LNPs robustly accumulated in atherosclerotic aortic plaque as well as in bone marrow after a single injection (Figures 4F–4H).

Furthermore, the amount of ITA-LNPs deposited in atherosclerotic plaque was increased with atherosclerosis severity and total plaque burden (Figure 4F). ITA-LNPs and Ctrl-LNPs accumulated in monocytes and neutrophils in plaque and blood, with a preference for Ly6C^{-} monocytes in the blood (Figures 4G and S4J). Importantly, we had shown that Ly6C^{-} monocytes were highly abundant in blood in response to cholesterol lowering in dietary cessation (Figures 1G), which suggests that these plaque-trafficking cells could be a carrier of ITA-LNPs under such conditions.[52–54] In conclusion, ITA-LNPs share mechanistic traits of ITA derivatives and traits unique to unmodified ITA, accumulate ITA intracellularly, and naturally target plaque and bone marrow, thus providing a superior means to study the therapeutic effect of ITA in atherosclerosis.

Effective plaque resolution with non-toxic ITA-LNP accumulation in plaque, blood, and bone marrow immune cells

Given ITA-LNPs' myeloid-targeting features, we tested the therapeutic efficacy of ITA-LNPs in both *Apo*$E^{-/-}$ and *Ldlr*$^{-/-}$ models. *Ldlr*$^{-/-}$ mice are another commonly used atherogenic knockout model, similar to *Apo*$E^{-/-}$ in outcome yet with different pathophysiologic mechanisms.[39] The use of both *Apo*$E^{-/-}$ and *Ldlr*$^{-/-}$ models allows for a multi-pronged study of atherosclerotic disease.[39] First, to mimic clinical treatments of lipid management (e.g., statins) with dietary modifications, we administered ITA-LNPs simultaneously with dietary restriction in *Ldlr*$^{-/-}$ mice (Figure 5A). Statin therapy, the most common clinical treatment for atherosclerosis, was not included as a control group because statins are known to have inconsistent effects in some atherogenic animal models.[109–111] Additionally, in contrast to *ApoE*$^{-/-}$ mice, *Ldlr*$^{-/-}$ mice develop only mild atherosclerosis when fed a chow diet, and thus chow diet cannot be used as a control group.[39,40,112] Therefore, our control "baseline" group for the *Ldlr*$^{-/-}$ studies was a subset of animals that were euthanized just before randomization to ITA-/Ctrl-LNP injections (Figure 5A).

To investigate whether plaque growth is alleviated by ITA-LNP therapy concomitant with dietary cessation, *Ldlr*$^{-/-}$ mice were fed HCHFD for 16 weeks and then switched to a chow diet and administered either ITA- or Ctrl-LNPs (50 mg/kg, two times per week, intravenously [i.v.]) for 8 weeks. At 24 weeks, we observed profound anti-atherosclerotic effects in the ITA-LNP group in comparison to the Ctrl-LNP group (Figures 5B–5E). The

size of the necrotic core in the plaques was reduced in the ITA-LNP group, as seen in aortic root tissue sections (Figures 5B and 5C). Oil red O staining and analysis of consecutive sections of aortic root and BCA showed significantly decreased lipid content with ITA-LNP treatment (Figures 5D and 5E). Plasma and liver cholesterol levels were also decreased significantly in Ctrl- and ITA-LNP groups in comparison to baseline, echoing what was observed in dietary cessation in *Apo*$E^{-/-}$ mice (Figures 1B, 1C, and 5F). However, there was no difference in plasma cholesterol levels between Ctrl- and ITA-LNPs, and there was a slight but significant increase in triglyceride levels in the ITA-LNP group compared to the Ctrl-LNP group but not the baseline group (Figure 5F), suggesting that the observed anti-atherosclerotic effects were due to the anti-inflammatory effects of ITA-LNPs as opposed to lipid-lowering actions. Importantly, plasma levels of IL-1β were downregulated with ITA-LNP treatment without impacting plaque stabilization (Figure 5F).[113] Indeed, the αSMA-to-Mac3^{+} ratio increased significantly in the ITA-LNP vs. Ctrl-LNP group BCA lesions (Figure 5G). This occurred concomitantly with reduced IL-1β signaling in plaque, evidenced by reduced IL-6 and phospho-IRAK in BCA sections (Figure 5H). Notably, this differs from previous literature showing that direct IL-1β targeting increases plaque vulnerability.[113]

Finally, to evaluate the safety of ITA-LNPs, we measured various parameters of tissue damage in the liver. The expression levels of common apoptosis, necrosis, and fibrosis markers in the liver and ALT/AST enzymes in serum were not statistically different between groups except for the downregulation of SDHA in response to ITA-LNP treatment (Figures S5A and S5B), which was previously observed (Figure 4D). There were also no differences in body or organ weights or liver histology between ITA-LNP and Ctrl-LNP groups (Figures S5C and S5D). In summary, this evidence shows that ITA-LNPs are non-toxic at this administered i.v. dose, which we predicted, since both ITA and Ptd-EG are typically well tolerated.[42,114,115]

Epigenetic-mediated plaque resolution by ITA-LNPs

Having confirmed that ITA-LNPs' anti-inflammatory effects lead to plaque resolution, we further probed the transcriptomes of ITA-LNP-targeted cells with deeper sequencing depths of bulk RNA-seq. In this assay, which we refer to as koded cells RNA-seq (kc-RNA-seq), kodecytes[116] are generated through targeting a living cell with a function-spacer-lipid construct (FSL) incorporated into ITA-LNPs or Ctrl-LNPs (Figure 6A). The biotin-conjugated FSL produces "koded" cells that exhibit a widely biotinylated cell surface (Figure 6B), allowing separation of nanoparticle-targeted cells via streptavidin-conjugated magnetic beads. Using *Ldlr*$^{-/-}$ mice and the previously described diet-switch design (Figure 5A), we injected unlabeled ITA- or Ctrl-LNPs for 6 weeks followed by switching to FSL-labeled ITA- and Ctrl-LNP injections for the last 2 weeks (Figure 6C). Single cells were separated from the whole aorta digest followed by pull-down of koded ITA- or Ctrl-LNP-targeted cells. Here, kcRNA-seq analysis identified 469 DEGs in the positive fraction and 456 DEGs in the negative fraction. Major DEG clusters from the positive fraction produced highly significant GO terms (Figures 6D and 6E) suggesting negative regulation (downregulated in ITA-LNPs) of epigenetic genes of leukocyte chemotaxis and positive regulation (upregulated in ITA-LNPs) of receptor-mediated endocytosis. Additionally, GO

terms of the whole positive fraction showed downregulation of leukocyte adhesion and tethering/rolling as well as reduction in inflammatory responses, while epigenetic-related terms such as chromatin remodeling and histone exchange were upregulated (Figure 6F).

In summary, these data reveal that ITA-LNPs epigenetically regulate inflammation on a single-cell level. Additionally, the enhancement of endocytosis-efferocytosis pathways, which are shown to promote plaque resolution, in ITA-LNP-targeted cells may also explain anti-atherosclerotic actions of ITA.[117–119]

Resolution of unstable atherosclerosis by ITA-LNPs in a model of tandem stenosis

To study ITA-LNPs' ability to treat unstable, vulnerable plaque, we turned to a surgically modified mouse model described by Chen et al., as typical atherosclerotic mouse models do not spontaneously generate vulnerable atherosclerotic plaque.[75,120–124] To simulate appropriate wall-stress dynamics, two non-occlusive sutures were applied to the right carotid artery (Figure 6G), which resulted in "tandem stenosis" (TS). TS-*ApoE*$^{-/-}$ mice fed HCHFD subsequently generated unstable plaque morphology proximal to the TS suture (Figure 6H). Gross pathology and Prussian blue staining prominently revealed intra-luminal thrombosis, intraplaque hemorrhage, and iron depositions (Figure 6H), which are characteristic features of unstable plaque in humans.[121,122]

The TS model allowed us to evaluate ITA-LNP efficacy under the extreme conditions of persistent hyperlipidemia and unstable, vulnerable plaque with the following timeline. First, *ApoE*$^{-/-}$ mice were fed HCHFD for 7 weeks, after which the TS surgery was performed. HCHFD feeding was then continued for an additional 7 weeks during which PBS placebo, ITA-LNPs, or Ctrl-LNPs were administered i.v. biweekly (Figure 6I). Single cells from the TS-affected right carotid artery (RCA) segment were subjected to flow-cytometric cell sorting to separate myeloid CD45^{+} cells, followed by 10× Genomics scRNA-seq pipeline (SRA: PRJNA729752). Unsupervised clustering analysis detected eight distinct leukocyte clusters in the combined datasets from the TS-RCA of ITA- and Ctrl-LNP-treated mice (Figure 6J). The following major cell types were identified according to published immune cell markers and cluster-specific marker genes: B cells (cluster 0), macrophages (cluster 1), natural killer cells (cluster 2), granulocytes (cluster 3), fibroblasts (cluster 4), monocytes (cluster 5) and T cells (cluster 6). Cluster 7 contained cells that expressed myeloid/dendritic cell markers (*Bst2*, *Ccr9*, *Trem2*, *Lyz2*) and also uniquely expressed *Siglec-h*, and thus was defined as interferon-producing cells (IPCs).[125,126] A number of gene set enrichment analyses of differential gene expression indicated reduction in apoptosis, adipogenesis, inflammatory response, and mitochondrial transport in ITA-LNPs vs. Ctrl-LNPs (Figure 6K). Strikingly, a GO term, "unstable atherosclerotic plaque UP,"[127] was significantly downregulated in cluster 2 in ITA- vs. Ctrl-LNPs. Notably, and in line with kcRNA-seq data from the *Ldlr*$^{-/-}$ model of atherosclerosis (Figure 6F), epigenetic-related terms including those related to leukocyte trafficking, inflammation, and chromatin remodeling changed significantly. With regard to ITA-treated macrophages (cluster 1), DEG analysis showed a reduction of classic inflammation-related genes, such as *Il1b*, *Cd14*, *Ccl3*, *Ccl4*, and *Clec4n* (also known as Dectin-2) (Figure 6L). Measurements of plaque vulnerability markers, such as an increase in *Wwp1* expression (and subsequent significantly reduced expression

of ubiquitin conjugates on a protein level), CD68, and CHI3L1, indicated decreased plaque vulnerability in ITA-LNP-treated groups (Figure S6A).[128–130] Gross pathology scoring confirmed significant reduction in the disease scores of ITA-LNP-treated animals (Figure S6B). Furthermore, serum analysis showed that major thrombosis-associated factors and inflammatory markers, including PAI-1, sP-selectin, and IL-6, were significantly downregulated in ITA- LNPs vs. Ctrl-LNPs, while anti-thrombotic thrombomodulin and anti-inflammatory T helper 2 cytokine IL-13 were upregulated (Figure S6C).[62,131–135] Notably, IL-13 has been previously shown to initiate inflammation resolution through macrophage efferocytosis and to suppress atherosclerosis.[134,135]

Collectively, these data show that even under severe conditions of hyperlipidemia and a shear-stress-induced inflammatory insult, ITA-LNPs significantly lower inflammation and stabilize vulnerable plaque. This likely occurs through multiple mechanisms, including epigenetic changes, attenuation of plaque inflammation, and systemic effects that reduce immune cell infiltration and secreted pro-thrombotic and pro-inflammatory factors.

Histone deacetylation and cellular priming by ITA-LNP-mediated epigenetic effects in myeloid cells

Based on the previous data showing the effects of ITA-LNP accumulation in plaque myeloid cells (Figure 6), we hypothesized that ITA-LNP accumulation in bone marrow (Figure 4H) could indicate that ITA-LNPs also affected bone marrow cells, particularly myeloid progenitor cells.[136] To test our hypothesis, we injected a single dose of ITA- or Ctrl-LNPs into wild-type C57BL/6 mice and collected and phenotyped the bone marrow 24 h later. We found prominent ITA-LNP accumulation in hematopoietic stem cells (HSCs) and multipotent progenitors (MPPs), both of which give rise to myeloid and lymphoid lineages (Figure S7A).[137,138] Subsequent RNA-seq GO term pathway analysis of these cells demonstrated that ITA-LNP injection induced changes in biological processes and molecular functions associated with chromatin remodeling and suppressed histone acetylation (Figure S7B). We also investigated the effects of ITA-LNPs in neutrophils, in which ITA-LNPs were shown to accumulate (Figure S4J), as they are considered the “first responders” to insults such as atherosclerotic plaque and play a key role in plaque biology.[139] Bone marrow neutrophils from ITA- or Ctrl-LNP bolus-injected mice were cultured with LPS or recombinant tumor necrosis factor α (TNF-α) (Figure 7A), and we observed that ITA-LNP-treated neutrophils secreted significantly lower levels of pro-inflammatory cytokines compared to those treated with Ctrl-LNPs (Figure 7B). Bulk RNA-seq followed by principal component analysis in these neutrophils demonstrated clear differences between the treatments (Figure 7C). Notably, the GO term analysis indicated that ITA-LNPs upregulated biological processes related to chromatin remodeling, nucleosome assembly, and downregulated interleukin production (Figure 7D). The effects of ITA-LNPs on transcriptional regulation of inflammation, using *Il1b* as a representative marker, were also confirmed by qPCR analysis (Figure S7C).

The above findings and scRNA-seq data (Figure 6) suggested that ITA-LNPs epigenetically regulate inflammation and cause chromatin remodeling. Additionally, ITA and its derivatives have been shown to activate the transcription factor NRF2, which has ties to histone

deacetylation.[90,140] Thus, we performed chromatin immunoprecipitation sequencing (ChIP-seq) and the assay for transposase-accessible chromatin (ATAC-seq) in flow-sorted NP^+ (Atto647-labeled ITA-LNPs or Ctrl-LNPs) cells of the bone marrow after a single injection (Figure 7A). For ChIP-seq, we used an antibody against acetylated histone H3 at lysine 27 (H3K27ac), a known epigenetic mark often associated with immune activation, active enhancers, chromatin opening, and transcription activation.[141,142] The ChIP-seq signal at 6,575 genes aligned by the transcription start site (Figure 7E) demonstrated a marked loss of acetylation at H3K27 in the ITA-LNP group. This was further confirmed by immunoblotting of ITA- or Ctrl-LNP-treated BMDM lysates (Figure 7F). Strikingly, this deacetylated state was associated with downregulation of inflammation and thrombosis-relevant *Il1b*, *Tnf*, and *F3*, as illustrated by the significant loss of H3K27ac and accessible chromatin at their promoters and regions of open chromatin (Figure 7G). Similarly, accessible chromatin at prototypical monocyte and neutrophil maturation genes (*Klf4*, *Cxcr2*, *PU.1*)[143–145] was greatly reduced in the cells of ITA-LNP-injected animals. GO analysis of ATAC-seq peaks demonstrated that lost peaks were associated with T cell receptor signaling and cytokine signaling pathways (Figure 7H). As H3K27 is acetylated by histone acetyltransferases (HATs), we analyzed the expression of a number of mRNAs that encoded histone-modifying enzymes, including HDACs and HATs. Notably, major HATs, including *Crebbp*, *Ep300*, *Kat2a*, and *Kat2b*, were significantly downregulated with ITA-LNP treatment (Figure 7I).

In summary, ITA-LNPs effectively target chronic and acute inflammation via epigenetic action on HATs in progenitor bone marrow cells. The reduction in HAT activity is associated with deacetylation and, consequently, closed chromatin at major histone mark H3K27ac, leading to suppressed transcription of major inflammatory and myeloid differentiation genes. Suppressed differentiation likely occurs through reduced accessibility of maturation genes and thus results in reduced neutrophil egress from the bone marrow. Consequently, neutrophils shift to less-inflammatory subtypes, manifesting protective actions against vascular inflammation including atherosclerosis and thrombosis.

DISCUSSION

In this study, we have elucidated the biological mechanisms underlying dietary cessation-driven plaque resolution in several atherosclerotic murine models. In doing so, we highlighted the role of ITA as an immunomodulatory and plaque-resolving agent that induces plaque stabilization, inhibits plaque growth, and is directly immunomodulatory in preventing ASCVD complications. Importantly, we also developed and tested an ITA-based drug candidate and demonstrated its plaque-resolving capabilities and myeloid cell targeting while also revealing previously unknown epigenetic modulatory properties of ITA.

The dietary cessation model was determined to be the optimal model for studying the mechanisms of plaque resolution, as it is more clinically relevant than other models such as sense-anti-sense or surgical transplantation methods.[146–151] Our dietary cessation model demonstrated significant plaque resolution and typical phenotypic changes associated with dietary modifications, such as reduction in cholesterol levels, plasma lipids, and systemic and local inflammation. Notably, dietary cessation is characterized by decreased mitochondrial metabolism and increased glycolysis. We identified that the levels of the

immunomodulatory metabolite ITA and the ITA-producing enzyme IRG1 (gene: *Irg1*) were a key difference between progression and cessation groups in mice as well as between unstable and stable plaques in human samples.[41,70,71] Between both groups, ITA and/or IRG1 were consistently more abundant in the more pathologic samples (e.g., progression and unstable human plaque).

The therapeutic efficacy of ITA-LNPs confirms that ITA is a response to atherosclerosis, rather than a driver or incidental biomarker of the disease. Because prior studies had shown that ITA and its derivatives inhibit IL-1β *in vitro* and *in vivo*, we tested ITA-LNP *in vitro* and in $Ldlr^{-/-}$ animals to confirm inhibition of IL-1β. While prior studies by Gomez et al. suggested that IL-1β inhibition causes plaque instability in animals with advanced atherosclerosis,[113] our $Ldlr^{-/-}$ model of advanced, unstable atherosclerosis showed that ITA-LNPs increased plaque stability as compared to baseline or Ctrl-LNPs. We thus hypothesize that ITA-LNPs' composite mechanism of action modulates IL-1β inhibition, thereby negating the detrimental impact on plaque stability. One of the future directions for our research will be to use genetic models to regulate *Irg1* gene expression to further explore the role of the IRG1 enzyme in IL-1β-dependent plaque resolution.[113]

Unlike certain ITA derivatives (e.g., DMI), our ITA-conjugated lipid nanoparticles (ITA-LNPs) led to intracellular accumulation of non-endogenous and unconjugated ITA, which was endorsed by ITA-LNPs' effects that were akin to both unconjugated ITA and of ITA derivatives.[42,46,47] We postulate that non-endogenous ITA forms because of principally different uptake mechanisms of ITA-LNPs and ITA derivatives. Engulfment of nanoparticles such as ITA-LNPs by macrophages is followed by endosome-lysosome fusion[152] and may allow for lysosomal de-esterification of ITA from the lipid carrier, resulting in intracellular release of unconjugated ITA. On the other hand, lipophilic derivatives such as DMI may bypass lysosomal processing because of their preferred entry into the cell via diffusion, leaving the molecule intact. Ultimately, this demonstrates that this ITA-nanoparticle treatment generates intracellular, unconjugated ITA and demonstrates effects (e.g., intracellular succinate accumulation) that are unique to unconjugated ITA.[42]

ITA-LNPs achieved direct, metabolite-based delivery and accumulation in myeloid cells in blood and plaque as well as in myeloid progenitor cells in the bone marrow. This myeloid- and bone-marrow-targeting trait is likely due to the negative surface charge of ITA-LNPs. We reported previously that negatively charged vesicles exhibit robust plaque- and macrophage-targeting characteristics, likely because such vesicles mimic apoptotic debris with negatively charged exteriorized oxidized lipids and phosphatidylserine serving as "eat me" signals for cellular uptake.[153–155] This phenomenon is also consistent with literature showing that certain negatively charged nanoparticles (e.g., aspartate-decorated particles) have high affinity to bone marrow.[156] Importantly, bone marrow is the source of myeloid progenitors such as HSCs and MPPs, which give rise to cell populations with high propensity to migrate to sites of inflammation (e.g., atherosclerotic plaque).[53,157] Targeting these cells with nanoparticles has been previously successfully demonstrated in models of transplant rejection, cancer, and atherosclerosis, delivering immunomodulatory agents able to "reprogram" the bone marrow compartment for therapeutic gain.[138,157,158] From this and

our observational data, it appears that ITA-LNPs may also “reprogram” bone marrow cells to aid in atherosclerotic resolution.

This targeting resulted in inflammation resolution and plaque stabilization and was corroborated in macrophages by scRNA-seq. We discovered that ITA may exhibit an epigenetic mode of action that could be a driving force of its broad anti-inflammatory effects. The analysis of datasets from bulk RNA-seq and scRNA-seq experiments suggested that ITA-LNPs affect epigenetic gene regulation, including actions on histone acetylation. This was further clarified through ChIP- and ATAC-seq and immunoblotting focusing on H3K27ac, a well-known inflammation enhancer mark. We determined that the loss of acetylation at H3K27ac, resulting in reduced transcription of inflammation- and thrombosis-relevant genes, is likely due to the reduction in HAT activity rather than through activation of HDACs. The exact mechanism by which ITA inhibits HATs and whether this inhibition is limited to a specific class of HATs remains to be determined in future studies. From a translational perspective, such mechanisms of action in conjunction with bone-marrow-selective delivery of ITA may provide long-lasting therapeutic efficacy and infrequent dosing.

In summary, we described the underlying mechanisms of the dietary cessation murine model of atherosclerotic plaque resolution and developed a treatment strategy in the form of a drug candidate based on our mechanistic insights. We tested this drug candidate, ITA-LNPs, in models of stable and vulnerable atherosclerotic plaques. ITA-LNPs were observed to be both effective and safe in these models and did not cause liver toxicity. Furthermore, we identified a mechanism of action of ITA, namely the epigenetic reprogramming of bone marrow cells via H3K27ac deacetylation, which likely contributes to plaque resolution and ITA’s overall immunomodulatory effects. We consider ITA-LNPs a safe and effective drug candidate for pursuit of future translation to clinical trials. Future studies will aim to develop ITA-LNPs as a therapeutic and determine the role of the IRG1 enzyme in atherosclerotic resolution.

Limitations of the study

Our model of dietary cessation was designed to demonstrate the differences in plaque burden and study its biology at 25 weeks after the start of HCHFD, so the results obtained may not fully correlate with other studies of different design. In addition, we did not investigate whether dietary cessation in the *Ldlr*$^{-/-}$ mouse model produces results comparable to those in *ApoE*$^{-/-}$ mice. We did, however, thoroughly investigate the effects of ITA-LNPs in both mouse models with consistent results, demonstrating that the effect of ITA-LNPs on atherosclerosis is not genotype dependent. We did not determine whether ITA-LNPs were liposomal or micellar in nature. However, we thoroughly characterized the ITA-LNP particle and its precursors and demonstrated the ability of ITA-LNPs to deliver ITA and induce ITA-related effects. Lastly, we were not able to definitively decipher the actions of ITA-LNPs on HATs that modulated the epigenetic effect and whether the direct or indirect inhibition of HATs by ITA-LNPs may occur. Effects on HATs as well as the specificity of ITA-LNPs warrant future investigation.

RESOURCE AVAILABILITY

Lead contact—Further information and requests for resources and reagents should be directed to and will be fulfilled by the lead contact, Andrei Maiseyeu (axm1079@case.edu).

Materials availability—All unique/stable reagents generated in this study are available from the lead contact with a completed materials transfer agreement.

Data and code availability

- scRNA-seq, CPC model, and IC-MS datasets have been deposited in the Sequence Read Archive and ProteomeXchange and are publicly available as of the date of publication. Accession numbers are listed in the key resources table. Microscopy data reported in this paper will be shared by the lead contact upon request.
- This paper does not report original code.
- Any additional information required to reanalyze the data reported in this paper is available from the lead contact upon request.

STAR★METHODS

Detailed methods are provided in the online version of this paper and include the following:

EXPERIMENTAL MODEL AND STUDY PARTICIPANT DETAILS

Cell culture—IL-1β Reporter HEK 293 cells, RAW 264.7, THP1, and iBMDMs were acquired from vendors as noted in the KRT. Primary BMDMs, smooth muscle cells, endothelial cells, and hepatocytes were acquired from mice as specified in this publication. Unless specified, the basal medium consisted of Dulbecco's modified Eagle's medium (DMEM) supplemented with 10% heat-inactivated fetal bovine serum and 1% streptomycin/penicillin. Cell culture flasks and cell culture dishes were used with tissue-culture-treated vessels for all cell types except primary BMDMs, which were cultured in non-tissue-culture-treated vessels. The cell culture incubator was maintained at 37°C at 5% CO2.

Animal studies—Male *ApoE*$^{-/-}$ and *LDLr*$^{-/-}$ mice (5 weeks of age) were purchased from The Jackson Laboratory (Bar Harbor, ME) and kept in AAALAC-accredited facilities at Case Western Reserve University. The experimental procedures here described were approved by The Institutional Animal Care and Use Committee (IACUC). Animals were housed five per cage and allowed to acclimate in the facility for one week. Throughout all experiments, animals were kept on a 12:12 h light-dark cycle at 22°C, and both diet and water were provided *ad libitum*.

METHOD DETAILS

Experimental design

CPC experiments: *ApoE*$^{-/-}$ mice were fed a high-cholesterol, high-fat diet (HCHFD), which provided 40% kcal from fat and 1.25% added cholesterol (Research Diets Inc., D12108C). After 17 weeks, half of the animals on HCHFD were switched to a standard

laboratory diet (chow diet) (Diet Switch (Cessation) group, $n = 8$) for another eight weeks. The other half remained on HCHFD diet for these 8 weeks (Progression group, $n = 6$). Control mice ($n = 5$) received a chow (standard laboratory diet) throughout the whole experiment. Animals were euthanized by isoflurane followed by cervical dislocation. Blood was taken by cardiac puncture and organs excised, weighed and snap-frozen in liquid nitrogen. Samples were stored at −80°C until further analysis.

***ITA-LNP testing in* LDLr$^{-/-}$ *mice*:** *LDLr*$^{-/-}$ mice (10–15 per group) were fed HCHFD starting 10 weeks of age for 16 weeks, followed by randomization to a baseline (6 animals euthanized at this point) and two treatment groups: ITA- and Ctrl-LNP. For treatment groups the mice were switched to standard laboratory diet and the treatments were administered ITA- or Ctrl-LNP at 50 mg/kg two times a week for an 8 week period.

***ITA-LNP testing in tandem stenosis* ApoE$^{-/-}$ *model*:** Tandem stenosis (TS) was induced as described below. *ApoE*$^{-/-}$ mice with TS were treated for 7 weeks with ITA- or Ctrl-LNP at 50 mg/kg three times a week intravenously or 0.1 mL PBS as a placebo control.

Plasma lipids determinations—Blood obtained from cardiac puncture after euthanasia was kept on ice and centrifuged at 2500 rpm for 25 min at 4°C in order to isolate plasma. Samples were stored at −80°C until further analysis. Blood glucose was obtained using a hand-held glucometer (Ascensia Diabetes Care, Parsippany, NJ) from tail-vein blood, and insulin, plasma fatty acids (cholesterol, TG, NEFA and phospholipids) were detected using commercial kits (key resources table).

Plasma lipoproteins: Plasma lipids were analyzed using fast protein liquid chromatography (FPLC) as previously described.[159] Briefly, the separation was performed on a Superose 6 Increase 3.2/300 column (Cytiva Bio-Sciences) using isocratic elution with a PBS buffer containing 10 mM phosphate and 154 mM NaCl at pH 7.4 and room temperature. The injection volume was set at 10 μL via injection loop and the samples were diluted ten times in PBS prior to the separation. The flow rate was set at 0.05 mL/min. The effluent from the column was delivered into a 25 μL binary mixing tee (ASI part number: 402–0025B), where it was mixed with either enzymatic cholesterol reagent (Infinity, Thermo Scientific TR13421) or enzymatic triglyceride reagent (Infinity, Thermo Scientific TR22421). The reagent was delivered at 0.25 mL/min via an auxiliary pump (Lab Alliance, Series 1), after which the mixture of the reagent and the mobile phase reacted in an ASI post column reactor (Model 310) equipped with a 1 mL cartridge and maintained at 45°C. The absorbance of the effluent was then recorded via Shimadzu SPD-20A UV/Vis detector at 590 nm. The quantification was performed using Shimadzu Lab Solutions version 5.3 by using the peak area of the lipoprotein interpolated with the area of the standard curve peak produced with known amounts of cholesterol or triglycerides using corresponding standards (Stanbio Laboratory).

Plasma cytokines—Serum levels of eotaxin, granulocyte-colony stimulating factor (G-CSF), IL-1α, IL-2, IL-5, IL-6, IL-10, IL-12 (p70), IL-13, IL-15, IL-17, interferon gamma-induced protein 10 (IP-10), chemokine (C-X-C motif) ligand 1 (KC), C-X-C motif chemokine 5 (LIX), monocyte chemoattractant protein 1 (MCP-1), MIP1α, MIP2,

monokine induced by gamma interferon (MIG) and vascular endothelial growth factor (VEGF) were determined using the Mouse High-Sensitivity Cytokine array (cat#: MD31, Eve Technologies, Calgary, Canada).

Liver lipid determinations—Whole livers were ground using the Geno/Grinder 2010 (SpexSamplePrep, Metuchen, New Jersey) for 90 s and 30 s rest at a rate of 1500 strokes/min. Liver powder was then lyophilized, and a solution of chloroform:methanol was added, followed by bath sonication. Samples were then centrifuged at 14000 × *g* for 5 min. The organic lipid extract was then removed and placed in a centrifugal evaporator. Following, the samples were resuspended in PBS containing 1% sodium taurocholate, and cholesterol and triglycerides were detected using commercial colorimetric kits (Stanbio Laboratory).

Liver gene expression—Whole livers were ground as described above. RNA was isolated from liver powder using the RNeasy Mini Kit (Qiagen, 74004), quantified using the NanoDrop ND-1000 spectrophotometer (NanoDrop Technologies Inc., Wilmington, DE, USA) and checked for integrity with gel electrophoresis (1%) and on the Advanced Analytical Technologies Fragment Analyzer (Agilent Technologies, Inc., CA, USA) (RIN>7.0). Samples were normalized to a concentration of 150 ng/μL each for subsequent analyses. A total of 28 probeset identifiers (Integrated DNA Technologies, Inc., IL, USA) associated with lipid metabolism and inflammation in the liver, together with a set of reference genes (Table S4), was submitted to NanoString Technologies, Inc. (Seattle, WA, USA) for a custom codeset creation and transcript count. Reporter code count (RCC) output files were processed using the nSolver analysis software (version 4.0) for quality control, background correction and normalization using negative controls and eight housekeeping genes (*Ppia*, *Hprt*, *Rpl19*, *Sdha*, *Tubb*, *Abcf1*, *Gusb* and *Alas1*), and the data obtained was used to compare differences between groups. The counts represented on the bar graphs refer to the expression levels of the analyzed mRNA.

Aorta gene expression—Whole aorta was excised and immediately placed into ice-cold TRIzol Reagent and grinded with a pestle. RNA was then extracted using the TRIzol Reagent protocol, quantified using the NanoDrop ND-1000 spectrophotometer (NanoDrop Technologies Inc., Wilmington, DE, USA) and checked for integrity with gel electrophoresis (1%) and on the Advanced Analytical Technologies Fragment Analyzer (Agilent Technologies, Inc., CA, USA) (RIN>7.0). Samples were normalized to a concentration of 50 ng/μL each and were submitted for single-end sequencing to the Beijing Genomics Institute (Cambridge, MA, USA) following standard protocols. Library products were sequenced using a BGISEQ-50, and bioinformatics analysis was performed as previously described using NextFlow computational pipeline.[160] RNA (at a concentration of 50 ng/μL per sample) was also submitted to NanoString Technologies, Inc. (Seattle, WA, USA) together with a total of 39 probeset identifiers and reference genes (Integrated DNA Technologies, Inc., IL, USA) (Table S5) for a custom codeset creation and transcript count. Reporter code count (RCC) output files were processed using the nSolver analysis software (version 4.0) for quality control, background correction, and normalization using negative controls and housekeeping genes. Data obtained was used to compare differences between groups.

Flow cytometry (FACS)—Single-cell suspensions from whole blood, spleen, bone marrow and aorta were prepared separately as follows (see below for aorta digestion). Briefly, spleens were minced in 4–5 mL of RPMI 1640 medium supplemented with 2% fetal bovine serum (FBS) and then passed through a 70 μm micron cell strainer to remove tissue clumps; bone marrow was flushed from femurs of mice with 1 mL of RPMI 1640 medium supplemented with 2% FBS using a 26G needle, resuspended using gentle pipetting, and passed through a 70 μm micron cell strainer to remove clumps; and blood was collected from cardiac puncture, transferred into EDTA tubes and centrifuged at 650 × *g*, 25 min at 4°C to collect plasma. All cell suspensions were treated with ACK lysing buffer as per the manufacturer's instructions and resuspended in FACS buffer (PBS, 0.1% bovine serum albumin, 0.5% FBS). Following, cells (2×10^5) were incubated with TruStain FcX (anti-mouse CD16/32) antibody for 25 min on ice, centrifuged (300 × *g*, 5 min, 4°C), and resuspended in 50 μL FACS buffer and 50 μL of fluorochrome conjugated antibody mix for 30 min. Cells were then washed twice with FACS buffer and resuspended in 300 μL FACS for analysis. Cells were acquired on either the BD LSR II or BD LSRFortessa equipped with 5 lasers and 18 detector filters. Data were analyzed using FlowJo V10 (FlowJo, LLC) and specific cell populations were identified using the gating strategies described in Figures 1G–H, S1I–S1K, and S7A. Details of all antibodies and reagents can be found in the key resources table.

Seahorse analysis—BMDMs were isolated and differentiated in Teflon wells as described above. On day 6, 150k/well of BMDMs were seeded into a 24-well Seahorse XF Cell Culture Microplate and allowed to attach for 3 h. The cells were then incubated overnight with 100 μM ITA-LNP or Ctrl-LNP, with or without 1ug/mL LPS. The next day, cells were washed and equilibrated in base DMEM supplemented with 5 mM HEPES and 2 mM L-glutamine, but without glucose and pyruvate. The assay was conducted using the Glycolysis Stress Test template provided by Agilent, with sequential injections of 100 mM glucose, 100 μM oligomycin, and 500 mM 2-DG.

Tissue culture of aorta organoids in the presence of ^{13}C glucose—Aortas (including aortic root, ascending aorta, aortic arch, and descending aorta) were excised and carefully cleaned of all adjoining lymph nodes, cut lengthwise and immediately immersed in tissue culture medium containing Dulbecco's Modified Eagle Medium (DMEM, no sodium pyruvate, glucose, sodium bicarbonate and glutamine), 10% dialyzed fetal bovine serum, 1000 U/mL penicillin-streptomycin, 2 mM glutamine, 3.7 g/L sodium bicarbonate and 1000 mg/L uniformly-labeled [U-^{13}C] glucose (details in key resources table). The tissue organoids were incubated for 24 h in 25 cm^2 tissue-culture flasks with gentle rocking at 37°C and 5% carbon dioxide atmosphere. Next, the tissue was thoroughly rinsed in phosphate buffered saline (3 × 20 mL) and blotted with filter paper to remove the buffer excess. The tissue was flash-frozen in liquid nitrogen and stored at −80°C until pulverization, quenching, and metabolite extraction.

Metabolite extraction of aortas—Samples were quenched and extracted as previously described using methodology developed by the Resource Center for Stable Isotope-Resolved Metabolomics (RC-SIRM) at the University of Kentucky.[67,68,161–163] Frozen aorta samples

were pulverized in liquid nitrogen using a Spex Freezer Mill (SPEX SamplePrep, Metuchen, NJ, USA). A fraction (20–50 mg) of the pulverized tissue was quenched in 2 mL cold acetonitrile, 0.75 mL of water and 0.75 mL of Tris-HCl buffer (0.2 mM Tris-HCl, pH 8.0), to which 1 mL of chloroform was added to result in a 2:1.5:1 mixture of acetonitrile:water:chloroform. Samples were vigorously shaken and vortexed for at least 3 min followed by centrifugation (20 min at 3,000 × *g*, 4°C) that resulted in phase separation. The top polar layer (acetonitrile, water) and the bottom lipid layers (chloroform, water) were collected in separate tubes, while the remaining interphase tissue protein was separated and washed with methanol via centrifugation (10 min, 2 × 10,000 *g*, 200 μL each). The tissue protein obtained was dissolved and analyzed for total protein content for normalization of metabolites. Polar fractions were lyophilized and stored at −80°C until analysis via NMR or IC-MS as described below. Tissue culture supernatants (100 μL) were quenched in 400 μL ice-cold acetone and the insoluble protein fraction was separated via centrifugation (10 min × 20,000 *g*). The supernatant was transferred into another tube, flash frozen in liquid nitrogen, and lyophilized.

Nuclear magnetic resonance metabolomics—Polar extracts were reconstituted in deuterium oxide (D_2O) (>99.9%) containing 0.1 mM ethylenediaminetetraacetic acid and 0.5 mM d6–2,2-dimethyl-2-silapentane-5-sulfonate (DSS) followed by 1D 1H and 1H (^{13}C) HSQC (heteronuclear single quantum coherence or heteronuclear single quantum correlation) NMR on a 14.1 Tesla NMR spectrometer (Agilent Technologies, CA) equipped with a 3 mm inverse triple resonance HCN cryoprobe. 1D 1H spectra were acquired with standard PRESAT pulse sequence at 15°C. The acquisition parameters were: 16384 data points, 2 s acquisition time, 512 transients, 12 ppm spectral width, and 4 s recycle delay time. The spectra were linear predicted and zero filled to 128 k points and apodized with 1 Hz exponential line broadening. 1D HSQC spectra were acquired with ^{13}C adiabatic decoupling and parameters as follows: 0.25 s acquisition time, 1796 data points, 1024 transients, 12 ppm spectral width. The HSQC spectra were then apodized with unshifted Gaussian function and 4 Hz exponential line broadening and zero filling to 16 k data points before Fourier transformation. Metabolites were assigned by comparison with in-house[164] and public (Human Metabolome Database, http://www.hmdb.ca/), and commercial (ChenomX, Edmonton, Alberta, Canada) NMR databases. Metabolites and their ^{13}C isotopomers were assigned and quantified using the MestReNova software (Mestrelab, Spain) and ChenomX. The peak intensities of metabolites obtained were converted into nmoles by calibration against the peak intensity of DSS (27.5 nmol) at 0 ppm for 1H spectra. HSQC spectra were normalized using lactate satellites as previously described.[161,164] Metabolite amounts were normalized to total protein content.

Ion chromatography-mass spectrometry metabolomics—Polar extracts for IC-MS were reconstituted in 20 μL ultrapure deionized water of which 10 μL was injected for IC-MS. All analyses were performed on a Dionex ICS-5000+ ion chromatography interfaced to a Thermo Fusion Orbitrap Tribrid mass spectrometer (Thermo Fisher Scientific) as previously described.[165,166] Isotopologue peak areas were integrated and exported to Microsoft Excel via the Thermo TraceFinder (version 3.3) software package. Natural abundance correction of peak areas was performed using the method developed by Moseley

HN.[167] Fractional enrichment was calculated as the percentage of the natural abundance corrected signal of each isotopologue from the sum of all isotopologues within a certain metabolite and averaged across all replicates. Selected metabolites were quantified using an external standard mixture with known concentration of a given metabolite.

Protein quantification—The protein pellet obtained after acetonitrile:chloroform extraction was homogenized in a 2% sodium dodecyl sulfate (SDS), 62.5 mM Tris, and 1 mM dithiothreitol (DTT), pH 6.8 buffer followed by protein quantification using the bicinchoninic acid (BCA) assay. The colorimetric detection was performed in a 96-well format using Molecular Devices i3 plate reader and a wavelength of 562 nm.

Synthesis of itaconate conjugates and corresponding nanoparticles

Ptd Ethylene Glycol - ITA synthesis: 40.2 mg itaconic anhydride (0.359 mmol, 1.1 mol eq) and 250 mg (0.326 mmol) of 18:1 Ptd Ethylene Glycol (Avanti Polar Lipids 870302) were mixed in 6 mL absolute dichloromethane in a 50 mL dry Schlenk flask. The liquid was stirred with a magnet simultaneously with addition of 100 μL boron trifluoride tetrahydrofuran complex (Sigma-Aldrich 434280). The flask was filled with dry nitrogen gas and kept stirring overnight at room temperature. Next, to that solution 30–40 mL of dry acetonitrile was then added. The white precipitate was formed. The mixture was then placed at −20°C overnight. The precipitate was then separated by centrifugation (3500 g, 2 min, 4°C) and the acetonitrile was discarded. This re-precipitation was repeated 2 times and the residue was dried in a high vacuum yielding 199 mg of Ptd Ethylene Glycol - ITA (63%).

ITA-LNP nanoparticle synthesis and fluorescent labeling: The Ptd Ethylene Glycol - ITA powder was resuspended at 10 mg/mL (12.6 mM) in water and then pH-adjusted with 1 M NaOH slowly while stirring until pH is ~7.2. The mixture was stirred for 30 min and the pH was adjusted to ~7.2 with additional few drops of 0.1 M NaOH. The mixture was then sonicated at max power at 20°C for 20 min using QSonica Sonicator Q2000 with a bath probe until the solution turned clear. The solution was vortexed with 10x PBS to a final 1x PBS concentration as adjusted to the volume, and then sonicated again for 5 min. The solution was filter-sterilized through 0.2 μm PES membrane. In some experiments, ITA-LNP were labeled with Atto647 fluorochrome: 100 μL (1 mg/mL) of DPPE-Atto647 (Atto-Tech GmbH, AD 647–155) in chloroform was added to a 15 mL Falcon tube and the solvent was evaporated. 100 mg of Ptd Ethylene Glycol - ITA was then added and the nanoparticles were produced as described above. To produce “Koded” cells *in vivo* as described in Figure 6, the final formulation was supplemented with 1 mol% FSL-biotin (Sigma Aldrich).

Synthesis of Na-ITA-LNP, OI-LNP-pc, OI-LNP-ps, and OI-LNP-pg lipid nanoparticles: Nanoparticles were prepared via standard lipid film hydration technique using lipids and surfactants found in literature to formulate and stabilize particles.[168–172] Briefly, the lipids and cholesterol at a molar percentages indicated in Table S2 were dissolved in chloroform, the solvent was evaporated under nitrogen gas, and the resulting lipid film was hydrated with a 10 mM PBS buffer or 100 mM sodium itaconate (ITA) in water (for Na-ITA-LNP). The mixture was sonicated at maximum power at 4°C using Sonica Sonicator Q2000 with a bath probe until the solution turned clear. Next, the

nanoparticles were extruded through 100 nm Nuclepore membranes at 60°C using a hand-held syringe-based extruder (Avanti Polar Lipids). The unincorporated sodium ITA was then separated from the nanoparticles using dialysis (20 kDa MWCO cellulose membrane). The amount of ITA in Na-ITA-LNP was determined after nanoparticle breakdown in acetonitrile (50 μL of nanoparticles mixed with 250 μL of acetonitrile) followed by HPLC to analyze ITA concentration. The amount of ITA incorporated in the OI-based nanoparticles was determined as follows. First, a 100 μL of the corresponding nanoparticles was mixed with 100 μL 5 M NaOH and the solution was stirred at 4°C overnight to completely saponify the lipids and hydrolyze OI into sodium ITA. The hydroxide was then neutralized with an equimolar hydrochloric acid and the concentration of ITA was determined using HPLC.

Nanoparticle characterization: The nanoparticles were characterized using dynamic light scattering using the Zetasizer Nano ZS instrument (Malvern Instruments). Nanoparticles were diluted in water at 0.01% and standard latex SOP was used. At least 15 measurement cycles were used for each sample. To determine lipid concentration in nanoparticle preparations, lipids were precipitated from an aliquot of nanoparticles by addition of 10 volumes of acetone and incubated at −80°C for at least 1 h. Next, the precipitate was separated using centrifugation (31,000 g × 10 min, 4°C) and the supernatant was removed. The lipid concentration was then analyzed using Stewart lipid assay as previously described.[173,174]

Cryo transmission electron microscopy (Cryo-TEM) was performed to analyze nanoparticle shape and diameter. One drop of nanoarticle formulation was added to glow-discharged holey carbon/formvar film coated grids in a controlled environment vitrification system at constant humidity and temperature of 25°C. The samples were blotted and frozen hydrated by plunging into a bath of liquid ethane slush. They were stored under liquid nitrogen temperature until transfer to Gatan cryo-holder operating at 176°C and imaged in low-dose mode with FEI Tecnai G2 Spirit TEM equipped with bioTWIN optics operating at 120 kV. Images were recorded using a Gatan CCD camera equipped with a post column Gatan energy filter (GIF).

Biodistribution of ITA-LNP—ITA-LNP was labeled with Atto647 as described above to allow for fluorescence detection in isolated organs. *LDLr*$^{-/-}$ male mice of 8 weeks of age were fed with HCHFD for 12, 20 and 28 weeks and briefly switched on Alfalfa free diet (Inotiv) for 1 week prior to the imaging. The mice were fasted overnight (12 h) and injected with 30 mg/kg of Atto647-labeled ITA-LNP retro-orbitally. One hour after the injection, the animals were euthanized and perfused in a reduced light environment through the left ventricle with cold PBS-citrate buffer (10 mM PBS containing 11 mM trisodium citrate, pH 7.2) for at least 5 min. The major organs including whole aorta (cut in an *en face* preparation) were then excised and immediately imaged using Azure C400 reader equipped with Cy5 fluorescence filter. The same aortas were next stained with Oil Red O and photographed for comparative localization of the ITA-LNP signal and lipid accumulation. Quantification was performed on organs after pulverizing them in liquid nitrogen, extraction of the Atto647 fluorochrome with chloroform and analysis of the extracts on a fluorescence

plate reader (630 excitation and 647 emission). The resulting relative fluorescence units (RFU) were normalized to total protein content from the same tissue.

Cell isolation and culture—IL-1β Reporter HEK 293 Cells (Invivogen), RAW 264.7 (ATCC), THP1, and iBMDMs were cultured as per vendor recommendations. See key resources table for specific identifiers.

Bone marrow cells were isolated from mice by flushing the femurs and tibias with PBS. Cells were cultured in Teflon flasks in 30mL of Dulbecco's Modified Eagle's Medium (DMEM) containing 10% fetal bovine serum, 1% MEM Non-essential Amino Acid Solution, 1% antibiotic-antimycotic and 40 ng/ml Mouse M-CSF for 6 days to differentiate them into macrophages (bone marrow derived macrophages, BMDM).

Neutrophil isolation: Mice femurs and tibias were flushed using a syringe containing RPMI. The bone marrow cell suspension was filtered using 100 μM falcon cell strainer and centrifuged for 7 min at 1400 rpm at 4°C. The pellet was lysed with 20 mL of 0.2% saline for 20 s. Afterward, 20 mL of 1.6% saline solution was added. The suspension was centrifuged in the aforementioned conditions. The pellet was resuspended in 1 mL RPMI, layered on the top of a histopaque gradient (3mL of histopaque 1119, 3mL of histopaque 1077), and centrifuged for 30 min 2000 rpm, 22°C (acceleration 3, deceleration 0). The bottom white band was collected and resuspended in 20 mL of RPMI and centrifuged for 7 min at 1400 rpm 4°C. After washing, cells were plated.

Hepatocyte isolation: Perfusion buffer (0.9% Sodium Chloride, 20 mM HEPES, 5 mM Calcium Chloride, 1% BSA) was prepared and kept in a water bath (42°C) during all surgery. C57BL/6 Mice were anesthetized (Ketamine 20 mg/mL and xylazine 7.5 mg/mL mouse cocktail, 5 mL/kg) before a flap of skin was cut across the lower rib cage and the intestines were moved to the left side to expose the portal vein. The catheter was inserted into the portal vein and fixed with threads. Then the abdominal IVC was cut. The liver was perfused with a warm perfusion buffer using a peristaltic pump at a rate of 20 mL/min for 2 min until the liver was blanched. The cotton applicators were used to squeeze the effluent blood vessel to inflate the liver a few times to ensure all the blood drained out. This was followed by perfusion with a collagenase solution (0.9% Sodium Chloride, 20 mM HEPES, 5 mM Calcium Chloride, 1% BSA, 1 mg/mL Collagenase H) at a rate of 4 mL/min for 10 min. The liver was extracted and resuspended in a collagenase solution to yield a cell suspension. The liver cell suspension was resuspended in a perfusion buffer and filtered through a 40 μm filter and centrifuged at 60 × g for 5 min 4°C. After three wash cycles, the cells were resuspended in 10 mL of warm Dulbecco's Modified Eagle's Medium (DMEM) containing 10% fetal bovine serum and 1% Penicillin-Streptomycin, plated in collagen-coated plates and incubated for 3–4 h at 37°C in 5% CO_2. After the cells attached, the media was changed to William's Medium E containing 8 μg/mL gentamicin, 1% NEAA, 1% Anti-anti, 1% glutamine and 50 nM dexamethasone.

GSH/GSSG and NADPH/NADP measurements—BMDMS were differentiated as described above and then treated with 100 μM ITA- or Ctrl-LNP for 24 h. The respective Promega kits were used to measure GSH/GSSG and NADPH/NADP levels.

Gene expression analysis via quantitative PCR—For qRT-PCR, cells were lysed in Trizol and RNA was isolated using Direct-zol RNA Miniprep Kit (Zymo Research). Concentrations of total RNA were quantified by NanoDrop spectrophotometry. cDNA was synthesized from 250 ng total RNA using a High-Capacity cDNA Reverse Transcription Kit (Thermo Fisher Scientific). qRT-PCR was carried out using TaqMan Fast Advanced Master Mix and TaqMan probes in a Roche LightCycler 480 system. Fold change was calculated by the ΔΔCT method and normalized to housekeeping genes *Gapdh* and *Actb*.

Immunoblot assays (western blot)—Cells were lysed in 2x Laemmli SDS loading buffer (4% SDS, 0.1 M DTT, 6.25% Ficoll, 1x protease inhibitor cocktail and 0.001% bromophenol blue) and boiled at 95°C for 5 min. Direct Detect Infrared Spectrometer (Millipore) was used to measure protein concentration. Cell lysates were loaded into a Bio Rad TGX Criterion (4–20%) gel and resolved at 300 V in Tris-Glycine running buffer. Proteins were transferred on PVDF membranes using the BioRad TransBlot Turbo. After transfer, membranes were incubated in pre-cooled acetone for 30 min with the subsequent drying at 50°C for 30 min. The membranes were hydrated in PBS, blocked in 5% nonfat dry milk in Tris-buffered saline containing 0.05% Tween 20 (TBS-T), probed overnight at 4°C with primary antibodies as indicated in key resources table. The membranes were washed in TBS-T and incubated with secondary antibodies for 1 h at room temperature. The Azure C400 western blot imaging system was used for visualization of the proteins of interest.

IRG1 knockdown via shRNA overexpression—iBMDMs cells were seeded in 0.75 M/well in 24-well plates and incubated overnight. The media was then changed to media containing 5 or 10 μg/mL of polybrene. On the day of infection, cells were about 50% confluent. The cells were treated in duplicates with lentiviruses encoding IRG1 shRNA or cop-GFP control (both from Santa Cruz Biotechnology) at three different concentrations (1, 2 and 4 μL). After 24 h of incubation, the media was changed to media without polybrene. Puromycin dihydrochloride was used for selecting the most stable clones by incubating cells in media containing infected cells that were grown in media containing 10 μg/mL puromycin for one week. Western blot was used to determine the success of the knockdown.

IL-1β reporter assays in THP1 cells—The assays were performed according to the manufacturer's instructions (Invivogen). THP1 cells were seeded 0.5 M/well in 96-well plates in RPMI media and treated with different concentrations of 4-octyl itaconate (OI) and ITA-LNP overnight. The cells were then treated with 100 ng/mL LPS overnight.The cells were then treated with monosodium urate crystals (MSU, Invivogen) at 1 μg/mL and incubated overnight. The 50 μL of media was then collected and added to IL-1β Reporter HEK cells, which were seeded 0.05 M/well in 96-well plates and cultured according to the manufacturer's instructions. After an overnight incubation, 20 μL of the media was transferred to a new 96 well plate and mixed with 180 μL of QUANTI-Blue Solution (Invivogen). The plate was incubated at 37°C for 1 h and the optical density was detected at a wavelength of 650 nm.

In vitro analysis in IRG1-KD iBMDMs and BMDMs

Unfolded protein response: iBMDMs and BMDMs were seeded in DMEM containing 1% BSA and 1% Penicillin-Streptomycin. The media for iBMDMs additionally contained 10 μg/mL puromycin. Cells were treated with DMSO, ACAT-inhibitor (ACATi, CP-113818), CD-Cholesterol, or ACATi with CD-Cholesterol simultaneously. After 48 h of incubation, the cells were lysed in a 2x Laemmli SDS loading buffer. Immunoblotting was performed as described above. The cells were seeded at a density of 0.3 M/well in 24-well plates and allowed to attach overnight. The media was then changed to the media containing 10% human lipoprotein-depleted serum and treated with PBS; 5 μg/mL ACATi; 100 μg/mL oxLDL, ACATi and oxLDL; 10 μg/ml CD-cholesterol, ACATi and CD-cholesterol; 1 μg/mL Tunicamycin; or 100 μg/mL LPS. After 24 h, the cells were lysed in Trizol, and qPCR was performed as described above.

Inflammasome assays: BMDMs were seeded at a density of 0.7 M/well in 24-well plates. After the cells attached, they were treated overnight with the indicated concentrations of ITA-LNP, Ctrl-LNP or PBS. The following day, the media was changed to Opti-MEM without serum and the cells were treated with PBS or 50 ng/mL ultrapure LPS (List Biological Labs) for 3 h. The cells were then treated with 5 μM Nigericin. After 1 h of incubation, the supernatant was collected and the cells were lysed in a 2x Laemmli SDS loading buffer. Cell lysates (15 μg/lane) and supernatant (50 μL/well) were loaded to Bio Rad TGX Criterion (4–20%) 12-well gels. Immunoblotting was performed as described above.

Immunofluorescence studies in human plaque—Human aortic tissue was obtained from autopsy specimens under exemptions granted by the Institutional Review Boards at CVPath Institute (Gaithersburg, MD). Immunohistochemical stains were performed using anti-IRG1 mAb (key resources table). Anti-IRG1 mAb was validated in house using cell validation treatment and overexpression experiments (Figures S3I, and S3J). Human coronary specimens were formalin-fixed and paraffin embedded and cut at 5 μm on glass slides. Following standard deparaffinization and hydration, the slides were processed using a Leica Bond system via standard protocol as previously described by us.[175,176] The sections were pre-treated using heat mediated antigen retrieval with Tris-EDTA buffer at pH 9 for 20 min. The sections were then incubated with anti-IRG1 mAb or anti-CD68 at dilutions indicated in key resources table for 45 min at room temperature and detected using anti-mouse Alexa Fluor 488 (to detect CD68) or anti-rabbit Alexa Fluor 647 (to detect IRG1). The sections were then counter-stained with DAPI and mounted with Mowiol aqueous mounting media. The fluorescence was visualized by confocal microscopy (Zeiss LSM800).

Immunofluorescence and immunohistochemistry studies in mouse atherosclerosis—For immunofluorescence studies in mouse brachiocephalic artery (BCA) and aortic root, 10 μm pre-dried frozen sections were fixed by immersion in acetone for 10 min at −20°C, drying and rehydrating. Blocking and staining with primary and fluorochrome-conjugated secondary antibodies was accomplished as described previously.[159,177] The antibodies and the dilutions that were used in this work are listed in key resources table. Vectashield mounting medium with DAPI (Vector Laboratories) was

used to stain nuclei and mount the slides. In some experiments, colorimetric detection of antigens was performed according to standard protocols and manufacturer's instructions. In brief, the slides were exposed to primary antibodies as above, washed and processed with an ImmPRESS HRP Horse Anti-Rabbit IgG PLUS Polymer Kit (Vector Laboratories), followed by the detection using ImmPACT DAB EqV Substrate (Vector Laboratories).

Image analysis—Whole organ fluorescence was analyzed using ImageJ/Fiji, an open source image analysis software. In brief, the images were first color inverted and the ROIs were created by tracing each organ. The integrated intensity of fluorescence per ROI area was then determined using the "Analysis" function in ImageJ. After autofluorescence subtraction, the values of each organ were normalized to the value of liver from the same animal. The analysis of Mac3 and αSMA expression plaque was performed using Keyence BZ-X analyzer and a Hybrid Cell Count plugin. First, the area of analysis was identified using the "Same Intensity" function and then the "Cell Separation" function was used to outline individual fluorescence+ or DAB+ cells. The number of such cells was next counted in each slide using a premade macro function and a "Macro cell count" module. Ten slides at different histopathological locations (30 μm difference between slides) were analyzed per mouse/condition.

Koded Cells RNA-seq (kc-RNA-seq)—The pooled aortas (three tissues per pool from 9 animals per group) from "koded" ITA-LNP and Ctrl-LNP injected animals were digested in an enzyme cocktail in RPMI as previously described by us.[159] The enzymatic reaction was quenched with 3% BSA in PBS containing 0.3 mM EDTA. The cell suspension was passed through a 100 μm cell strainer, washed with the buffer and incubated with streptavidin magnetic beads on ice (Thermo Fisher Dynabeads M-280). Dynabeads M-280 were specifically selected over other commercially available beads because it has been previously shown that they are most suitable for cell capture under a variety of conditions. Dynabeads M-280 resulted in highest cell viability, specific capture and the highest nucleic acid yield.[178] Importantly, the large size of Dynabeads M-280 is not conducive for non-specific engulfment by phagocytic cells at 4°C. The incubation proceeded for 10 min on ice under gentle tube rotation following which the cells were separated with a magnet. The negative fraction (the cells that did not bind to the magnet) and the positive fraction (Dynabeads-bound cells) were separated. The Dynabeads-bound cells were washed three times with PBS containing 1% BSA and then lysed in Trizol under vigorous repeat pipetting and the RNA was isolated as described above. Bulk RNA sequencing was performed as described above.

Tandem stenosis model—Mice were divided into two groups: 1) sham (460 μm stenosis) and 2) experimental tandem stenosis surgery (150 μm stenosis). 8 (4 and 4) were used for tissue histology to demonstrate unstable plaque phenotype. 8 mice/group were used for scRNA-Seq analysis using pooled aortic segments. 10–15 mice per group were used for gross pathology analysis and downstream immunofluorescence analysis of tissue sections.

At 6 weeks of age, $ApoE^{-/-}$ mice were initiated on an HCHFD (Evigo TD 88137). At 12 weeks of age, they underwent tandem stenosis surgery as previously described[124] and were sacrificed after 6 weeks of therapy as indicated above and in the main manuscript. Mice

were operated on according to the following protocol. Using the dissecting microscope, a small incision (~1 cm) was made on the skin directly midline over the trachea. The connective tissue was bluntly dissected underneath the skin using curved forceps. A segment of the left common carotid artery was exposed. The common carotid artery was lifted up and bluntly dissected away from the surrounding tissue. The vagus nerve was identified and separated from the common carotid artery. Vascular stenosis was induced by suturing two points on the common carotid using 6–0 blue braided polyester fiber (Ti-cron). Distal point is defined as 1 mm from the carotid bifurcation. Proximal point is defined as 3 mm from the distal point. Carotid stenosis was performed by tying the carotid against a probe made of a needle. For 150 μm stenosis, a 8–0 Ethilon needle, and for 460 μm stenosis, a 26 G needle was used. A surgeon's knot was tied over the probe with moderate tightness and one relatively loose above it before removal. Blood flow distal to suture was confirmed. Any excess filament was cut. The wound was closed using a 6–0 monofilament suture in the single interrupted method. 500 μL saline bolus was then given i.v. Mice were monitored to ensure recovery from anesthesia. Buprenorphine at 0.1 mg/kg was administered subcutaneously (SQ) as mice awakened postoperatively. The mice were monitored closely for the next 48 h administering buprenorphine at 0.05 mg/kg SQ 8–12 h with 2 extra doses post 48 h as needed.

Single-cell RNA sequencing

Sample preparation: *ApoE*$^{-/-}$ mice with tandem stenosis (see above) were euthanized followed by perfusion with cold PBS/citrate buffer containing 1 μg/mL Actinomycin D. The aortic segments were extracted and carefully processed by removing all lymph nodes. The pooled aortic segments (8 from both ITA-LNP and Ctrl-LNP injected animals) were then digested in an enzyme cocktail in RPMI containing 1 μg/mL Actinomycin D as previously described by us.[159] The enzymatic reaction was quenched with 3% BSA in PBS containing 0.3 mM EDTA and 1 μg/mL Actinomycin D. The cell suspension was passed through a 100 μm filter, washed with the buffer and the cell viability was determined. Next, the cells were labeled with anti-CD45 fluorochrome-labeled antibodies and live/dead staining and separated using FACS as described above. After FACS separation, viable CD45^{+} cells were kept on ice in a PBS buffer containing 1% BSA and 1 μg/mL Actinomycin D until scRNA-seq using the 10x Genomic platform as previously described by us.[179]

Sequencing: Briefly, the 10x Genomics Chromium Next GEM Single Cell 5′ Kit v2 was used to process cell suspensions for 5′ gene expression profiling. The cell suspension volumes were calculated for a target cell recovery of 10,000 cells and loaded on the chromium controller per manufacturer's guidelines. The resultant cDNAs were quantified and assessed on the Agilent Bioanalyzer using the high-sensitivity DNA kit. The final single cell 5′ libraries were quantified using the Qubit dsDNA high sensitivity and qualitatively evaluated on the Agilent Bioanalyzer using the high-sensitivity DNA kit. Libraries were sequenced on an Illumina NovaSeq 6000 under recommended settings (PE26×90 with 10 bp dual index) targeting 50,000 PE reads per target cell equivalent.

Preprocessing and quality control: The raw scRNA-seq fastq files were processed using Cell Ranger from 10X Genomics Technology and aligned to mm10 reference genome. All

expression matrices were loaded into R version 4.1.2 (R Foundation) using the "Read10X" function from the Seurat library version 4.1.0.[180] The Seurat library was also used to perform the analyses. The expression matrices from two separate samples (ITA-LNP and Ctrl-LNP injected animals) were combined into one Seurat object prior to preprocessing, transformation, and analysis. Pre-processing removed cells with fewer than 200 genes, greater than 6000 genes, or displaying more than 10% mitochondrial transcripts to filter out low-quality cells. The "SCTransform" function from the Seurat library was applied to transform the expression matrices via normalization and variance stabilization on each sample.[181]

Integration: To allow comparison between two groups, the expression matrices were integrated via the "FindIntegrationAnchors" Seurat function prior to principal component analysis (PCA) dimension reduction with 50 principal components and subsequent UMAP dimensional reduction. Clusters were identified in an unsupervised manner via shared nearest neighbor modularity optimization-based Louvain clustering algorithm using a resolution parameter of 0.5.

Differential expression analysis: This was conducted via the "FindMarkers" Seurat function, where the Wilcoxon Rank-Sum Test and thresholding criteria of logFC >1 or < −1 and a Bonferroni-adjusted $p < 0.05$ to identify differentially expressed genes between and within groups and conditions. All statistical comparison of scRNA-seq DEGs, and canonical pathway analysis cell clusters was performed with ingenuity pathway analysis by Qiagen. UMAP visualizations were created using the "DimPlot" and "FeaturePlot" Seurat functions. Volcano plots were created using the ggplot2 library of functions.

H3K27ac chromatin immunoprecipitation sequencing (ChIP-seq)

Sample preparation: C57BL/6 mice of 8 weeks of age ($n = 3$ per group) were bolus injected with either ITA- or Ctrl-LNP at 30 mg/kg. The mice were euthanized 24 h later and the bone marrow was isolated as described above. The whole bone marrow cells were then fixed with 1% paraformaldehyde for 10 min at room temperature. The cross-linked chromatin was sonicated to shear chromatin into fragments of 200–600 bp using the Diagenode Bioruptor Pico sonication device according to the manufacturer's instruction. The sheared chromatin was immunoprecipitated with 1 μg of anti-H3K27ac ChIP grade rabbit polyclonal antibody (Millipore Sigma) with rabbit IgG used as a negative control. The immunoprecipitates were captured using Protein A/G Dynabeads (Thermo Fisher). The genomic DNA was then eluted with the DNA elution buffer and analyzed for integrity using Agilent Bioanalyzer as described above. DNA library preparation and sequencing was performed by Beijing Genomics Institute (Cambridge, MA, USA) following standard protocols and using Illumina TruSeq Chip Library Kit.

ChIP-seq data processing: The sequencing reads from Illumina HiSeq were aligned to the mouse genome (mm10) using the BOWTIE alignment tool.[182] These aligned reads were then processed and converted into bam/bai (http://genome.ucsc.edu/goldenPath/help/bam.html) format, and then loaded in the Integrative Genomics Viewer (http://www.broadinstitute.org/igv/) for visualization as previously described by us.[183] The

processing steps involved removing duplicate reads and format conversions using SAMtools suite.[184] Once the peaks were obtained for all the tracks, the common peaks and genes between these tracks were removed by BEDtools[185] intersect command.

QUANTIFICATION AND STATISTICAL ANALYSIS

For all experiments, data was first tested for normality using the Shapiro-Wilk test and for equality of variances using Bartlett's test. If it was determined that the normality and equality of variances are satisfied ($p \leq 0.05$), the group means were compared using Student's t-test (for 2 groups) or ANOVA with Tukey's *post-hoc* test (>2 groups). In some experiments with >2 groups, pairwise t test was applied with Holm *post-hoc* test. The particular statistical analysis employed is indicated in the figure legends of the main manuscript. For non-normally distributed data or data with unequal variances, nonparametric Mann-Whitney U-test (2 groups) was used. The statistical analysis was performed using R version 4.3.0 ("Already Tomorrow") or later. Graphs and plots were created using Plotly Chart Studio or with R packages tidyverse/ggplot2. The results are presented as mean with standard error of mean (SEM). The SEM values are displayed as error bars in the figures or values following plus-minus sign in the main text.

Supplementary Material

Refer to Web version on PubMed Central for supplementary material.

ACKNOWLEDGMENTS

This work was supported by the National Heart, Lung, and Blood Institute, grants HL130516 and HL155450 to A.M. N.E.H. was supported by CWRU MSTP training program funded to CWRU by NIH grant numbers T32GM007250 and T32GM152319. A.A.P. was supported by The Valour Foundation, as the Rebecca E. Barchas, MD, Professor in Translational Psychiatry of Case Western Reserve University, the Morley-Mather Chair in Neuropsychiatry of University Hospitals of Cleveland Medical Center, and the Louis Stokes VA Medical Center resources and facilities.

REFERENCES

1. GBD 2015 DALYs and HALE Collaborators (2016). Global, regional, and national disability-adjusted life-years (DALYs) for 315 diseases and injuries and healthy life expectancy (HALE), 1990–2015: a systematic analysis for the Global Burden of Disease Study 2015. Lancet 388, 1603–1658. 10.1016/S0140-6736(16)31460-X. [PubMed: 27733283]
2. Roth GA, Mensah GA, Johnson CO, Addolorato G, Ammirati E, Baddour LM, Barengo NC, Beaton AZ, Benjamin EJ, Benziger CP, et al. (2020). Global Burden of Cardiovascular Diseases and Risk Factors, 1990–2019: Update From the GBD 2019 Study. J. Am. Coll. Cardiol. 76, 2982–3021. 10.1016/j.jacc.2020.11.010. [PubMed: 33309175]
3. Low Wang CC, Hess CN, Hiatt WR, and Goldfine AB (2016). Clinical Update: Cardiovascular Disease in Diabetes Mellitus: Atherosclerotic Cardiovascular Disease and Heart Failure in Type 2 Diabetes Mellitus - Mechanisms, Management, and Clinical Considerations. Circulation 133, 2459–2502. 10.1161/CIRCULATIONAHA.116.022194. [PubMed: 27297342]
4. Pahwa R, and Jialal I (2022). Atherosclerosis (StatPearls Publishing).
5. Everett BM (2019). Residual inflammatory risk: A common and important risk factor for recurrent cardiovascular events. J. Am. Coll. Cardiol. 73, 2410–2412. 10.1016/j.jacc.2019.02.056. [PubMed: 31097160]
6. Joseph P, Roshandel G, Gao P, Pais P, Lonn E, Xavier D, Avezum A, Zhu J, Liu L, Sliwa K, et al. (2021). Fixed-dose combination therapies with and without aspirin for primary prevention

of cardiovascular disease: an individual participant data meta-analysis. Lancet 398, 1133–1146. 10.1016/S0140-6736(21)01827-4. [PubMed: 34469765]

7. Libby P, Ridker PM, and Maseri A (2002). Inflammation and atherosclerosis. Circulation 105, 1135–1143. 10.1161/hc0902.104353. [PubMed: 11877368]
8. Ridker PM, Everett BM, Thuren T, MacFadyen JG, Chang WH, Ballantyne C, Fonseca F, Nicolau J, Koenig W, Anker SD, et al. (2017). Antiinflammatory Therapy with Canakinumab for Atherosclerotic Disease. N. Engl. J. Med. 377, 1119–1131. 10.1056/NEJMoa1707914. [PubMed: 28845751]
9. Sirimarco G, Labreuche J, Bruckert E, Goldstein LB, Fox KM, Rothwell PM, Amarenco P, Bousser MG, Chamorro A, Ford I, et al. (2014). Atherogenic dyslipidemia and residual cardiovascular risk in statin-treated patients. Stroke 45, 1429–1436. 10.1161/STROKEAHA.113.004229. [PubMed: 24736236]
10. Wong ND, Zhao Y, Quek RGW, Blumenthal RS, Budoff MJ, Cushman M, Garg P, Sandfort V, Tsai M, and Lopez JAG (2017). Residual atherosclerotic cardiovascular disease risk in statin-treated adults: The Multi-Ethnic Study of Atherosclerosis. J. Clin. Lipidol. 11, 1223–1233. 10.1016/j.jacl.2017.06.015. [PubMed: 28754224]
11. Ramkumar N, Martinez-Camblor P, Columbo JA, Osborne NH, Goodney PP, and O'Malley AJ (2019). Adverse Events After Atherectomy: Analyzing Long-Term Outcomes of Endovascular Lower Extremity Revascularization Techniques. J. Am. Heart Assoc. 8, e012081. 10.1161/JAHA.119.012081. [PubMed: 31165658]
12. Soehnlein O, and Libby P (2021). Targeting inflammation in atherosclerosis - from experimental insights to the clinic. Nat. Rev. Drug Discov. 20, 589–610. 10.1038/s41573-021-00198-1. [PubMed: 33976384]
13. Zhao L, Zhang S, Su Q, and Li S (2021). Effects of withdrawing an atherogenic diet on the atherosclerotic plaque in rabbits. Exp. Ther. Med. 22, 751. 10.3892/etm.2021.10183. [PubMed: 34035848]
14. Verhamme P, Quarck R, Hao H, Knaapen M, Dymarkowski S, Bernar H, Van Cleemput J, Janssens S, Vermylen J, Gabbiani G, et al. (2002). Dietary cholesterol withdrawal reduces vascular inflammation and induces coronary plaque stabilization in miniature pigs. Cardiovasc. Res. 56, 135–144. 10.1016/s0008-6363(02)00515-1. [PubMed: 12237174]
15. Daoud AS, Jarmolych J, Augustyn JM, and Fritz KE (1981). Sequential morphologic studies of regression of advanced atherosclerosis. Arch. Pathol. Lab Med. 105, 233–239. [PubMed: 6894365]
16. Armstrong ML, Warner ED, and Connor WE (1970). Regression of coronary atheromatosis in rhesus monkeys. Circ. Res. 27, 59–67. 10.1161/01.res.27.1.59. [PubMed: 4987450]
17. Armstrong ML (1976). Evidence of regression of atherosclerosis in primates and man. Postgrad. Med. 52, 456–461. 10.1136/pgmj.52.609.456.
18. Aikawa M, and Libby P (2000). Lipid lowering reduces proteolytic and prothrombotic potential in rabbit atheroma. Ann. N. Y. Acad. Sci. 902, 140–152. 10.1111/j.1749-6632.2000.tb06309.x. [PubMed: 10865834]
19. McConnell MV, Aikawa M, Maier SE, Ganz P, Libby P, and Lee RT (1999). MRI of rabbit atherosclerosis in response to dietary cholesterol lowering. Arterioscler. Thromb. Vasc. Biol. 19, 1956–1959. 10.1161/01.atv.19.8.1956. [PubMed: 10446077]
20. Badimon JJ, Badimon L, and Fuster V (1990). Regression of atherosclerotic lesions by high density lipoprotein plasma fraction in the cholesterol-fed rabbit. J. Clin. Invest. 85, 1234–1241. 10.1172/JCI114558. [PubMed: 2318976]
21. Li J, Lee DH, Hu J, Tabung FK, Li Y, Bhupathiraju SN, Rimm EB, Rexrode KM, Manson JE, Willett WC, et al. (2020). Dietary Inflammatory Potential and Risk of Cardiovascular Disease Among Men and Women in the U.S. J. Am. Coll. Cardiol. 76, 2181–2193. 10.1016/j.jacc.2020.09.535. [PubMed: 33153576]
22. Lichtenstein AH, Appel LJ, Vadiveloo M, Hu FB, Kris-Etherton PM, Rebholz CM, Sacks FM, Thorndike AN, Van Horn L, and Wylie-Rosett J (2021). 2021 Dietary Guidance to Improve Cardiovascular Health: A Scientific Statement From the American Heart Association. Circulation 144, e472–e487. 10.1161/CIR.0000000000001031. [PubMed: 34724806]

23. Mattavelli E, Olmastroni E, Redaelli L, Grigore L, Pellegatta F, Magni P, Casula M, Catapano A, and Baragetti A (2023). Assessment of Mediterranean diet adherence changes over time in the general population. Atherosclerosis 379, S127. 10.1016/j.athero-sclerosis.2023.06.440.
24. Shai I, Spence JD, Schwarzfuchs D, Henkin Y, Parraga G, Rudich A, Fenster A, Mallett C, Liel-Cohen N, Tirosh A, et al. (2010). Dietary intervention to reverse carotid atherosclerosis. Circulation 121, 1200–1208. 10.1161/CIRCULATIONAHA.109.879254. [PubMed: 20194883]
25. Baratta F, Angelico F, and Del Ben M (2023). Challenges in Improving Adherence to Diet and Drug Treatment in Hypercholesterolemia Patients. Int. J. Environ. Res. Publ. Health 20, 5878. 10.3390/ijerph20105878.
26. Barrett TJ (2020). Macrophages in Atherosclerosis Regression. Arterioscler. Thromb. Vasc. Biol. 40, 20–33. 10.1161/ATV-BAHA.119.312802. [PubMed: 31722535]
27. Moore KJ, Sheedy FJ, and Fisher EA (2013). Macrophages in atherosclerosis: a dynamic balance. Nat. Rev. Immunol. 13, 709–721. 10.1038/nri3520. [PubMed: 23995626]
28. Theofilis P, Oikonomou E, Tsioufis K, and Tousoulis D (2023). The Role of Macrophages in Atherosclerosis: Pathophysiologic Mechanisms and Treatment Considerations. Int. J. Mol. Sci. 24, 9568. 10.3390/ijms24119568. [PubMed: 37298518]
29. Deftereos SG, Beerkens FJ, Shah B, Giannopoulos G, Vrachatis DA, Giotaki SG, Siasos G, Nicolas J, Arnott C, Patel S, et al. (2022). Colchicine in Cardiovascular Disease: In-Depth Review. Circulation 145, 61–78. 10.1161/CIRCULATIONAHA.121.056171. [PubMed: 34965168]
30. Banach M, and Penson PE (2021). Colchicine and Cardiovascular Outcomes: a Critical Appraisal of Recent Studies. Curr. Atherosclerosis Rep. 23, 32. 10.1007/s11883-021-00932-5.
31. Nelson K, Fuster V, and Ridker PM (2023). Low-dose colchicine for secondary prevention of coronary artery disease: JACC review topic of the week. J. Am. Coll. Cardiol. 82, 648–660. 10.1016/j.jacc.2023.05.055. [PubMed: 37558377]
32. Ma Z, Chen J, Jin K, and Chen X (2022). Colchicine and coronary heart disease risks: A meta-analysis of randomized controlled clinical trials. Front. Cardiovasc. Med. 9, 947959. 10.3389/fcvm.2022.947959. [PubMed: 36176989]
33. Dhindsa DS, Sandesara PB, Shapiro MD, and Wong ND (2020). The Evolving Understanding and Approach to Residual Cardiovascular Risk Management. Front. Cardiovasc. Med. 7, 88. 10.3389/fcvm.2020.00088. [PubMed: 32478100]
34. Wierda RJ, Geutskens SB, Jukema JW, Quax PHA, and van den Elsen PJ (2010). Epigenetics in atherosclerosis and inflammation. J. Cell Mol. Med. 14, 1225–1240. 10.1111/j.1582-4934.2010.01022.x. [PubMed: 20132414]
35. Yang S-S, Zhang R, Wang G, and Zhang Y-F (2017). The development prospection of HDAC inhibitors as a potential therapeutic direction in Alzheimer's disease. Transl. Neurodegener. 6, 19. 10.1186/s40035-017-0089-1. [PubMed: 28702178]
36. Bondarev AD, Attwood MM, Jonsson J, Chubarev VN, Tarasov VV, and Schiöth HB (2021). Recent developments of HDAC inhibitors: Emerging indications and novel molecules. Br. J. Clin. Pharmacol. 87, 4577–4597. 10.1111/bcp.14889. [PubMed: 33971031]
37. Markus HS (2023). HDAC9 Inhibition as a Novel Treatment for Stroke. Stroke 54, 3182–3189. 10.1161/STROKEAHA.123.044862. [PubMed: 37942644]
38. Basu D, and Bornfeldt KE (2020). Hypertriglyceridemia and Atherosclerosis: Using Human Research to Guide Mechanistic Studies in Animal Models. Front. Endocrinol. 11, 504. 10.3389/fendo.2020.00504.
39. Getz GS, and Reardon CA (2016). Do the Apoe−/− and Ldlr−/− Mice Yield the Same Insight on Atherogenesis? Arterioscler. Thromb. Vasc. Biol. 36, 1734–1741. 10.1161/ATVBAHA.116.306874. [PubMed: 27386935]
40. Ilyas I, Little PJ, Liu Z, Xu Y, Kamato D, Berk BC, Weng J, and Xu S (2022). Mouse models of atherosclerosis in translational research. Trends Pharmacol. Sci. 43, 920–939. 10.1016/j.tips.2022.06.009. [PubMed: 35902281]
41. Michelucci A, Cordes T, Ghelfi J, Pailot A, Reiling N, Goldmann O, Binz T, Wegner A, Tallam A, Rausell A, et al. (2013). Immune-responsive gene 1 protein links metabolism to immunity by catalyzing itaconic acid production. Proc. Natl. Acad. Sci. USA 110, 7820–7825. 10.1073/pnas.1218599110. [PubMed: 23610393]

42. Swain A, Bambouskova M, Kim H, Andhey PS, Duncan D, Auclair K, Chubukov V, Simons DM, Roddy TP, Stewart KM, and Artyomov MN (2020). Comparative evaluation of itaconate and its derivatives reveals divergent inflammasome and type I interferon regulation in macrophages. Nat. Metab. 2, 594–602. 10.1038/s42255-020-0210-0. [PubMed: 32694786]
43. Song J, Zhang Y, Frieler RA, Andren A, Wood S, Tyrrell DJ, Sajjakulnukit P, Deng JC, Lyssiotis CA, Mortensen RM, et al. (2023). Itaconate suppresses atherosclerosis by activating a Nrf2-dependent antiinflammatory response in macrophages in mice. J. Clin. Invest. 134. 10.1172/JCI173034.
44. Cyr Y, Bozal FK, Barcia Durá n JG, Newman AAC, Amadori L, Smyrnis P, Gourvest M, Das D, Gildea M, Kaur R, et al. (2024). The IRG1-itaconate axis protects from cholesterol-induced inflammation and atherosclerosis. Proc. Natl. Acad. Sci. USA 121, e2400675121. 10.1073/pnas.2400675121. [PubMed: 38564634]
45. Bambouskova M, Gorvel L, Lampropoulou V, Sergushichev A, Loginicheva E, Johnson K, Korenfeld D, Mathyer ME, Kim H, Huang L-H, et al. (2018). Electrophilic properties of itaconate and derivatives regulate the IkBz-ATF3 inflammatory axis. Nature 556, 501–504. 10.1038/s41586-018-0052-z. [PubMed: 29670287]
46. ElAzzouny M, Tom CT, Evans CR, Olson LL, Tanga MJ, Gallagher KA, Martin BR, and Burant CF (2017). Dimethyl Itaconate Is Not Metabolized into Itaconate Intracellularly. J. Biol. Chem. 292, 4766–4769. 10.1074/jbc.C117.775270. [PubMed: 28188288]
47. Yang W, Wang Y, Tao K, and Li R (2023). Metabolite itaconate in host immunoregulation and defense. Cell. Mol. Biol. Lett. 28, 100. 10.1186/s11658-023-00503-3. [PubMed: 38042791]
48. Pullinger CR, Eng C, Salen G, Shefer S, Batta AK, Erickson SK, Verhagen A, Rivera CR, Mulvihill SJ, Malloy MJ, and Kane JP (2002). Human cholesterol 7alpha-hydroxylase (CYP7A1) deficiency has a hypercholesterolemic phenotype. J. Clin. Invest. 110, 109–117. 10.1172/JCI15387. [PubMed: 12093894]
49. Tian K, Xu Y, Sahebkar A, and Xu S (2020). CD36 in Atherosclerosis: Pathophysiological Mechanisms and Therapeutic Implications. Curr. Atherosclerosis Rep. 22, 59. 10.1007/s11883-020-00870-8.
50. Hilgendorf I, Swirski FK, and Robbins CS (2015). Monocyte fate in atherosclerosis. Arterioscler. Thromb. Vasc. Biol. 35, 272–279. 10.1161/ATVBAHA.114.303565. [PubMed: 25538208]
51. Kratofil RM, Kubes P, and Deniset JF (2017). Monocyte Conversion During Inflammation and Injury. Arterioscler. Thromb. Vasc. Biol. 37, 35–42. 10.1161/ATVBAHA.116.308198. [PubMed: 27765768]
52. Auffray C, Sieweke MH, and Geissmann F (2009). Blood monocytes: development, heterogeneity, and relationship with dendritic cells. Annu. Rev. Immunol. 27, 669–692. 10.1146/annurev.immunol.021908.132557. [PubMed: 19132917]
53. Tacke F, Alvarez D, Kaplan TJ, Jakubzick C, Spanbroek R, Llodra J, Garin A, Liu J, Mack M, van Rooijen N, et al. (2007). Monocyte subsets differentially employ CCR2, CCR5, and CX3CR1 to accumulate within atherosclerotic plaques. J. Clin. Invest. 117, 185–194. 10.1172/JCI28549. [PubMed: 17200718]
54. Nahrendorf M, Swirski FK, Aikawa E, Stangenberg L, Wurdinger T, Figueiredo J-L, Libby P, Weissleder R, and Pittet MJ (2007). The healing myocardium sequentially mobilizes two monocyte subsets with divergent and complementary functions. J. Exp. Med. 204, 3037–3047. 10.1084/jem.20070885. [PubMed: 18025128]
55. Gonzalez-Ramos S, Fernández-García V, Recalde M, Rodríguez C, Marínez-González J, Andrés V, Martín-Sanz P, and Boscá L (2020). Deletion or Inhibition of NOD1 Favors Plaque Stability and Attenuates Atherothrombosis in Advanced Atherogenesis. Cells 9, 2067. 10.3390/cells9092067. [PubMed: 32927803]
56. Poels K, van Leent MMT, Reiche ME, Kusters PJH, Huveneers S, de Winther MPJ, Mulder WJM, Lutgens E, and Seijkens TTP (2020). Antibody-Mediated Inhibition of CTLA4 Aggravates Atherosclerotic Plaque Inflammation and Progression in Hyperlipidemic Mice. Cells 9, 1987. 10.3390/cells9091987. [PubMed: 32872393]
57. Kawai K, Tsuno NH, Matsuhashi M, Kitayama J, Osada T, Yamada J, Tsuchiya T, Yoneyama S, Watanabe T, Takahashi K, and Nagawa H (2005). CD11b-mediated migratory property of

peripheral blood B cells. J. Allergy Clin. Immunol. 116, 192–197. 10.1016/j.jaci.2005.03.021. [PubMed: 15990794]

58. Yang H, Parkhouse RME, and Wileman T (2005). Monoclonal antibodies that identify the CD3 molecules expressed specifically at the surface of porcine gammadelta-T cells. Immunology 115, 189–196. 10.1111/j.1365-2567.2005.02137.x. [PubMed: 15885124]
59. Wang S, Song R, Wang Z, Jing Z, Wang S, and Ma J (2018). S100A8/A9 in Inflammation. Front. Immunol. 9, 1298. 10.3389/fimmu.2018.01298. [PubMed: 29942307]
60. Durrington PN, Bashir B, and Soran H (2023). Paraoxonase 1 and atherosclerosis. Front. Cardiovasc. Med. 10, 1065967. 10.3389/fcvm.2023.1065967. [PubMed: 36873390]
61. Mai W, and Liao Y (2020). Targeting IL-1β in the Treatment of Atherosclerosis. Front. Immunol. 11, 589654. 10.3389/fimmu.2020.589654. [PubMed: 33362770]
62. Ridker PM, and Rane M (2021). Interleukin-6 Signaling and Anti-Interleukin-6 Therapeutics in Cardiovascular Disease. Circ. Res. 128, 1728–1746. 10.1161/CIRCRESAHA.121.319077. [PubMed: 33998272]
63. Zandbergen F, and Plutzky J (2007). PPARalpha in atherosclerosis and inflammation. Biochim. Biophys. Acta 1771, 972–982. 10.016/j.bbalip.2007.04.021. [PubMed: 17631413]
64. Alonso-Piñeiro JA, Gonzalez-Rovira A, Sánchez-Gomar I, Moreno JA, and Durán-Ruiz MC (2021). Nrf2 and Heme Oxygenase-1 Involvement in Atherosclerosis Related Oxidative Stress. Antioxidants 10, 1463. 10.3390/antiox10091463. [PubMed: 34573095]
65. Dzobo KE, Hanford KML, and Kroon J (2021). Vascular Metabolism as Driver of Atherosclerosis: Linking Endothelial Metabolism to Inflammation. Immunometabolism 3, e210020. 10.20900/immunometab20210020. [PubMed: 34084561]
66. Leung SWS, and Shi Y (2022). The glycolytic process in endothelial cells and its implications. Acta Pharmacol. Sin. 43, 251–259. 10.1038/s41401-021-00647-y. [PubMed: 33850277]
67. Fan TW-M, and Lane AN (2011). NMR-based stable isotope resolved metabolomics in systems biochemistry. J. Biomol. NMR 49, 267–280. 10.1007/s10858-011-9484-6. [PubMed: 21350847]
68. Fan TW-M, Lane AN, and Higashi RM (2016). Stable Isotope Resolved Metabolomics Studies in *Ex Vivo* TIssue Slices. Bio. Protoc. 6, e1730.
69. Reyes-Caballero H, Rao X, Sun Q, Warmoes MO, Lin P, Sussan TE, Park B, Fan TW-M, Maiseyeu A, Rajagopalan S, et al. (2019). Air pollution-derived particulate matter dysregulates hepatic Krebs cycle, glucose and lipid metabolism in mice. Sci. Rep. 9, 17423. 10.1038/s41598-019-53716-y. [PubMed: 31757983]
70. Luan HH, and Medzhitov R (2016). Food Fight: Role of Itaconate and Other Metabolites in Antimicrobial Defense. Cell Metabol. 24, 379–387. 10.1016/j.cmet.2016.08.013.
71. Strelko CL, Lu W, Dufort FJ, Seyfried TN, Chiles TC, Rabinowitz JD, and Roberts MF (2011). Itaconic acid is a mammalian metabolite induced during macrophage activation. J. Am. Chem. Soc. 133, 16386–16389. 10.1021/ja2070889. [PubMed: 21919507]
72. Heng TSP, Painter MW, Elpek K, Lukacs-Kornek V, Mauermann N, Turley SJ, Koller D, Kim FS, Wagers AJ, Asinovski N, et al. (2008). The Immunological Genome Project: networks of gene expression in immune cells. Nat. Immunol. 9, 1091–1094. 10.1038/ni1008-1091. [PubMed: 18800157]
73. Wirka RC, Wagh D, Paik DT, Pjanic M, Nguyen T, Miller CL, Kundu R, Nagao M, Coller J, Koyano TK, et al. (2019). Atheroprotective roles of smooth muscle cell phenotypic modulation and the TCF21 disease gene as revealed by single-cell analysis. Nat. Med. 25, 1280–1289. 10.1038/s41591-019-0512-5. [PubMed: 31359001]
74. Willemsen L, and de Winther MP (2020). Macrophage subsets in atherosclerosis as defined by single-cell technologies. J. Pathol. 250, 705–714. 10.1002/path.5392. [PubMed: 32003464]
75. Finn AV, Nakano M, Narula J, Kolodgie FD, and Virmani R (2010). Concept of vulnerable/unstable plaque. Arterioscler. Thromb. Vasc. Biol. 30, 1282–1292. 10.1161/ATVBAHA.108.179739. [PubMed: 20554950]
76. Peace CG, and O'Neill LA (2022). The role of itaconate in host defense and inflammation. J. Clin. Invest. 132, e148548. 10.1172/JCI148548. [PubMed: 35040439]
77. Lougheed M, Moore ED, Scriven DR, and Steinbrecher UP (1999). Uptake of oxidized LDL by macrophages differs from that of acetyl LDL and leads to expansion of an acidic endolysosomal

compartment. Arterioscler. Thromb. Vasc. Biol. 19, 1881–1890. 10.1161/01.atv.19.8.1881. [PubMed: 10446066]

78. Nagy L, Tontonoz P, Alvarez JG, Chen H, and Evans RM (1998). Oxidized LDL regulates macrophage gene expression through ligand activation of PPARgamma. Cell 93, 229–240. 10.1016/s0092-8674(00)81574-3. [PubMed: 9568715]
79. Chellan B, Reardon CA, Getz GS, and Hofmann Bowman MA (2016). Enzymatically Modified Low-Density Lipoprotein Promotes Foam Cell Formation in Smooth Muscle Cells via Macropinocytosis and Enhances Receptor-Mediated Uptake of Oxidized Low-Density Lipoprotein. Arterioscler. Thromb. Vasc. Biol. 36, 1101–1113. 10.1161/ATVBAHA.116.307306. [PubMed: 27079883]
80. Fong LG, Fong TA, and Cooper AD (1991). Inhibition of lipopolysaccharide-induced interleukin-1 beta mRNA expression in mouse macrophages by oxidized low density lipoprotein. J. Lipid Res. 32, 1899–1910. [PubMed: 1816321]
81. Ting KKY, Yu P, Dow R, Floro E, Ibrahim H, Scipione CA, Hyduk SJ, Polenz CK, Zaslaver O, Karmaus PWF, et al. (2023). Oxidized Low-Density Lipoprotein Accumulation Suppresses Glycolysis and Attenuates the Macrophage Inflammatory Response by Diverting Transcription from the HIF-1α to the Nrf2 Pathway. J. Immunol. 211, 1561–1577. 10.4049/jimmunol.2300293. [PubMed: 37756544]
82. Tabas I (2002). Consequences of cellular cholesterol accumulation: basic concepts and physiological implications. J. Clin. Invest. 110, 905–911. 10.1172/JCI16452. [PubMed: 12370266]
83. Sakashita N, Chang CCY, Lei X, Fujiwara Y, Takeya M, and Chang T-Y (2010). Cholesterol loading in macrophages stimulates formation of ER-derived vesicles with elevated ACAT1 activity. J. Lipid Res. 51, 1263–1272. 10.1194/jlr.M900288. [PubMed: 20460577]
84. Jerome WG, Cox BE, Griffin EE, and Ullery JC (2008). Lysosomal cholesterol accumulation inhibits subsequent hydrolysis of lipoprotein cholesteryl ester. Microsc. Microanal. 14, 138–149. 10.1017/S1431927608080069. [PubMed: 18312718]
85. Feng B, Yao PM, Li Y, Devlin CM, Zhang D, Harding HP, Sweeney M, Rong JX, Kuriakose G, Fisher EA, et al. (2003). The endoplasmic reticulum is the site of cholesterol-induced cytotoxicity in macrophages. Nat. Cell Biol. 5, 781–792. 10.1038/ncb1035. [PubMed: 12907943]
86. Kellner-Weibel G, Yancey PG, Jerome WG, Walser T, Mason RP, Phillips MC, and Rothblat GH (1999). Crystallization of free cholesterol in model macrophage foam cells. Arterioscler. Thromb. Vasc. Biol. 19, 1891–1898. 10.1161/01.atv.19.8.1891. [PubMed: 10446067]
87. Su YR, Dove DE, Major AS, Hasty AH, Boone B, Linton MF, and Fazio S (2005). Reduced ABCA1-mediated cholesterol efflux and accelerated atherosclerosis in apolipoprotein E-deficient mice lacking macrophage-derived ACAT1. Circulation 111, 2373–2381. 10.1161/01.CIR.0000164236.19860.13. [PubMed: 15851589]
88. Dove DE, Su YR, Zhang W, Jerome WG, Swift LL, Linton MF, and Fazio S (2005). ACAT1 deficiency disrupts cholesterol efflux and alters cellular morphology in macrophages. Arterioscler. Thromb. Vasc. Biol. 25, 128–134. 10.1161/01.ATV.0000148323.94021.e5. [PubMed: 15499044]
89. Linton MF, and Fazio S (2003). Macrophages, inflammation, and atherosclerosis. Int. J. Obes. 27, S35–S40. 10.1038/sj.ijo.0802498.
90. Mills EL, Ryan DG, Prag HA, Dikovskaya D, Menon D, Zaslona Z, Jedrychowski MP, Costa ASH, Higgins M, Hams E, et al. (2018). Itaconate is an anti-inflammatory metabolite that activates Nrf2 via alkylation of KEAP1. Nature 556, 113–117. 10.1038/nature25986. [PubMed: 29590092]
91. Booth AN, Taylor J, Wilson RH, and Deeds F (1952). The inhibitory effects of itaconic acid in vitro and in vivo. J. Biol. Chem. 195, 697–702. [PubMed: 14946179]
92. Hooftman A, Angiari S, Hester S, Corcoran SE, Runtsch MC, Ling C, Ruzek MC, Slivka PF, McGettrick AF, Banahan K, et al. (2020). The Immunomodulatory Metabolite Itaconate Modifies NLRP3 and Inhibits Inflammasome Activation. Cell Metabol. 32, 468–478.e7. 10.1016/j.cmet.2020.07.016.
93. Liu P, Chen G, and Zhang J (2022). A Review of Liposomes as a Drug Delivery System: Current Status of Approved Products, Regulatory Environments, and Future Perspectives. Molecules 27, 1372. 10.3390/molecules27041372. [PubMed: 35209162]

94. Kelly C, Jefferies C, and Cryan S-A (2011). Targeted liposomal drug delivery to monocytes and macrophages. J. Drug Deliv. 2011, 727241. 10.1155/2011/727241. [PubMed: 21512579]

95. Dong H, Pang L, Cong H, Shen Y, and Yu B (2019). Application and design of esterase-responsive nanoparticles for cancer therapy. Drug Deliv. 26, 416–432. 10.1080/10717544.2019.1588424. [PubMed: 30929527]

96. Ehinger JK, Piel S, Ford R, Karlsson M, Sjövall F, Frostner EÅ, Morota S, Taylor RW, Turnbull DM, Cornell C, et al. (2016). Cell-permeable succinate prodrugs bypass mitochondrial complex I deficiency. Nat. Commun. 7, 12317. 10.1038/ncomms12317. [PubMed: 27502960]

97. Lang T, Lee JPW, Elgass K, Pinar AA, Tate MD, Aitken EH, Fan H, Creed SJ, Deen NS, Traore DAK, et al. (2018). Macrophage migration inhibitory factor is required for NLRP3 inflammasome activation. Nat. Commun. 9, 2223. 10.1038/s41467-018-04581-2. [PubMed: 29884801]

98. Karasawa T, and Takahashi M (2017). Role of NLRP3 Inflammasomes in Atherosclerosis. J. Atherosclerosis Thromb. 24, 443–451. 10.5551/jat.RV17001.

99. Schroder K, Zhou R, and Tschopp J (2010). The NLRP3 inflammasome: a sensor for metabolic danger? Science 327, 296–300. 10.1126/science.1184003. [PubMed: 20075245]

100. Zhang B, Chen H, Ouyang J, Xie Y, Chen L, Tan Q, Du X, Su N, Ni Z, and Chen L (2019). SQSTM1-dependent autophagic degradation of PKM2 inhibits the production of mature IL1B/IL-1β and contributes to LIPUS-mediated anti-inflammatory effect. Autophagy 16, 1262–1278. 10.1080/15548627.2019.1664705. [PubMed: 31500508]

101. Mog B, Asase C, Chaplin A, Gao H, Rajagopalan S, and Maiseyeu A (2019). Nano-Antagonist Alleviates Inflammation and Allows for MRI of Atherosclerosis. Nanotheranostics 3, 342–355. 10.7150/ntno.37391. [PubMed: 31723548]

102. Lampropoulou V, Sergushichev A, Bambouskova M, Nair S, Vincent EE, Loginicheva E, Cervantes-Barragan L, Ma X, Huang SC-C, Griss T, et al. (2016). Itaconate Links Inhibition of Succinate Dehydrogenase with Macrophage Metabolic Remodeling and Regulation of Inflammation. Cell Metabol. 24, 158–166. 10.1016/j.cmet.2016.06.004.

103. Burczyk G, Cichon I, and Kolaczkowska E (2022). Itaconate Suppresses Formation of Neutrophil Extracellular Traps (NETs): Involvement of Hypoxia-Inducible Factor 1a (Hif-1α) and Heme Oxygenase (HO-1). Front. Immunol. 13, 864638. 10.3389/fimmu.2022.864638. [PubMed: 35837403]

104. Yin S, and Cao W (2015). Toll-Like Receptor Signaling Induces Nrf2 Pathway Activation through p62-Triggered Keap1 Degradation. Mol. Cell Biol. 35, 2673–2683. 10.1128/MCB.00105-15. [PubMed: 26012548]

105. Diotallevi M, Ayaz F, Nicol T, and Crabtree MJ (2021). Itaconate as an inflammatory mediator and therapeutic target in cardiovascular medicine. Biochem. Soc. Trans. 49, 2189–2198. 10.1042/BST20210269. [PubMed: 34665229]

106. Zhu X, Guo Y, Liu Z, Yang J, Tang H, and Wang Y (2021). Itaconic acid exerts anti-inflammatory and antibacterial effects via promoting pentose phosphate pathway to produce ROS. Sci. Rep. 11, 18173. 10.1038/s41598-021-97352-x. [PubMed: 34518559]

107. Puckett DL, Alquraishi M, Chowanadisai W, and Bettaieb A (2021). The Role of PKM2 in Metabolic Reprogramming: Insights into the Regulatory Roles of Non-Coding RNAs. Int. J. Mol. Sci. 22, 1171. 10.3390/ijms22031171. [PubMed: 33503959]

108. Anderson R, Pladna KM, Schramm NJ, Wheeler FB, Kridel S, and Pardee TS (2023). Pyruvate Dehydrogenase Inhibition Leads to Decreased Glycolysis, Increased Reliance on Gluconeogenesis and Alternative Sources of Acetyl-CoA in Acute Myeloid Leukemia. Cancers 15, 484. 10.3390/cancers15020484. [PubMed: 36672433]

109. Song G, Liu J, Zhao Z, Yu Y, Tian H, Yao S, Li G, and Qin S (2011). Simvastatin reduces atherogenesis and promotes the expression of hepatic genes associated with reverse cholesterol transport in apoE-knockout mice fed high-fat diet. Lipids Health Dis. 10, 8. 10.1186/1476-511X-10-8. [PubMed: 21241519]

110. Bea F, Blessing E, Bennett B, Levitz M, Wallace EP, and Rosenfeld ME (2002). Simvastatin promotes atherosclerotic plaque stability in apoE-deficient mice independently of lipid lowering. Arterioscler. Thromb. Vasc. Biol. 22, 1832–1837. 10.1161/01.atv.0000036081.01231.16. [PubMed: 12426212]

111. Wang YX, Martin-McNulty B, Huw LY, da Cunha V, Post J, Hinchman J, Vergona R, Sullivan ME, Dole W, and Kauser K (2002). Anti-atherosclerotic effect of simvastatin depends on the presence of apolipoprotein E. Atherosclerosis 162, 23–31. 10.1016/s0021-9150(01)00678-5. [PubMed: 11947894]

112. Ritskes-Hoitinga M, Tobin G, Jensen TL, and Mikkelsen LF (2012). Chapter 4.3 - Nutrition of the Laboratory Mouse. In The Laboratory Mouse, Second Edition, Hedrich HJ, ed. (Academic Press), pp. 567–599. 10.1016/B978-0-12-382008-2.00024-6.

113. Gomez D, Baylis RA, Durgin BG, Newman AAC, Alencar GF, Mahan S, St Hilaire C, Müller W, Waisman A, Francis SE, et al. (2018). Interleukin-1b has atheroprotective effects in advanced atherosclerotic lesions of mice. Nat. Med. 24, 1418–1429. 10.1038/s41591-018-0124-5. [PubMed: 30038218]

114. Lin J, Ren J, Gao DS, Dai Y, and Yu L (2021). The Emerging Application of Itaconate: Promising Molecular Targets and Therapeutic Opportunities. Front. Chem. 9, 669308. 10.3389/fchem.2021.669308. [PubMed: 34055739]

115. Yanasarn N, Sloat BR, and Cui Z (2009). Nanoparticles engineered from lecithin-in-water emulsions as a potential delivery system for docetaxel. Int. J. Pharm. X. 379, 174–180. 10.1016/j.ijpharm.2009.06.004.

116. Henry S, Williams E, Barr K, Korchagina E, Tuzikov A, Ilyushina N, Abayzeed SA, Webb KF, and Bovin N (2018). Rapid one-step biotinylation of biological and non-biological surfaces. Sci. Rep. 8, 2845. 10.1038/s41598-018-21186-3. [PubMed: 29434224]

117. Yurdagul A Jr., Subramanian M, Wang X, Crown SB, Ilkayeva OR, Darville L, Kolluru GK, Rymond CC, Gerlach BD, Zheng Z, et al. (2020). Macrophage Metabolism of Apoptotic Cell-Derived Arginine Promotes Continual Efferocytosis and Resolution of Injury. Cell Metabol. 31, 518–533.e10. 10.1016/j.cmet.2020.01.001.

118. Liao X, Sluimer JC, Wang Y, Subramanian M, Brown K, Pattison JS, Robbins J, Martinez J, and Tabas I (2012). Macrophage autophagy plays a protective role in advanced atherosclerosis. Cell Metabol. 15, 545–553. 10.1016/j.cmet.2012.01.022.

119. Tabas I (2010). Macrophage death and defective inflammation resolution in atherosclerosis. Nat. Rev. Immunol. 10, 36–46. 10.1038/nri2675. [PubMed: 19960040]

120. Ahmadi A, Argulian E, Leipsic J, Newby DE, and Narula J (2019). From Subclinical Atherosclerosis to Plaque Progression and Acute Coronary Events: JACC State-of-the-Art Review. J. Am. Coll. Cardiol. 74, 1608–1617. 10.1016/j.jacc.2019.08.012. [PubMed: 31537271]

121. Caro CG (2009). Discovery of the role of wall shear in atherosclerosis. Arterioscler. Thromb. Vasc. Biol. 29, 158–161. 10.1161/ATVBAHA.108.166736. [PubMed: 19038849]

122. Chen Y-C, Bui AV, Diesch J, Manasseh R, Hausding C, Rivera J, Haviv I, Agrotis A, Htun NM, Jowett J, et al. (2013). A novel mouse model of atherosclerotic plaque instability for drug testing and mechanistic/therapeutic discoveries using gene and microRNA expression profiling. Circ. Res. 113, 252–265. 10.1161/CIRCRE-SAHA.113.301562. [PubMed: 23748430]

123. Oppi S, Lüscher TF, and Stein S (2019). Mouse Models for Atherosclerosis Research—Which Is My Line? Front. Cardiovasc. Med. 6, 46. 10.3389/fcvm.2019.00046. [PubMed: 31032262]

124. Chen YC, Rivera J, and Peter K (2015). Tandem Stenosis to Induce Atherosclerotic Plaque Instability in the Mouse. Methods Mol. Biol. 1339, 333–338. 10.1007/978-1-4939-2929-0_23. [PubMed: 26445800]

125. Blasius AL, Cella M, Maldonado J, Takai T, and Colonna M (2006). Siglec-H is an IPC-specific receptor that modulates type I IFN secretion through DAP12. Blood 107, 2474–2476. 10.1182/blood-2005-09-3746. [PubMed: 16293595]

126. Crocker PR, Paulson JC, and Varki A (2007). Siglecs and their roles in the immune system. Nat. Rev. Immunol. 7, 255–266. 10.1038/nri2056. [PubMed: 17380156]

127. Papaspyridonos M, Smith A, Burnand KG, Taylor P, Padayachee S, Suckling KE, James CH, Greaves DR, and Patel L (2006). Novel candidate genes in unstable areas of human atherosclerotic plaques. Arterioscler. Thromb. Vasc. Biol. 26, 1837–1844. 10.1161/01.ATV.0000229695.68416.76. [PubMed: 16741146]

128. Versari D, Herrmann J, Gössl M, Mannheim D, Sattler K, Meyer FB, Lerman LO, and Lerman A (2006). Dysregulation of the ubiquitin-proteasome system in human carotid atherosclerosis.

Arterioscler. Thromb. Vasc. Biol. 26, 2132–2139. 10.1161/01.ATV.0000232501.08576.73. [PubMed: 16778122]

129. Zhi X, and Chen C (2012). WWP1: a versatile ubiquitin E3 ligase in signaling and diseases. Cell. Mol. Life Sci. 69, 1425–1434. 10.1007/s00018-011-0871-7. [PubMed: 22051607]
130. Tsantilas P, Lao S, Wu Z, Eberhard A, Winski G, Vaerst M, Nanda V, Wang Y, Kojima Y, Ye J, et al. (2021). Chitinase 3 like 1 is a regulator of smooth muscle cell physiology and atherosclerotic lesion stability. Cardiovasc. Res. 117, 2767–2780. 10.1093/cvr/cvab014. [PubMed: 33471078]
131. Khoukaz HB, Ji Y, Braet DJ, Vadali M, Abdelhamid AA, Emal CD, Lawrence DA, and Fay WP (2020). Drug Targeting of Plasminogen Activator Inhibitor-1 Inhibits Metabolic Dysfunction and Atherosclerosis in a Murine Model of Metabolic Syndrome. Arterioscler. Thromb. Vasc. Biol. 40, 1479–1490. 10.1161/ATVBAHA.119.313775. [PubMed: 32268785]
132. Burger PC, and Wagner DD (2003). Platelet P-selectin facilitates atherosclerotic lesion development. Blood 101, 2661–2666. 10.1182/blood-2002-07-2209. [PubMed: 12480714]
133. Li Y-H, Shi G-Y, and Wu H-L (2006). The role of thrombomodulin in atherosclerosis: from bench to bedside. Cardiovasc. Hematol. Agents Med. Chem. 4, 183–187. 10.2174/187152506776369953. [PubMed: 16611051]
134. Cardilo-Reis L, Gruber S, Schreier SM, Drechsler M, Papac-Milicevic N, Weber C, Wagner O, Stangl H, Soehnlein O, and Binder CJ (2012). Interleukin-13 protects from atherosclerosis and modulates plaque composition by skewing the macrophage phenotype. EMBO Mol. Med. 4, 1072–1086. 10.1002/emmm.201201374. [PubMed: 23027612]
135. Proto JD, Doran AC, Gusarova G, Yurdagul A Jr., Sozen E, Subramanian M, Islam MN, Rymond CC, Du J, Hook J, et al. (2018). Regulatory T Cells Promote Macrophage Efferocytosis during Inflammation Resolution. Immunity 49, 666–677.e6. 10.1016/j.immuni.2018.07.015. [PubMed: 30291029]
136. Zhu YP, Padgett L, Dinh HQ, Marcovecchio P, Blatchley A, Wu R, Ehinger E, Kim C, Mikulski Z, Seumois G, et al. (2018). Identification of an Early Unipotent Neutrophil Progenitor with Pro-tumoral Activity in Mouse and Human Bone Marrow. Cell Rep. 24, 2329–2341.e8. 10.1016/j.celrep.2018.07.097. [PubMed: 30157427]
137. Månsson R, Hultquist A, Luc S, Yang L, Anderson K, Kharazi S, Al-Hashmi S, Liuba K, Thoren L, Adolfsson J, et al. (2007). Molecular evidence for hierarchical transcriptional lineage priming in fetal and adult stem cells and multipotent progenitors. Immunity 26, 407–419. 10.1016/j.immuni.2007.02.013. [PubMed: 17433729]
138. Priem B, van Leent MMT, Teunissen AJP, Sofias AM, Mourits VP, Willemsen L, Klein ED, Oosterwijk RS, Meerwaldt AE, Munitz J, et al. (2020). Trained Immunity-Promoting Nanobiologic Therapy Suppresses Tumor Growth and Potentiates Checkpoint Inhibition. Cell 183, 786–801.e19. 10.1016/j.cell.2020.09.059. [PubMed: 33125893]
139. Zhang X, Kang Z, Yin D, and Gao J (2023). Role of neutrophils in different stages of atherosclerosis. Innate Immun. 29, 97–109. 10.1177/17534259231189195. [PubMed: 37491844]
140. Wang B, Zhu X, Kim Y, Li J, Huang S, Saleem S, Li R-C, Xu Y, Dore S, and Cao W (2012). Histone deacetylase inhibition activates transcription factor Nrf2 and protects against cerebral ischemic damage. Free Radic. Biol. Med. 52, 928–936. 10.1016/j.freerad-biomed.2011.12.006. [PubMed: 22226832]
141. Roadmap Epigenomics Consortium; Kundaje A, Meuleman W, Ernst J, Bilenky M, Yen A, Heravi-Moussavi A, Kheradpour P, Zhang Z, Wang J, et al. (2015). Integrative analysis of 111 reference human epigenomes. Nature 518, 317–330. 10.1038/nature14248. [PubMed: 25693563]
142. Creyghton MP, Cheng AW, Welstead GG, Kooistra T, Carey BW, Steine EJ, Hanna J, Lodato MA, Frampton GM, Sharp PA, et al. (2010). Histone H3K27ac separates active from poised enhancers and predicts developmental state. Proc. Natl. Acad. Sci. USA 107, 21931–21936. 10.1073/pnas.1016071107. [PubMed: 21106759]
143. Eash KJ, Greenbaum AM, Gopalan PK, and Link DC (2010). CXCR2 and CXCR4 antagonistically regulate neutrophil trafficking from murine bone marrow. J. Clin. Invest. 120, 2423–2431. 10.1172/JCI41649. [PubMed: 20516641]
144. Sadik CD, Kim ND, and Luster AD (2011). Neutrophils cascading their way to inflammation. Trends Immunol. 32, 452–460. 10.1016/j.it.2011.06.008. [PubMed: 21839682]

145. Feinberg MW, Wara AK, Cao Z, Lebedeva MA, Rosenbauer F, Iwasaki H, Hirai H, Katz JP, Haspel RL, Gray S, et al. (2007). The Kruppel-like factor KLF4 is a critical regulator of monocyte differentiation. EMBO J. 26, 4138–4148. 10.1038/sj.emboj.7601824. [PubMed: 17762869]

146. Basu D, Hu Y, Huggins L-A, Mullick AE, Graham MJ, Wietecha T, Barnhart S, Mogul A, Pfeiffer K, Zirlik A, et al. (2018). Novel Reversible Model of Atherosclerosis and Regression Using Oligonucleotide Regulation of the LDL Receptor. Circ. Res. 122, 560–567. 10.1161/CIRCRESAHA.117.311361. [PubMed: 29321129]

147. Sharma M, Schlegel MP, Afonso MS, Brown EJ, Rahman K, Weinstock A, Sansbury BE, Corr EM, van Solingen C, Koelwyn GJ, et al. (2020). Regulatory T Cells License Macrophage Pro-Resolving Functions During Atherosclerosis Regression. Circ. Res. 127, 335–353. 10.1161/CIRCRESAHA.119.316461. [PubMed: 32336197]

148. Peled M, Nishi H, Weinstock A, Barrett TJ, Zhou F, Quezada A, and Fisher EA (2017). A wild-type mouse-based model for the regression of inflammation in atherosclerosis. PLoS One 12, e0173975. 10.1371/journal.pone.0173975. [PubMed: 28291840]

149. Chereshnev I, Trogan E, Omerhodzic S, Itskovich V, Aguinaldo J-G, Fayad ZA, Fisher EA, and Reis ED (2003). Mouse model of heterotopic aortic arch transplantation. J. Surg. Res. 111, 171–176. 10.1016/s0022-4804(03)00039-8. [PubMed: 12850459]

150. Reis ED, Li J, Fayad ZA, Rong JX, Hansoty D, Aguinaldo JG, Fallon JT, and Fisher EA (2001). Dramatic remodeling of advanced atherosclerotic plaques of the apolipoprotein E-deficient mouse in a novel transplantation model. J. Vasc. Surg. 34, 541–7. 10.1067/mva.2001.115963. [PubMed: 11533609]

151. Trogan E, Feig JE, Dogan S, Rothblat GH, Angeli V, Tacke F, Randolph GJ, and Fisher EA (2006). Gene expression changes in foam cells and the role of chemokine receptor CCR7 during atherosclerosis regression in ApoE-deficient mice. Proc. Natl. Acad. Sci. USA 103, 3781–3786. 10.1073/pnas.0511043103. [PubMed: 16537455]

152. Gustafson HH, Holt-Casper D, Grainger DW, and Ghandehari H (2015). Nanoparticle Uptake: The Phagocyte Problem. Nano Today 10, 487–510. 10.1016/j.nantod.2015.06.006. [PubMed: 26640510]

153. Bagalkot V, Deiuliis JA, Rajagopalan S, and Maiseyeu A (2016). “Eat me” imaging and therapy. Adv. Drug Deliv. Rev. 99, 2–11. 10.1016/j.addr.2016.01.009. [PubMed: 26826436]

154. Levitan I, Volkov S, and Subbaiah PV (2010). Oxidized LDL: diversity, patterns of recognition, and pathophysiology. Antioxidants Redox Signal. 13, 39–75. 10.1089/ars.2009.2733.

155. Di L, and Maiseyeu A (2021). Low-density lipoprotein nanomedicines: mechanisms of targeting, biology, and theranostic potential. Drug Deliv. 28, 408–421. 10.1080/10717544.2021.1886199. [PubMed: 33594923]

156. Jiang Y, Lin W, and Zhu L (2022). Targeted Drug Delivery for the Treatment of Blood Cancers. Molecules 27, 1310. 10.3390/molecules27041310. [PubMed: 35209102]

157. Noz MP, Bekkering S, Groh L, Nielen TM, Lamfers EJ, Schlitzer A, El Messaoudi S, van Royen N, Huys EH, Preijers FW, et al. (2020). Reprogramming of bone marrow myeloid progenitor cells in patients with severe coronary artery disease. Elife 9, e60939. https://doorg/10.7554/eLife.60939. [PubMed: 33168134]

158. Yao L, Heuser-Baker J, Herlea-Pana O, and Barlic-Dicen J (2013). Bone marrow endothelial progenitors in atherosclerotic plaque resolution. Organogenesis 9, 29–33. 10.4161/org.24433. [PubMed: 23538778]

159. Maiseyeu A, Di L, Ravodina A, Barajas-Espinosa A, Sakamoto A, Chaplin A, Zhong J, Gao H, Mignery M, Narula N, et al. (2022). Plaque-targeted, proteolysis-resistant, activatable and MRI-visible nano-GLP-1 receptor agonist targets smooth muscle cell differentiation in atherosclerosis. Theranostics 12, 2741–2757. 10.7150/thno.66456. [PubMed: 35401813]

160. Ewels PA, Peltzer A, Fillinger S, Patel H, Alneberg J, Wilm A, Garcia MU, Di Tommaso P, and Nahnsen S (2020). The nf-core framework for community-curated bioinformatics pipelines. Nat. Biotechnol. 38, 276–278. 10.1038/s41587-020-0439-x. [PubMed: 32055031]

161. Lane AN, Fan TW-M, and Higashi RM (2008). Isotopomer-based metabolomic analysis by NMR and mass spectrometry. Methods Cell Biol. 84, 541–588. 10.1016/S0091-679X(07)84018-0. [PubMed: 17964943]

162. Fan TW-M, Yuan P, Lane AN, Higashi RM, Wang Y, Hamidi AB, Zhou R, Guitart X, Chen G, Manji HK, and Kaddurah-Daouk R (2010). Stable isotope-resolved metabolomic analysis of lithium effects on glial-neuronal metabolism and interactions. Metabolomics 6, 165–179. 10.1007/s11306-010-0208-9. [PubMed: 20631920]

163. Fan TW-M, Lane AN, Higashi RM, and Yan J (2011). Stable isotope resolved metabolomics of lung cancer in a SCID mouse model. Metabolomics 7, 257–269. 10.1007/s11306-010-0249-0. [PubMed: 21666826]

164. Fan TW-M, and Lane AN (2008). Structure-based profiling of metabolites and isotopomers by NMR. Prog. Nucl. Magn. Reson. Spectrosc. 52, 69–117. 10.1016/j.pnmrs.2007.03.002.

165. Fan TW-M, Warmoes MO, Sun Q, Song H, Turchan-Cholewo J, Martin JT, Mahan A, Higashi RM, and Lane AN (2016). Distinctly perturbed metabolic networks underlie differential tumor tissue damages induced by immune modulator b-glucan in a two-case ex vivo non-small-cell lung cancer study. Cold Spring Harb. Mol. Case Stud. 2, a000893. 10.1101/mcs.a000893. [PubMed: 27551682]

166. Lorkiewicz P, Higashi RM, Lane AN, and Fan TW-M (2012). High information throughput analysis of nucleotides and their isotopically enriched isotopologues by direct-infusion FTICR-MS. Metabolomics 8, 930–939. 10.1007/s11306-011-0388-y. [PubMed: 23101002]

167. Moseley HN (2010). Correcting for the effects of natural abundance in stable isotope resolved metabolomics experiments involving ultra-high resolution mass spectrometry. BMC Bioinf. 11, 139. 10.186/1471-2105-11-139.

168. Alipour M, Halwani M, Omri A, and Suntres ZE (2008). Antimicrobial effectiveness of liposomal polymyxin B against resistant Gram-negative bacterial strains. Int. J. Pharm. X. 355, 293–298. 10.1016/j.ijpharm.2007.11.035.

169. Sakai H, Gotoh T, Imura T, Sakai K, Otake K, and Abe M (2008). Preparation and properties of liposomes composed of various phospholipids with different hydrophobic chains using a supercritical reverse phase evaporation method. J. Oleo Sci. 57, 613–621. 10.5650/jos.57.613. [PubMed: 18838834]

170. Yang K, Tran K, and Salvati A (2022). Tuning Liposome Stability in Biological Environments and Intracellular Drug Release Kinetics. Biomolecules 13, 59. 10.3390/biom13010059. [PubMed: 36671444]

171. Hashizaki K, Taguchi H, Itoh C, Sakai H, Abe M, Saito Y, and Ogawa N (2003). Effects of poly(ethylene glycol) (PEG) chain length of PEG-lipid on the permeability of liposomal bilayer membranes. Chem. Pharm. Bull. 51, 815–820. 10.1248/cpb.51.815.

172. Gibbons A, McElvaney NG, and Cryan S-A (2010). A dry powder formulation of liposome-encapsulated recombinant secretory leukocyte protease inhibitor (rSLPI) for inhalation: preparation and characterisation. AAPS PharmSciTech 11, 1411–1421. 10.1208/s12249-010-9500-2. [PubMed: 20839079]

173. Maiseyeu A, Mihai G, Kampfrath T, Simonetti OP, Sen CK, Roy S, Rajagopalan S, and Parthasarathy S (2009). Gadolinium-containing phosphatidylserine liposomes for molecular imaging of atherosclerosis. J. Lipid Res. 50, 2157–2163. 10.1194/jlr.M800405-JLR200. [PubMed: 19017616]

174. Bagalkot V, Badgeley MA, Kampfrath T, Deiuliis JA, Rajagopalan S, and Maiseyeu A (2015). Hybrid nanoparticles improve targeting to inflammatory macrophages through phagocytic signals. J. Contr. Release 217, 243–255. 10.1016/j.jconrel.2015.09.027.

175. Nakazawa G, Otsuka F, Nakano M, Vorpahl M, Yazdani SK, Ladich E, Kolodgie FD, Finn AV, and Virmani R (2011). The pathology of neoatherosclerosis in human coronary implants bare-metal and drug-eluting stents. J. Am. Coll. Cardiol. 57, 1314–1322. 10.1016/j.jacc.2011.01.011. [PubMed: 21376502]

176. Mokry M, Boltjes A, Slenders L, Bel-Bordes G, Cui K, Brouwer E, Mekke JM, Depuydt MAC, Timmerman N, Waissi F, et al. (2022). Transcriptomic-based clustering of human atherosclerotic plaques identifies subgroups with different underlying biology and clinical presentation. Nat. Cardiovasc. Res. 1, 1140–1155. 10.1038/s44161-022-00171-0. [PubMed: 37920851]

177. Di L, Thomas A, Switala L, Kalikasingh K, Lapping S, Nayak L, and Maiseyeu A (2023). Surface Geometry of Cargo-less Gold Nanoparticles Is a Driving Force for Selective Targeting of Activated Neutrophils to Reduce Thrombosis in Antiphospholipid Syndrome. Nano Lett. 23, 9690–9696. 10.1021/acs.nanolett.3c02075. [PubMed: 37884274]

178. Pezzi HM, Niles DJ, Schehr JL, Beebe DJ, and Lang JM (2018). Integration of Magnetic Bead-Based Cell Selection into Complex Isolations. ACS Omega 3, 3908–3917. 10.1021/acsomega.7b01427. [PubMed: 29732449]

179. Pallikkuth S, Kvistad D, Sirupangi T, Kizhner A, Pahwa R, Cameron MJ, Richardson B, Williams S, Ayupe A, Brooks M, et al. (2023). IL-21-IgFc immunotherapy alters transcriptional landscape of lymph node cells leading to enhanced flu vaccine response in aging and SIV infection. Aging Cell 22, e13984. 10.1111/acel.13984. [PubMed: 37712598]

180. Hao Y, Hao S, Andersen-Nissen E, Mauck WM 3rd, Zheng S, Butler A, Lee MJ, Wilk AJ, Darby C, Zager M, et al. (2021). Integrated analysis of multimodal single-cell data. Cell 184, 3573–3587.e29. 10.1016/j.cell.2021.04.048. [PubMed: 34062119]

181. Hafemeister C, and Satija R (2019). Normalization and variance stabilization of single-cell RNA-seq data using regularized negative binomial regression. Genome Biol. 20, 296. 10.1186/s13059-019-1874-1. [PubMed: 31870423]

182. Langmead B, Trapnell C, Pop M, and Salzberg SL (2009). Ultrafast and memory-efficient alignment of short DNA sequences to the human genome. Genome Biol. 10, R25. 10.1186/gb-2009-10-3-r25. [PubMed: 19261174]

183. Shankman LS, Gomez D, Cherepanova OA, Salmon M, Alencar GF, Haskins RM, Swiatlowska P, Newman AAC, Greene ES, Straub AC, et al. (2015). KLF4-dependent phenotypic modulation of smooth muscle cells has a key role in atherosclerotic plaque pathogenesis. Nat. Med. 21, 628–637. 10.1038/nm.3866. [PubMed: 25985364]

184. Li H, Handsaker B, Wysoker A, Fennell T, Ruan J, Homer N, Marth G, Abecasis G, and Durbin R; 1000 Genome Project Data Processing Subgroup (2009). The Sequence Alignment/Map format and SAMtools. Bioinformatics 25, 2078–2079. 10.1093/bioin-formatics/btp352. [PubMed: 19505943]

185. Quinlan AR, and Hall IM (2010). BEDTools: a flexible suite of utilities for comparing genomic features. Bioinformatics 26, 841–842. 10.1093/bioinformatics/btq033. [PubMed: 20110278]

Highlights

- Itaconate (ITA) mediates diet-driven plaque resolution in ASCVD
- ITA-bearing lipid nanoparticles (ITA-LNPs) target plaque and bone marrow myeloid cells
- ITA-LNP treatment recapitulates LCLFD-induced atherosclerotic plaque resolution
- ITA-LNP treatment downregulates inflammatory genes via H3K27ac deacetylation

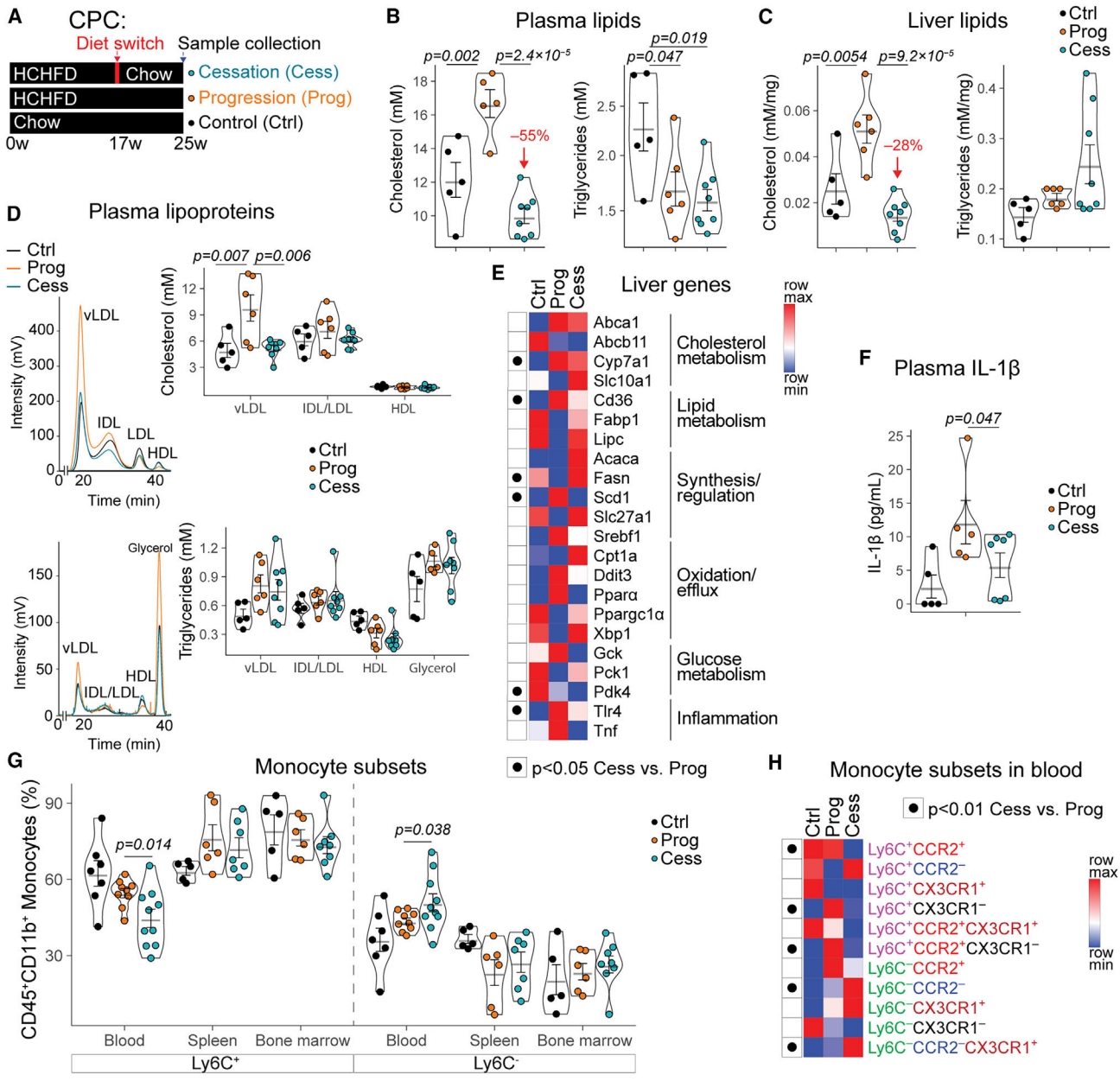

Figure 1. Systemic metrics of atherosclerosis resolution in dietary cessation CPC model

(A) Illustration of the CPC experimental system.

(B) Plasma cholesterol and triglyceride levels after CPC. Data are presented as mean ± SD.

(C) Liver cholesterol and triglyceride levels after CPC normalized on dry tissue weight. Data are presented as mean ± SD.

(D) Plasma lipoprotein subclass analysis after CPC. Lipoproteins (vLDL, LDL, IDL, HDL) were separated using fast protein liquid chromatography with in-line analysis of cholesterol (top) and triglyceride (bottom) content in the effluent. Data are presented as mean ± SD.

(E) Whole-liver mRNA transcript counting using NanoString. The data are shown as a heatmap with a color scale anchored to the minimum and maximum expression values for each gene.

(F) ELISA analysis of IL-1β in plasma after CPC. Data are presented as mean ± SD.
(G) Flow-cytometric analysis of $Ly6C^+$ and LyC^- monocytes subsets in blood, spleen and bone marrow after CPC. Data are presented as mean ± SD.
(H) Flow-cytometric analysis of subpopulations of $Ly6C^+$ and $Ly6C^-$ monocytes in blood. The data are presented in the same manner as in (E).
Data were analyzed and *p* values were obtained by one-way ANOVA with Tukey's multiple comparisons test or pairwise t test with Holm post hoc correction. n =5 (Ctrl), 6 (Prog), and 8 (Cess) animals in (A)–(F) and n = 5–7 (Ctrl), 6–9 (Prog), and 7–10 (Cess) animals in (G) and (H).

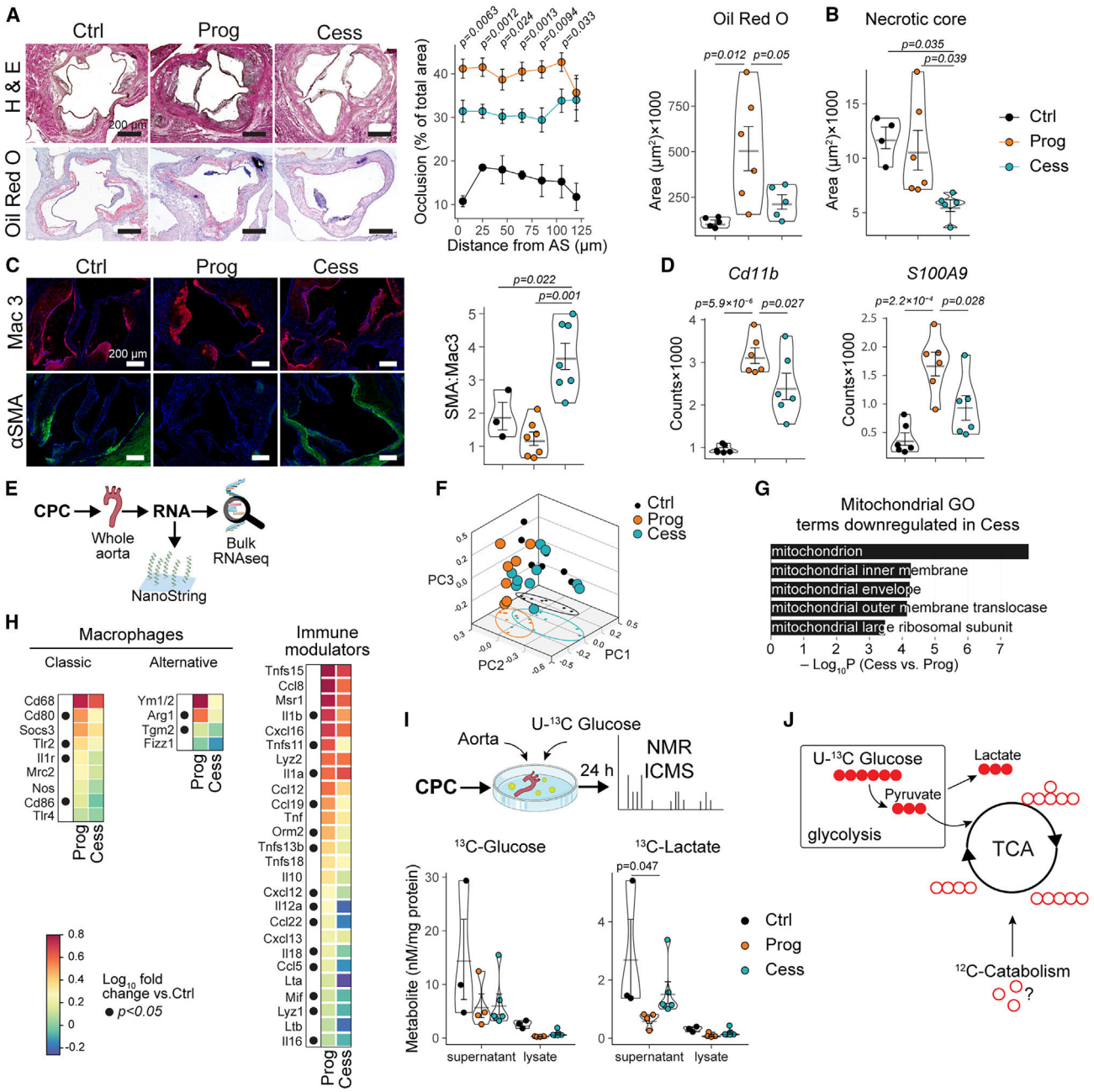

Figure 2. Cessation reduces atherosclerosis and plaque inflammation through glycolytic metabolism activation

(A) Representative photomicrographs of H&E- and oil-red-O-stained sections of aortic root from CPC. Left: quantification of atherosclerosis burden using analysis of luminal occlusion in consecutive tissue sections starting from aortic sinus (AS). Right: quantification of oil red O staining in the adjacent tissue sections. Data are presented as mean ± SD. Scale bar, 200 μm.

(B) Necrotic core analysis using H&E-stained sections from (A). Data are presented as mean ± SD.

(C) Representative immunofluorescence images of Mac-3- and αSMA-stained aortic root tissue sections and corresponding quantitative ratio analysis (right). Counterstain is DAPI (blue). Data are presented as mean ± SD. Scale bar, 200 μm.
(D) NanoString analysis of whole aortas for *Cd11b* and *S100A9*. Data are presented as mean ± SD.
(E) Schematic of transcriptomic analysis of aortas.
(F) Principal component (PC) analysis in bulk RNA-seq from whole aortas of CPC mice.
(G) Gene ontology (GO) analysis comparing Cess and Prog RNA-seq datasets. Most represented downregulated GO terms in cellular component sub-ontology are shown.
(H) Heatmap displaying fold change ($\log_{10}$) of mRNA expression of specific genes as indicated, measured using RNA-seq and normalized vs. Ctrl samples in whole aortas from CPC. Filled circles indicate $p < 0.05$.
(I) Schematic showing SIRM experiments in cultured aorta organoids and the analysis of uniformly labeled [^{13}C]glucose (U-^{13}C) and lactate using HSQC-NMR spectroscopy. Data are presented as mean ± SD.
(J) Diagram hypothesizing a metabolic shift and fuel utilization in Cess vs. Prog in CPC. Filled circles represent ^{13}C-labeled metabolites derived from [^{13}C]glucose, and open circles depict ^{12}C metabolites originating from other sources. The diagram summarizes the findings from SIRM (see also Figure S2G).
Data were analyzed and *p* values were obtained using pairwise t-test with Holm post hoc correction. $n = 3–5$ (Ctrl), 4–7 (Prog), and 5–8 (Cess) animals.

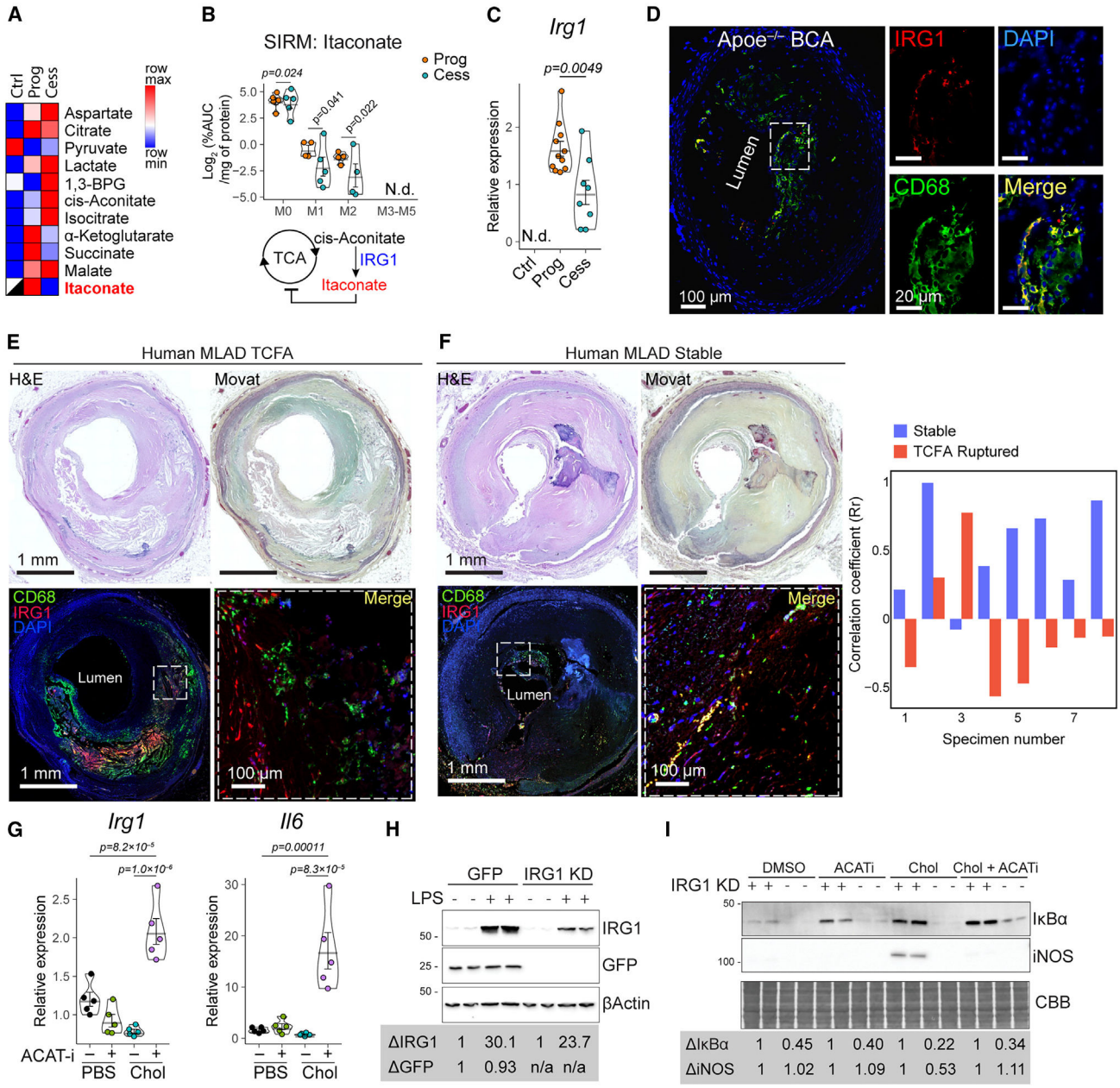

Figure 3. IRG1 and itaconate expression in mouse and human lesions

(A) Relative levels of the metabolites of the TCA cycle in whole aortas from CPC. White/black square on bottom left denotes not detected.

(B) SIRM analysis of itaconate isotopologs in CPC aortas from (A). Bottom: scheme illustrating the production of itaconate. Data are presented as mean ± SD. *p* values were obtained from Student's t-test.

(C) qPCR analysis of the levels of *Irg1* transcripts in whole aortas from separate CPC cohorts. N.d., not detected. Data are presented as mean ± SD. *p* values were obtained from Student's t-test.

(D) Immunofluorescence micrographs depicting positive staining for IRG1 and CD68 in BCA lesions from Prog mice with DAPI counterstain. Scale bars, 100 and 20 μm.

(E and F) Histologic assessment with H&E and Movat pentachrome stains and immunofluorescence analysis of IRG1 and CD68 expression in human (F) stable vs. (E) vulnerable thin-cap fibroatheroma (TCFA) plaques from mid-left anterior descending artery (MLAD) with DAPI counterstain. Quantification of co-localization between IRG1 and CD68 is included in (F). Scale bars, 1 mm and 100 μm.

(G) BMDMs were treated with free cholesterol for 48 h in the presence or absence of acyl-coenzyme A cholesterol acyltransferase inhibitor (ACAT-i) followed by qPCR mRNA analysis of the expression of *Irg1* and *Il6* as indicated. Data are presented as mean ± SD. *p* values were obtained from ANOVA with Tukey post hoc.

(H) Immunoblot of IRG1 knockdown in iBMDMs using shRNA.

(I) iBMDMs with the IRG1 knockdown (IRG1 KD) or control cells were treated with cholesterol as in (G), and the levels of IkBα and iNOS were determined in the cell lysates using immunoblotting. Staining with Coomassie brilliant blue (CBB) was used as total protein loading control.

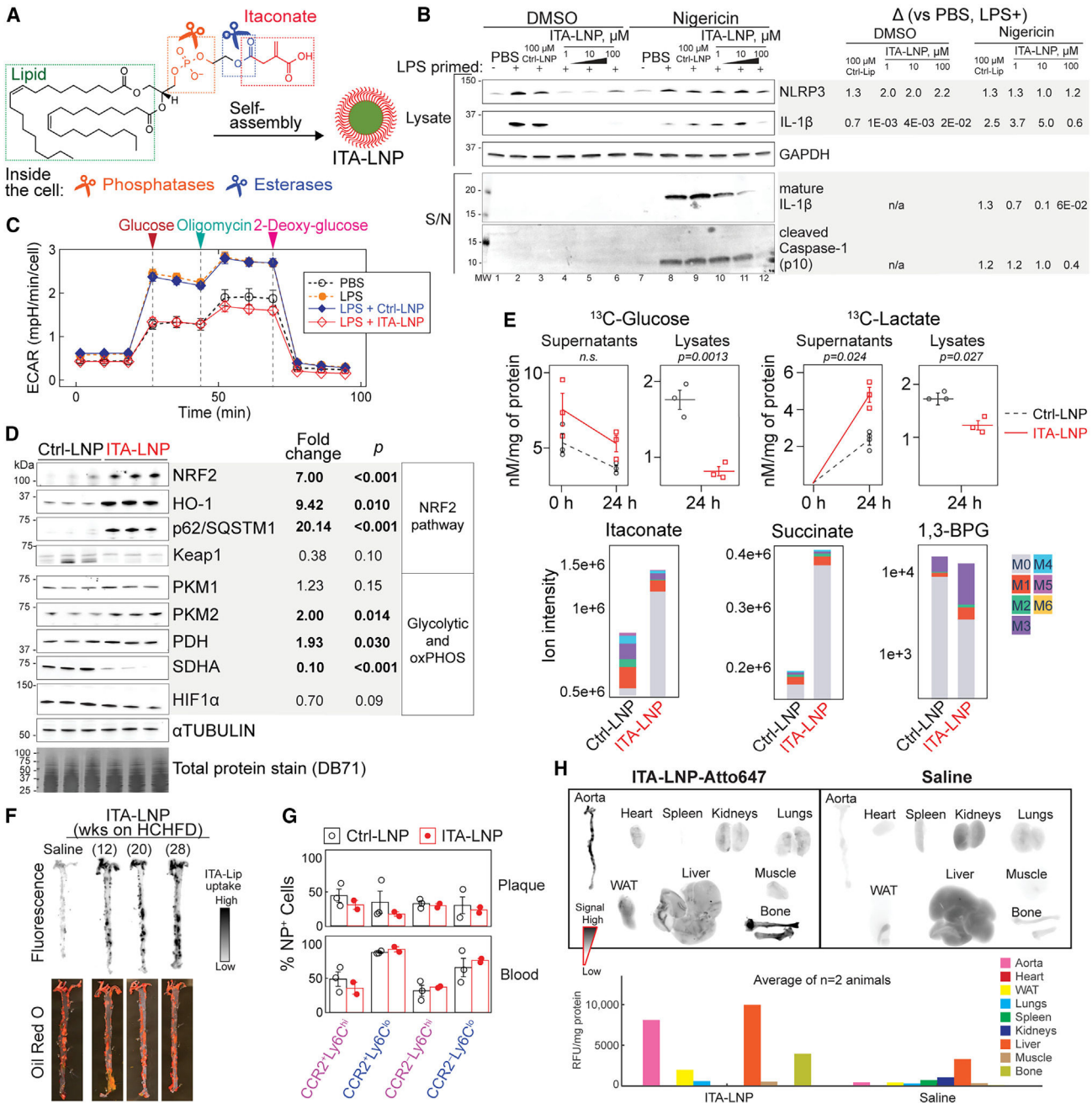

Figure 4. ITA-LNP is an engineered nanometabolite that raises intracellular itaconate levels, exhibits robust anti-inflammatory and metabolic effects *in vitro* and *in vivo*, and accumulates in plaque and bone marrow

(A) Chemical structure of itaconate pro-drug and schematic of self-assembled ITA-LNP.

(B) Immunoblot for inflammasome assays in Ctrl/ITA-LNP-treated BMDMs.

(C) Seahorse analysis of BMDMs pre-treated with Ctrl/ITA-LNP with LPS stimulation. Data are presented as mean ± SD.

(D) Immunoblotting for various metabolic targets of itaconate in Ctrl/ITA-LNP-treated BMDM lysate. *p* values were obtained from Student's t-test.

(E) SIRM experiments in BMDMs cultured with U-^{13}C-labeled glucose and treated with Ctrl/ITA-LNP for 24 h. [U-^{13}C]glucose and [U-^{13}C]lactate levels in supernatants and lysates were measured with HSQC-NMR spectroscopy and normalized to the total lysate protein content. Bottom: IC-MS analysis of itaconate, succinate, and 1,3-bisphosphoglyceric acid (1,3-BPG) isotopologs in the same experiments. Data are presented as mean ± SD. *p* values were obtained from Student's t-test.

(F) Fluorescence imaging of whole aortas excised 24 h post bolus injection of Atto647-labeled ITA-LNP in *Ldlr*$^{-/-}$ mice fed with HCHFD and corresponding oil red O staining of the same aortas.

(G) Flow-cytometric analysis of Ctrl/ITA-LNP-targeted cells in blood and plaque post bolus injection in *Ldlr*$^{-/-}$ animals fed with HCHFD for 12 weeks. Data are presented as mean ± SD.

(H) Atto647-labeled ITA-LNP were bolus injected intravenously in high-fat-fed *Ldlr*$^{-/-}$ mice (20 weeks on HCHFD), and the organs were excised following extensive perfusion at 6 h post injection. Mice injected with saline served as a control. Bottom: quantification of Atto647 content normalized to total protein content of the respective organs. $n = 2$ animals per group; statistical analysis was not performed.

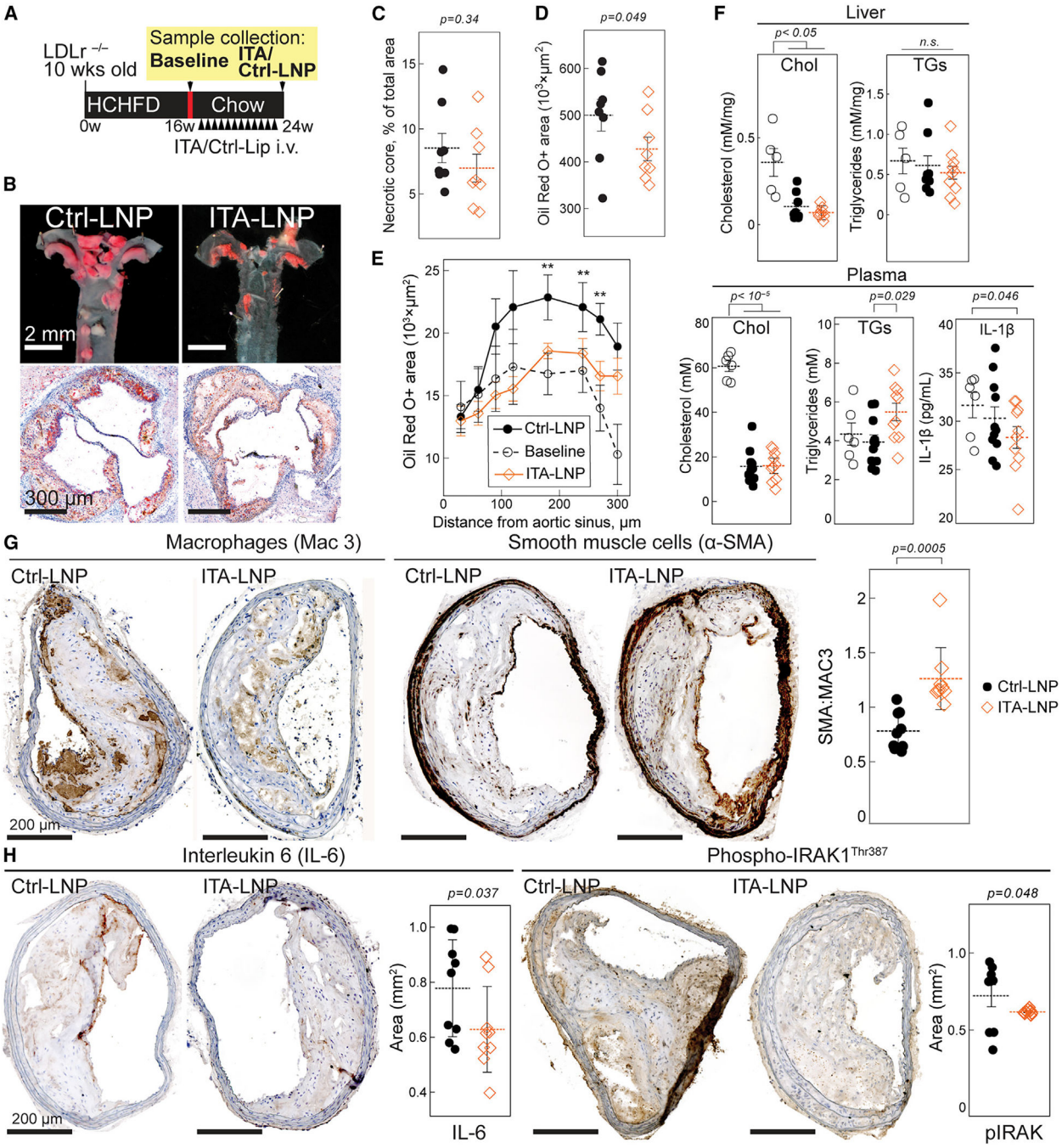

Figure 5. ITA-LNP accumulates in plaque and alleviates inflammation

(A) Timeline of efficacy testing experiments in *Ldlr*$^{-/-}$ mice.

(B) En face and histologic analysis of aortic root after oil red O staining from Ctrl/ITA-LNP-treated mice from A. Scale bars, 2 mm and 300 μm.

(C and D) Quantification of (C) necrotic core and (D) plaque burden in oil-red-O-stained brachiocephalic artery (BCA) samples from (A). Data are presented as mean ± SD. *p* values were obtained from Student's t-test.

(E) Quantification of aortic root plaque burden in oil-red-O-stained consecutive tissue sections from (A). Data are presented as mean ± SD. *p* values were obtained from ANOVA with Tukey's post hoc test.
(F) Plasma lipids, IL-1β levels, and liver lipids as indicated from (A). Data are presented as mean ± SD. *p* values were obtained from ANOVA with Tukey's post hoc test.
(G) Metrics of plaque stability: macrophages and smooth muscle actin staining in BCA samples from Ctrl/ITA-LNP-treated mice with corresponding quantitative ratio analysis (right). Data are presented as mean ± SD. Scale bar, 200 mm. *p* values were obtained from Student's t-test.
(H) Metrics of IL-1β signaling: IL-6 and phospho-IRAK in BCA samples from the same mice. Right: quantification with target levels normalized to the total area. $n = 6–15$ animals per group. Data are presented as mean ± SD. *p* values were obtained from Student's t-test. Scale bar, 200 μm.

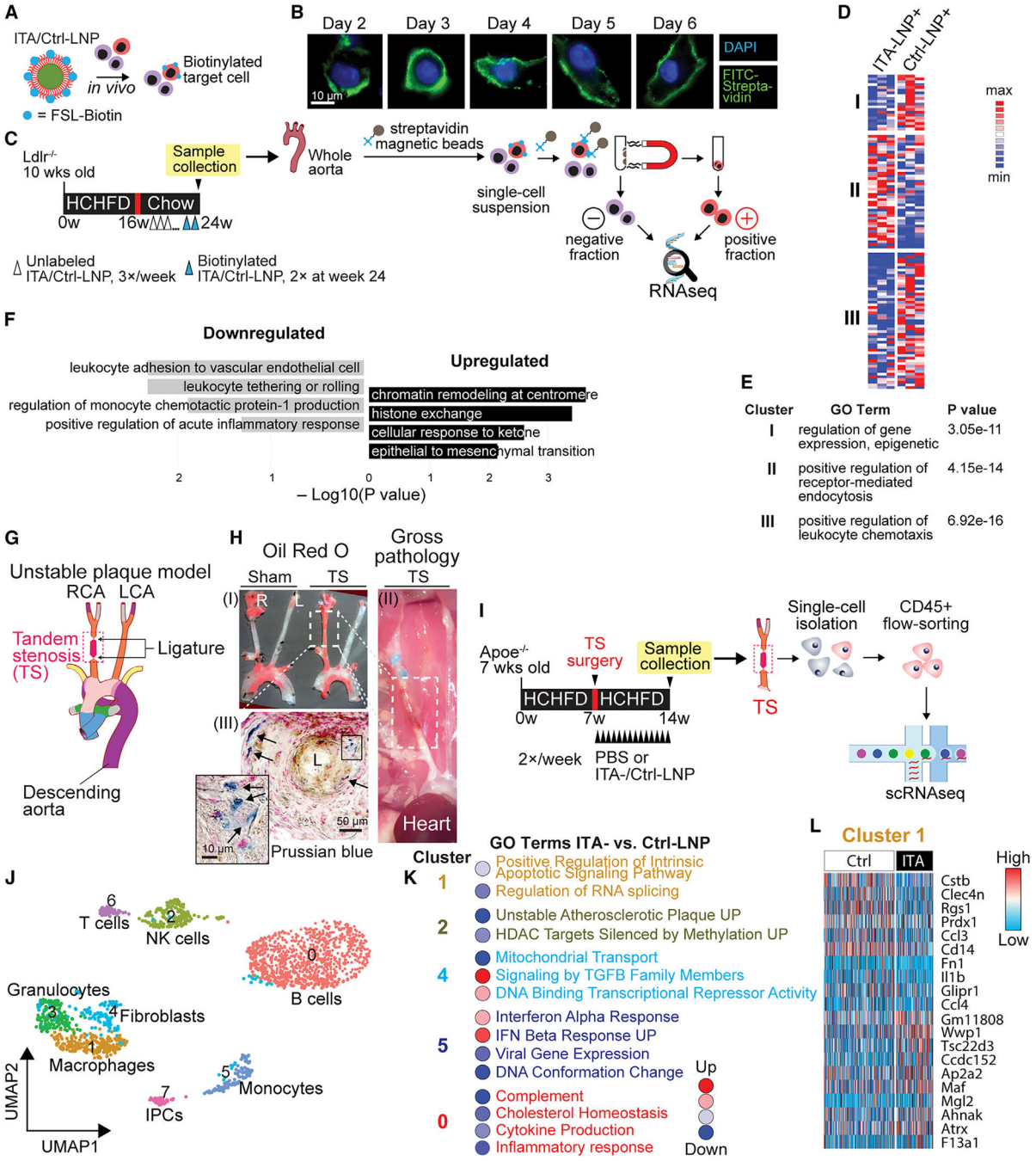

Figure 6. ITA-LNP targets inflammatory, epigenetic, and plaque vulnerability pathways in atherosclerotic lesions

(A) Schematic of *in vivo* cell biotinylation using ITA-LNP incorporating FSL-biotin.

(B) *In vitro* proof-of-concept studies demonstrating biotin label stability in BMDMs treated with ITA-LNP-FSL-biotin on day 1. Surface biotin presence was visualized with FITC-streptavidin.

(C) Schematic of experimental workflow for *in vivo* labeling and magnetic isolation of ITA-LNP-targeted cells in plaque and blood of *Ldlr*$^{-/-}$ Cess animals simultaneous with ITA-LNP therapy.

(D and E) mRNA from Ctrl/ITA-LNP-targeted cells in plaque from (C) was subjected to bulk RNA-seq and data analysis of representative hierarchical clusters of gene ontology (GO biological process). *p* values were derived from Benjamini-Hochberg multiple testing with False Discovery Rate (FDR) < 0.05.

(F) GO analysis of Ctrl/ITA-LNP-targeted cells in blood.

(G) Schematic of tandem stenosis to form unstable plaque (TS). A ligature was placed in the right carotid artery (RCA).

(H) Characterization of the TS model. I, oil red O lipid staining; II, gross pathology; III, Prussian blue iron staining in RCA sections. Scale bars, 10 μm and 50 μm.

(I) Experimental workflow scheme for ITA-LNP testing in TS model.

(J) $CD45^+$ cells from RCA segments were subjected to scRNA-seq. Uniform manifold approximation and projection (UMAP) clustering analysis identified distinct cell types.

(K) GO analysis of the most prevalent clusters from (J).

(L) Heatmap indicating differentially expressed genes in cluster 1 (macrophages).

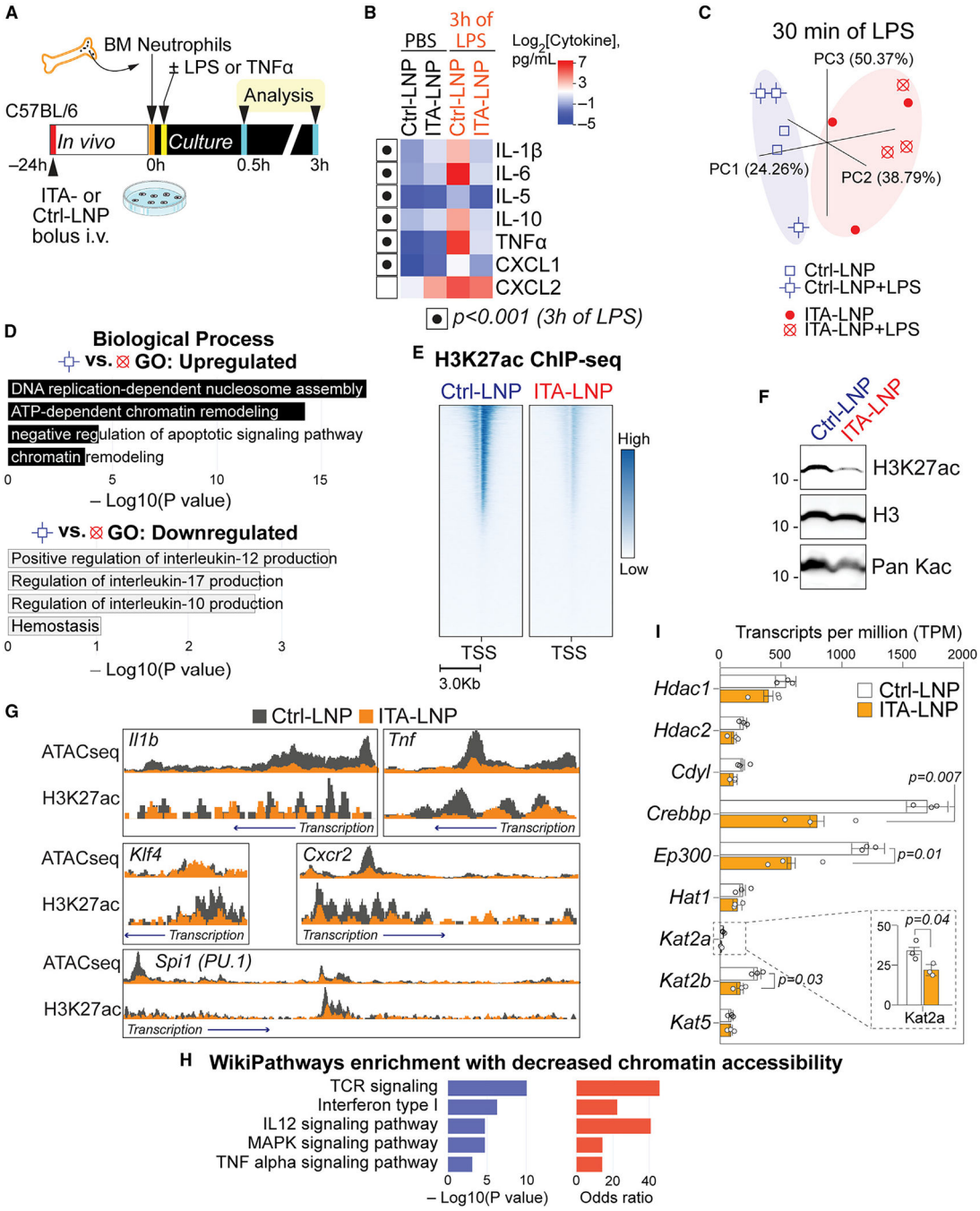

Figure 7. ITA-LNP "reprograms" bone marrow to immunomodulatory phenotype through impaired histone acetylation

(A) Ctrl/ITA-LNP were injected into wild-type mice followed by neutrophil isolation from bone marrow. Neutrophils were cultured and stimulated by LPS or TNF-α *in vitro*.

(B) Cytokines in supernatants from (A) as determined by Luminex ($n = 7$). Filled circles indicate $p < 0.001$.

(C) Principal component (PC) analysis after bulk RNA-seq of mRNA obtained from (A).

(D) GO analysis of Ctrl/ITA-LNP treated neutrophils with and without LPS stimulation.

(E) ChIP-seq heatmaps showing acetylation of H3K27 near the transcription start site (TSS). The data were obtained from whole bone marrow cells in separate experiments conducted as shown in (A) but without stimulation *in vitro*.

(F) Immunoblot probing for H3K27ac and pan-acetylated lysine (Kac) in lysates of cultured BMDMs treated with Ctrl/ITA-LNP.

(G) Profiles of H3K27ac ChIP-seq occupancy and ATAC-seq in loci of the indicated genes from flow-sorted ITA-LNP-targeted bone marrow cells. See text and Figure S7A for identity of these cells.

(H) WikiPathways GO analysis of gene set enrichments for downregulated genes in ITA-LNP vs. Ctrl-LNP groups from ATAC-seq datasets.

(I) RNA-seq counts of histone acetylation regulating genes differentially expressed in whole bone marrow cells in separate experiments conducted as shown in (A) but without stimulation. Data are presented as mean ± SD. The *p* values were obtained from ANOVA with Tukey post hoc test.

KEY RESOURCES TABLE

REAGENT or RESOURCE	SOURCE	IDENTIFIER
Antibodies		
CD45 Monoclonal Antibody (30-F11), eVolve 605, eBioscience™	ThermoFisher Scientific	Cat#: 83-0451-42; RRID: AB_2574712
Ly-6C Monoclonal Antibody (HK1.4), eFluor 450, eBioscience™	ThermoFisher Scientific	Cat#: 48-5932-82; RRID: AB_10805519
BUV737 Rat Anti-Mouse CD24	BD Biosciences	Cat#: 565308; RRID: AB_2739174
Brilliant Violet 711™ anti-mouse CD64 (FcγRI) Antibody	BioLegend	Cat#: 139311; RRID: AB_2563846
FITC anti-mouse Ly-6G Antibody	BioLegend	Cat#: 127605; RRID: AB_1236488
PE/Dazzle™ 594 anti-mouse I-A/I-E Antibody	BioLegend	Cat#: 107647; RRID: AB_2565978
PE/Cy7 anti-mouse F4/80 Antibody	BioLegend	Cat#: 123113; RRID: AB_893490
APC Hamster Anti-Mouse CD11c	BD Biosciences	Cat#: 561119; RRID: AB_398460
APC-Cy™7 Rat Anti-CD11b	BD Biosciences	Cat#: 561039; RRID: AB_396772
Alexa Fluor® 700 anti-mouse/human CD11b Antibody	BioLegend	Cat#: 101222; RRID: AB_493705
Biotin anti-mouse CD115 (CSF-1R) Antibody	BioLegend	Cat#: 135507; RRID: AB_2028401
Brilliant Violet 510™ anti-mouse CD192 (CCR2) Antibody	BioLegend	Cat#: 150617; RRID: AB_2721535
APC/Fire™ 750 anti-mouse CX3CR1 Antibody	BioLegend	Cat#: 149039; RRID: AB_2632859
FITC anti-mouse CD3ε Antibody	BioLegend	Cat#: 100305; RRID: AB_312670
FITC anti-mouse CD19 Antibody	BioLegend	Cat#: 115505; RRID: AB_313640
Purified rat Mac-3 (1:50)	BD Pharmingen	Cat#: 550292; RRID: AB_393587
Biotinylated Rabbit Anti-Rat IgG (1:1000)	Vector	Cat#: BA-4001; RRID: AB_10015300
Anti-Actin, alpha smooth muscle, mouse monoclonal (1:50)	Sigma-Aldrich	Cat#: A5228, RRID: AB_262054
Anti-Mouse IgG (H + L) X-Adsorbed-Biotin (1:5000)	Sigma-Aldrich	Cat#: RI20683; RRID: AB_2910246
TruStain FcX™ (anti-mouse CD16/32)	BioLegend	Cat#: 101320; RRID: AB_1574975
anti-human IRG1 (D6H2Y) Rabbit mAb	Cell Signaling Technology	Cat#: 77510; RRID:AB_2799901
anti-mouse IRG1 (E5B2G) Rabbit mAb	Cell Signaling Technology	Cat#: 19857; RRID:AB_3076520
anti-mouse NRF2 (D1Z9C) XP Rabbit mAb	Cell Signaling Technology	Cat#: 12721; RRID:AB_2715528
anti-mouse HO-1 (E3F4S) Rabbit mAb	Cell Signaling Technology	Cat#: 43966; RRID:AB_2799254
anti-mouse SQSTM1/p62 (D1Q5S) Rabbit mAb	Cell Signaling Technology	Cat#: 39749; RRID:AB_2799160
anti-mouse PKM1 (D30G6) XP Rabbit mAb	Cell Signaling Technology	Cat#: 7067; RRID:AB_2715534
anti-mouse PKM2 (D78A4) XP Rabbit mAb	Cell Signaling Technology	Cat#: 4053; RRID:AB_1904096
anti-mouse Pyruvate Dehydrogenase (C54G1) Rabbit mAb	Cell Signaling Technology	Cat#: 3205; RRID:AB_2162926
anti-mouse SDHA (D6J9M) XP Rabbit mAb #11998	Cell Signaling Technology	Cat#: 11998; RRID:AB_2750900
alpha Tubulin Antibody (DM1A)	Novus Biologicals	Cat#: NB100-690; RRID:AB_521686
anti-mouse NLRP3/NALP3 mAb (Cryo-1)	AdipoGen	Cat#: AG-20B-0006-C100; RRID:AB_2819182
anti-mouse Interleukin-1β antibody polyclonal antibody produced in goat	Millipore Sigma	Cat#: I3767; RRID:AB_477105
anti-mouse GAPDH (D16H11) XP Rabbit mAb (HRP Conjugate)	Cell Signaling Technology	Cat#: 8884; RRID:AB_11129865
anti-mouse Caspase-1 (p10) mAb (Casper-2)	AdipoGen	Cat#: AG-20B-0044-C100; RRID:AB_2490253
anti-mouse phospho-IRAK1 (Thr387) Polyclonal Antibody	Bioss Antibodies	Cat#: bs-3194R; RRID:AB_10857144
anti-mouse IL-6 (D5W4V) XP Rabbit mAb	Cell Signaling Technology	Cat#: 12912; RRID:AB_2798059

REAGENT or RESOURCE	SOURCE	IDENTIFIER
anti-mouse Anti-Actin, α-Smooth Muscle antibody (1A4) Mouse mAb	Millipore Sigma	Cat#: A5228; RRID:AB_262054
anti-mouse AATM Antibody (E–7) mouse mAb	Santa Cruz Biotechnology	Cat#: sc-271702; RRID:AB_10710382
anti-human IRG1 Rabbit polyclonal antibody	Abcam	Cat#: ab238580
anti-mouse Cytokeratin 18 (DC10) mAb	ThermoFisher Scientific	Cat#: MA5-12104; RRID:AB_10981680
anti-mouse Cleaved PARP (Asp214) (D6X6X) Rabbit mAb	Cell Signaling Technology	Cat#: 94885; RRID:AB_2800237
anti-mouse Phospho-MLKL (Ser345) (D6E3G) Rabbit mAb	Cell Signaling Technology	Cat#: 37333; RRID:AB_2799112
anti-Ubiquitin (E6K4Y) XP Rabbit mAb	Cell Signaling Technology	Cat#: 20326; RRID:AB_3064918
anti-mouse CD68 (E3O7V) Rabbit mAb	Cell Signaling Technology	Cat#: 97778; RRID:AB_2928056
anti-human CD68 (KP1) mouse mAb	ThermoFisher Scientific	Cat#: 14-0688-82; RRID:AB_11151139
anti-mouse CHI3L1/YKL40 Polyclonal antibody	ProteinTech	Cat#: 12036-1-AP; RRID:AB_2877819
Goat anti-Mouse IgG (H + L) Highly Cross-Adsorbed Secondary Antibody, Alexa Fluor™ Plus 488	ThermoFisher Scientific	Cat#: A32723TR; RRID:AB_2866489
Donkey anti-Rabbit IgG (H + L) Highly Cross-Adsorbed Secondary Antibody, Alexa Fluor™ Plus 647	ThermoFisher Scientific	Cat#: A32795TR; RRID:AB_2866496
Goat anti-Rabbit IgG (Heavy chain), Superclonal™ Recombinant Secondary Antibody, HRP	ThermoFisher Scientific	Cat#: A27036; RRID:AB_2536099
Rabbit anti-Goat IgG (Heavy Chain), Superclonal™ Recombinant Secondary Antibody, HRP	ThermoFisher Scientific	Cat#: A27014; RRID:AB_2536079
Rabbit anti-Mouse IgG (H + L), Superclonal™ Recombinant Secondary Antibody, HRP	ThermoFisher Scientific	Cat#: A27025; RRID:AB_2536089
Anti-acetyl-Histone H3 (Lys27) Antibody	Millipore Sigma	Cat#: 07-360; RRID:AB_310550
Biological samples		
Human aortic tissue	CVPath Institute	https://www.cvpath.org/
Human tonsil tissue	CVPath Institute	https://www.cvpath.org/
Chemicals, peptides, and recombinant proteins		
PE Streptavidin (High Concentration)	BioLegend	Cat#: 405245
Tris-EDTA (pH 9)	Abcam	ab93684; CAS: 77-86-1, 6381-92-6
Tris-HCl (pH 8)	Thermo Fisher Scientific	15568025; CAS: 77-86-1, 7647-01-0
Tris-buffered saline	Thermo Fisher Scientific	J60764.K2; CAS: 77-86-1, 7647-14-5
Chloroform	Sigma-Aldrich	288306; CAS: 67-66-3
Methanol	Thermo Fisher Scientific	610090040; CAS: 67-56-1
Sodium taurocholate	Sigma-Aldrich	86339; CAS: 345909-26-4
Sodium dodecyl sulfate	Merck	8220500100; CAS: 151-21-3
Dithiothreitol	Roche	10197777001; CAS: 3483-12-3
Acetonitrile	Acros Organics	610961000; CAS: 75-05-8
Deuterium oxide	Cambridge Isotope Laboratories	DLM-4-PK; CAS: 7789-20-0; (labeled) 7732-18-5 (unlabeled)
Ethylenediaminetetraacetic acid	Thermo Fisher Scientific	S312; CAS: 6381-92-6
d6-2,2-dimethyl-2-silapentane-5-sulfonate	Cambridge Isotope Laboratories	DLM-8206-PK; CAS: 284664-85-3 (labeled); 2039-96-5 (unlabeled)
D-glucose (U-$^{13}C_6$, 99%)	Cambridge Isotope Laboratories	CLM-1396-5; CAS: 110187-42-3 (labeled); 50-99-7 (unlabeled)

REAGENT or RESOURCE	SOURCE	IDENTIFIER
TRIzol™ Reagent	Thermo Fisher Scientific	15596026
Fetal bovine serum	Gemini Biosciences	100-108
ACK lysing buffer	Thermo Fisher Scientific	A1049201
18:1 Ptd Ethylene Glycol	Avanti Polar Lipids	870302; CAS: 474923-51-8
Boron trifluoride tetrahydrofuran complex	Sigma-Aldrich	434280; CAS: 462-34-0
1,2-dipalmitoyl-*sn*-glycero-3phosphoethanolamine (DPPE)-Atto647	Atto-Tec GmbH	AD 647-155
Sodium itaconate	Sigma-Aldrich	93598; CAS: 97-65-4
Itaconic anhydride	Acros Organics	412940250; CAS: 2170-03-8
100 nm Nuclepore membranes	Avanti Polar Lipids	610005-1EA
20 kDa MWCO cellulose membrane	Repligen	131345
Sodium hydroxide	Sigma-Aldrich	221465; CAS: 1310-73-2
Hydrochloric acid	Thermo Fisher Scientific	L13091.AU; CAS: 7647-01-0
MEM Non-essential Amino Acid Solution	Thermo Fisher Scientific	11140050
Mouse Macrophage colony stimulating factor	R&D Systems	414-CS; CAS: 81627-83-0
4-(2-hydroxyethyl)-1-piperazineethanesulfonic acid (HEPES)	Corning	MT 61-034-RR; CAS 7365-45-9
Calcium chloride	Sigma-Aldrich	21115; CAS: 10043-52-4
Bovine serum albumin	Gemini Bio-Products	700-107P; CAS: 9048-46-8
Ketamine	Hanna's Pharmaceutical Supply	CAS: 6740-88-1
Xylazine	Hanna's Pharmaceutical Supply	CAS: 7361-61-7
Collagenase H	Sigma-Aldrich	COLLH-RO
Histopaque 1119	Sigma-Aldrich	11191
Histopaque 1077	Sigma-Aldrich	10771
Taqman Fast Advanced Master Mix	Thermo Fisher Scientific	4444556
2x Laemmli SDS loading buffer	Bio-Rad	1610737
Polybrene	Santa Cruz Biotechnology	sc-134220; CAS: 28728-55-4
Puromycin dihydrochloride	AdipoGen	AGCN20078M025; CAS: 58-58-2
Cholic acid	Sigma-Aldrich	C1129; CAS: 81-25-4
4-octyl itaconate	Cayman Chemical	25374; CAS: 3133-16-2
QUANTI-Blue™ Solution	InvivoGen	rep-qbs
Dimethyl sulfoxide	Corning	25-950-CQC; CAS: 67-68-5
Tunicamycin	Sigma-Aldrich	T7765; CAS: 11089-65-9
Oxidized LDL	Athens Research and Technology	12-16-120412-OX
Cholesterol-Water Soluble (CD-cholesterol)	Sigma-Aldrich	C4951; CAS: 57-88-5
Lipopolysaccharides from Escherichia coli O111:B4	Sigma-Aldrich	L2630
Ultra pure Lipopolysaccharides Escherichia coli O111:B4	List Biological Labs	#421
CP-113818	MedChemExpress	HY-105445; CAS: 135025-12-6
Nigericin	Sigma-Aldrich	N7143; CAS: 28643-80-3
Buprenorphine	Hanna's Pharmaceutical Supply	CAS: 2485-79-7
DMEM	Agilent Technologies	103575–100

REAGENT or RESOURCE	SOURCE	IDENTIFIER
RPMI	Sigma-Aldrich	R0883
William's Medium E	Thermo Fisher Scientific	A1217601
Opti-MEM	Thermo Fisher Scientific	31985062
Antibiotic-antimycotic	Thermo Fisher Scientific	15240062
Actinomycin D from *Streptomyces* sp.	Sigma-Aldrich	A4262
Dynabeads™ M-280 Streptavidin	Thermo Fisher Scientific	11206D
Dynabeads™ Protein A/Protein G	Thermo Fisher Scientific	10015D
FSL-biotin	Sigma-Aldrich	F9182
1,2-dioleoyl-*sn*-glycero-3-phospho(ethylene glycol)	Avanti Polar Lipids	CAS: 474923-51-8
1,2-dioleoyl-*sn*-glycero-3-phospho-L-serine	Avanti Polar Lipids	CAS: 90693-88-2
1-palmitoyl-2-oleoyl-*glycero*-3-phosphocholine	Avanti Polar Lipids	CAS: 26853-31-6
1,2-dipalmitoyl-*sn*-glycero-3-phosphocholine	Avanti Polar Lipids	CAS: 63-89-8
1,2-distearoyl-*sn*-glycero-3-phosphoethanolamine-N-[methoxy(polyethylene glycol)-2000]	Avanti Polar Lipids	CAS: 474922-77-5
1,2-dioleoyl-*sn*-glycero-3-phospho-(1′-rac-glycerol)	Avanti Polar Lipids	CAS: 67254-28-8
Critical commercial assays		
Mouse Insulin ELISA	ALPCO	80-INSMS-E01
Laboratory Cholesterol Standard (200 mg/dL)	Stanbio Laboratory	1012–030
Total Cholesterol Reagents (Infinity)	Thermo Fisher Scientific	TR13421
Triglycerides Reagent (Infinity)	Thermo Fisher Scientific	TR22421
Triglycerides Standard (2 mg/mL)	Pointe Scientific	T7531-STD
Pointe Scientific Triglycerides Liquid Reagents	Fisher Scientific	T7532500
Free Fatty Acid Quantitation Kit	Millipore-Sigma	MAK044
Phospholipid Assay Kit	Millipore-Sigma	MAK122
Mouse Cytokine Array/Chemokine Array 31-Plex (MD31)	Eve Technologies	MD31
RNeasy Mini Kit	Qiagen	74004
Bicinchoninic acid (BCA) assay	Thermo Fisher Scientific	A55864
Direct-zol RNA Miniprep Kit	Zymo Research	R2054
RNAscope 2.5 HD Assay - BROWN	RNAscope	322370
Mouse IFN-beta DuoSet ELISA	R&D Systems	DY8234-05
ImmPRESS® HRP Horse Anti-Rabbit IgG Polymer Detection Kit, Peroxidase	Vector Laboratories	MP-7401
ImmPACT® DAB EqV Substrate Kit, Peroxidase (HRP)	Vector Laboratories	SK-4103
Seahorse XF Glycolysis Stress Test Kit	Agilent Technologies	103020–100
NADP/NADPH-Glo™ Assay	Promega Corporation	G9081
GSH/GSSG-Glo™ Assay	Promega Corporation	V6612
Deposited data		
SRA data for scRNA-seq tandem stenosis	Sequence Read Archive (SRA)	PRJNA729752
CPC model (Figures 1 and 2)	Sequence Read Archive (SRA)	PRJNA530042

REAGENT or RESOURCE	SOURCE	IDENTIFIER
IC-MS datasets in RAW format	ProteomeXchange	PXD041137
Experimental models: Cell lines		
IL-1β Reporter HEK 293 Cells	InvivoGen	hkb-il1bv2
RAW 264.7	ATCC	TIB-71
THP1	ATCC	TIB-202
iBMDMs	Kerafast	ENH166-FP
Experimental models: Organisms/strains		
Mouse: B6.129P2-Apoe^{m1Unc}/J	The Jackson Laboratory	RRID:IMSR_JAX:002052
Mouse: B6.129S7-Ldlr^{tm1Her}/J	The Jackson Laboratory	RRID:IMSR_JAX:002207
Oligonucleotides		
List of probes used for liver gene expression	See Table S4	–
List of probes used for aorta gene expression	See Table S5	–
Software and algorithms		
NextFlow	Seqera	https://www.nextflow.io/
MestReNova	Mestrelab	https://mestrelab.com/software/mnova-software/
ChenomX	Chenomx Inc	https://www.chenomx.com/
Thermo TraceFinder	Thermo Fisher Scientific	https://www.thermofisher.com/us/en/home/industrial/mass-spectrometry/liquid-chromatography-mass-spectrometry-lc-ms/lc-ms-software/lc-ms-data-acquisition-software/tracefinder-software.html
FlowJo	FLOWJO LLC	https://www.flowjo.com/
Other		
Zeiss LSM800 Confocal Scanning Microscope	Carl Zeiss	LSM800
Superose 6 Increase 3.2/300 FPLC column	Cytiva	29091598
25 mL Biocompatible PEEK Static Mixer	ASI	401-0025B